NASA Technical Paper 1535

Summary of Low-Speed Longitudinal Aerodynamics of Two Powered Close-Coupled Wing-Canard Fighter Configurations

John W. Paulson, Jr., and James L. Thomas

DECEMBER 1979

NASA

NASA Technical Paper 1535

Summary of Low-Speed Longitudinal Aerodynamics of Two Powered Close-Coupled Wing-Canard Fighter Configurations

John W. Paulson, Jr., and James L. Thomas
Langley Research Center
Hampton, Virginia

National Aeronautics
and Space Administration

**Scientific and Technical
Information Branch**

1979

SUMMARY

Investigations of the low-speed longitudinal characteristics of two powered close-coupled wing-canard fighter configurations have been completed in the Langley V/STOL tunnel. Data were obtained at angles of attack from -2° to 42°, Mach numbers from 0.12 to 0.20, nozzle and flap deflections from 0° to 40°, and thrust coefficients from 0 to 2.0 to represent both high-angle-of-attack subsonic maneuvering characteristics and conventional takeoff and landing characteristics. Limited data were obtained at angles of attack of 0° and 10° with the nozzles deflected either 60° or 90° and the flaps deflected 60° to represent vertical or short takeoff and landing characteristics.

These data have been published under several formal and informal covers; summary data which show the general findings of this experimental test program are presented in this report. For this type of configuration, these data generally showed the increases in lift coefficient and maximum lift coefficient, improvements in lift-drag polars, and decreases in longitudinal stability when a canard-strake is added to a wing planform. In addition, the investigation showed the expected further increases in lift coefficient and maximum lift coefficient and improvements in lift-drag polar when two-dimensional vectored thrust is employed at the wing trailing edge; the inability of the canard to trim the configuration at high thrust coefficients and nozzle deflections typical of takeoff and landing; the possibility of using a small nose jet for trim during takeoff and landing; and the generally good transition characteristics needed for short takeoff and landing.

INTRODUCTION

Previous results from wind-tunnel tests of an unpowered fighter research model (ref. 1) showed significant improvements in maximum lift coefficient when a canard and canard-strake were added to the basic wing planform. However, the increased maximum lift coefficient was accompanied by rather high static longitudinal instabilities owing to vortex lift generated by the canard-strake and flow separation over the wing trailing-edge flaps.

One possible solution to the problem of longitudinal instability was to incorporate two-dimensional nozzles at the wing trailing edge in hopes of obtaining favorable power-induced effects. (See refs. 2 and 3.) A larger scale model, identical in shape to the model reported in reference 1, was built, but this model had two-dimensional rectangular nozzles at the wing trailing edge near the root. This configuration, referred to in this report as the original configuration, showed favorable power-induced effects, increased maximum lift coefficients, improved lift-drag polars, and reduced static longitudinal instabilities. Data for this configuration were reported in references 4 to 7. The configuration was, however, very much out of trim at the high lift coefficients

because of the nose-down pitching moments produced by the trailing-edge flaps and both direct and induced power effects.

In order to develop a configuration which could be trimmed, as well as to represent a transonic fighter configuration more closely, a new wing-canard was designed with planform, twist, camber, and thickness appropriate for transonic maneuvering. (See refs. 5 to 7.) This wing-canard configuration, which was constrained to use the two-dimensional nozzles and fuselage from the model of reference 4, had fairly high leading-edge sweeps of 50° on both the wing and the canard. The configuration was designed for a lift coefficient of 1.0, corresponding to a maneuver condition, and had twists which varied from 0° at the root to -12° and -7° at the tip on the wing and canard, respectively. A second wing-canard configuration with lower twists of -6° and -3.5° was used to represent the takeoff and landing or 1g flight case. The data from this configuration, referred to here as the new configuration, have been reported in references 8 and 9.

Both wing-canard configurations were tested in the Langley V/STOL tunnel to determine the longitudinal aerodynamic characteristics with and without power. Data were obtained at angles of attack from -2° to 42° at Mach numbers from 0.12 to 0.20. Nozzle and flap deflections ranged from 0° to 40°. The basic leading edge could be drooped from 0° inboard to 20° at the tip. Canard incidences ranged from -20° to 10°. Thrust coefficients ranged from 0 to 2.0 so that both the maneuvering coefficients (0.1, 0.2, and 0.3) and takeoff and landing coefficients (1.0, 1.5, and 2.0) could be covered. All configurations had a nose jet available. Limited data were obtained in a representative vertical or short takeoff and landing (V/STOL) configuration. These data were obtained at angles of attack of 0° and 10°, at velocity ratios from 0 to 1.0, with the rear nozzles deflected 60° and 90°, with flaps deflected 60°, and with the nose jet thrusting downward.

These data have been reported under various formal and informal covers. (See refs. 4 to 9.) This report summarizes the results of the effects of power on the low-speed longitudinal aerodynamic characteristics of these two wing-canard fighter-type configurations.

SYMBOLS AND ABBREVIATIONS

All data have been reduced to standard coefficient form and are presented in the stability axis system. The nose of the model is located at body station 50.8 cm (20.0 in.). The model moment centers were at body station 135.66 cm (53.41 in.) for the original configuration and at body station 191.85 cm (75.53 in.) for the new configuration. All measurements and calculations were made in U.S. Customary Units; however, all data contained in this report are given in both SI and U.S. Customary Units. (See ref. 10.)

A	aspect ratio
A_j	jet area, m^2 (ft^2)
B.S.	body station

b span, m (ft)

C_D net force coefficient in drag direction, $\frac{\text{Drag}}{q_\infty S}$

$C_{D,e}$ equivalent thrust-removed drag coefficient, $C_D + C_T \cos(\alpha + \delta_N)$

$C_{D,min}$ minimum drag coefficient, power off

C_L lift coefficient, $\frac{\text{Lift}}{q_\infty S}$

$C_{L,e}$ equivalent thrust-removed lift coefficient, $C_L - C_T \sin(\alpha + \delta_N)$

C_{L_α} lift-curve slope, deg^{-1}

$\Delta C_{L,\Gamma}$ thrust-induced lift parameter, $C_L - C_T \sin(\alpha + \delta_N) - C_L|_{C_T=0}$

C_m pitching-moment coefficient, $\frac{\text{Pitching moment}}{q_\infty S\bar{c}}$

$C_{m,e}$ equivalent thrust-removed pitching-moment coefficient, $C_m + \left(\frac{\bar{x}}{\bar{c}}\right)C_T \sin \delta_N$

C_T thrust coefficient, $\frac{\text{Thrust}}{q_\infty S}$

c wing or canard chord, m (ft)

$\bar{c}$ mean aerodynamic chord, m (ft)

c_l section lift coefficient, $\frac{\text{Section lift}}{q_\infty c}$

c_p pressure coefficient, $\frac{p - p_\infty}{q_\infty}$

Δc_p net pressure coefficient, $(c_p)_{\text{lower}} - (c_p)_{\text{upper}}$

D drag, N (lbf)

e drag-due-to-lift efficiency parameter, $\frac{\left(C_L - C_L|_{C_{D,min}}\right)^2}{(C_D - C_{D,min})\pi A}$

i_c canard incidence, deg

L lift, N (lbf)

M Mach number

p surface pressure, Pa (lbf/ft^2)

p_∞ free-stream static pressure, Pa (lbf/ft^2)

q dynamic pressure, Pa (lbf/ft^2)

S wing area or area, m^2 (ft^2)

T thrust, N (lbf)

t maximum thickness, m (ft)

V velocity, knots

V_e effective jet velocity ratio, $\sqrt{\frac{q_\infty}{q_j}}$

W.S. wing station

X,Y,Z body axis system

x,y,z distances along body axes, m (ft)

$\bar{x}$ distance from moment center to nozzle hinge line, m (ft)

α angle of attack, deg

δ deflection angle, deg

ε wing or canard twist at tip, positive leading edge up, deg

η nondimensional semispan distance, $\frac{2y}{b}$

Λ sweep angle, deg

Subscripts:

c canard

cp center of pressure

dd	drag divergence
f	flap
j	jet
l	local
le	leading edge
lower	lower surface of wing
max	maximum
measured	data measured in the wind tunnel
min	minimum
m.c.	moment center
N	nozzle
ref	reference
root	plane of symmetry of wing
te	trailing edge
tip	located at semispan distance on wing or canard
upper	upper surface of wing
w	wing
$\perp$	perpendicular
∞	free stream

MODEL DESCRIPTIONS AND TEST CONDITIONS

Photographs of the original and new wing-canard models are shown in figures 1 and 2; planform sketches are shown in figures 3 and 4; and general dimensions are presented in tables I and II. Detailed model descriptions are given in references 4 and 8 and are not included here.

Thrust coefficients were obtained by varying both q_∞ and thrust T. The values of q_∞ and T at a given C_T as well as the corresponding Mach number and Reynolds number based on $\bar{c}$ are given in the following table:

C_T	q_∞		T		Mach number	Reynolds number
	kPa	lbf/ft^2	N	lbf		
Original wing-canard configuration						
0	2.39	50	0	0	0.18	1.51 × 10^6
.2	2.39	50	286	64	.18	1.51
.3	1.48	31	266	60	.14	1.20
New wing-canard configuration						
0	2.87	60	0	0	0.20	1.44 × 10^6
.1	2.87	60	129	29	.20	1.44
.2	2.87	60	262	59	.20	1.44
1.0	1.43	30	654	147	.14	1.37
1.5	.96	20	654	147	.12	1.12
2.0	.96	20	872	196	.12	1.12

To obtain the desired angle-of-attack range, the data were obtained in two phases using different sting-model couplings: a high-angle-of-attack phase, α = 12° to 42°; and a low-angle-of-attack phase, α = -2° to 26°. Overlapping data occurred from α = 12° to 26°.

The V/STOL data were obtained at prescribed effective velocity ratios $V_e = \sqrt{q_\infty/q_j}$ rather than with thrust coefficients, and, as in the previous table, both T and q_∞ were varied to obtain the desired effective velocity ratios. The effective velocity ratio, free-stream dynamic pressure, and thrust for various velocity ratios are given in the following table:

V_e	q_∞		T	
	kPa	lbf/ft^2	N	lbf
Original wing-canard configuration				
0	0	0	439	98
.13	.24	5	439	98
.26	1.00	21	439	98
.38	2.20	46	439	98
.51	2.87	60	322	72
.64	2.87	60	201	45
New wing-canard configuration				
0	0	0	403	90
.05	.03	1.7	↓	↓
.10	.13	2.8		
.20	.55	11.5		
.30	1.24	26.0		
.40	2.21	46.3		
.50	3.45	72.1		

PRESENTATION OF RESULTS

The complete tabulated data for these configurations are given in references 4 and 8. Selected data which are representative of the overall trends for each configuration are presented below and are not intended to show all possible configuration combinations, control deflections, and/or thrust coefficients obtained in the several investigations. The high-angle-of-attack data are plotted as symbols with + inside; the low-angle-of-attack data are plotted as plain symbols. It should be noted that the original wing-canard configuration had a moment center selected so that $\partial C_m/\partial C_L = 0.05$, and the data are presented for that moment center here. However, after the analysis of the original data and the design of the new wing-canard, a moment center represented by $\partial C_m/\partial C_L = 0.15$ appeared more appropriate, and the data for the new wing-canard configuration are presented for the higher instability. These two moment centers are retained in this paper to maintain consistency with related, previously published reports.

The run number presented in each figure corresponds to the same run number in references 4 and 8 for easy comparison with the tabulated results. The order of data presentation in the figures is as follows:

DISCUSSION

Original Wing-Canard Configurations

Geometry effects.- The effects of basic configuration geometry on the longitudinal aerodynamic characteristics are presented in figure 5. As expected, the addition of the canard increased C_{L_α} and $C_{L,max}$, improved the lift-drag polar at angle of attack, and decreased the static longitudinal stability over the wing-alone configuration. The addition of the strakes further increased $C_{L,max}$ and improved the lift-drag polar but caused a further decrease in static stability at the higher angles of attack. Since these effects are due to strake vortex flow, there were no changes in the longitudinal characteristics at low angles of attack $\alpha \leq 10^o$, where vortex flow is not appreciable. Figure 6 shows that a similar decrease in stability occurs as the nozzles and wing flaps are deflected from 10^o to 30^o on the wing-canard configuration. This decrease in stability is caused by flow separation on the nozzles and flaps at high angles of attack. This flow separation is also evident as reduced increments in C_L as the nozzles and flaps are deflected from 10^o to 30^o in comparison with the increments in C_L when the nozzles and flaps are deflected from 0^o to 10^o. These two effects, strake vortex flow and nozzle/flap deflection, are additive, and as shown in figure 7 the configuration with a strake and the flaps down can become rather unstable at high angles of attack.

Effects of thrust.- The effects of moderate thrust coefficients ($C_T = 0.2$ and 0.3) are presented in figure 8. For the wing-canard configuration, the use of thrust essentially eliminated the pitch-up. As expected, thrust also increased C_{L_α} and $C_{L,max}$ and improved the lift-drag polar, especially at the 30^o nozzle/flap deflection. These powered lift benefits are generally associated with three phenomena: direct thrust, attached flow through boundary-layer control, and induced circulation lift. In order to determine which effects were present, the direct thrust contributions were removed from the data. These equivalent thrust-removed data were defined as follows:

$$C_{L,e} = C_L - C_T \sin(\alpha + \delta_N)$$

$$C_{D,e} = C_D + C_T \cos(\alpha + \delta_N)$$

$$C_{m,e} = C_m + \left(\frac{\bar{x}}{\bar{c}}\right) C_T \sin \delta_N$$

where $\bar{x}/\bar{c}$ is the nondimensional distance from the moment reference center to the nozzle hinge line, and for this configuration $\bar{x}/\bar{c} = 0.90$. The thrust-removed data $\delta_N = \delta_f = 0^o$ in figure 9(a) collapsed to essentially the power-off ($C_T = 0$) data at the low angle of attack, indicating that only direct thrust effects were present. At the higher angles of attack, the data at $C_T = 0.2$ and 0.3 showed improvements over the power-off data, indicating that either of the latter two effects were present. However, since there are no differences between the data at $C_T = 0.2$ and $C_T = 0.3$, only a boundary-layer control which attached the flow over the nozzles and wing trailing edge appeared to be present. If induced circulation lift had been present, increased increments between those data as C_T was increased would have occurred. These effects can be seen somewhat more dramatically with $\delta_N = \delta_f = 30^o$ in figure 9(b). The thrust effects attached the flow over the nozzles and flaps, and the data showed an increment between $C_T = 0$ and $C_T = 0.2$ and 0.3. However, little or no induced circulation was present, since there was little difference between the data at $C_T = 0.2$ and $C_T = 0.3$ except at very high angles of attack. The difference at the high angle of attack is probably due to the occurrence of larger regions of separation, which are influenced more at the higher value of C_T.

It should be noted that this configuration was out of trim when the nozzle or flaps were deflected because the canard incidence was fixed. Also, this configuration had little or no design optimization because a moderately swept, untwisted planform with circular-arc airfoil sections was used rather than a twisted, cambered planform more appropriate for a transonic maneuvering fighter. This lack of design optimization was evident in the low values of the drag-due-to-lift efficiency factor e shown in figure 10. Although the addition of a strake and power to the basic wing-canard configuration improved the situation somewhat, the configuration still had a rather low efficiency ($e \approx 0.50$ to 0.55).

New Wing-Canard Configuration

Geometry effects.- Effects of the basic configuration geometry on the longitudinal aerodynamic characteristics are presented in figure 11. (A discussion of the design of the new wing-canard geometry is given in the appendix.) As expected and as seen in the original configuration, addition of the canard to the wing-along configuration increased both C_{L_α} and $C_{L,max}$, increased $\partial C_m/\partial C_L$, and improved the lift-drag polar. Addition of the strake further improved $C_{L,max}$, the lift-drag polar, and caused longitudinal instability similar to that on the original configuration. Again, these effects were seen only above $\alpha \approx 10^o$, where vortex flow on the strake was appreciable. The effects of flap deflection are present in figure 12. The typical increases in C_L, improvements in lift-drag polar, and increases in nose-down pitching moment are seen, and these effects increase as C_T increases. The decrease in stability caused by flap deflection on the original configuration (noted in fig. 4) was not seen in these data because the 30^o flap deflection, which caused badly separated flow on the original configuration, was eliminated on the new configuration. This deletion as well as the removal of the strake for most of the testing produced a new configuration that showed little decrease in sta-

bility with or without power in comparison with the original configuration. For this reason, a new configuration longitudinal instability of 15 percent ($\partial C_m/\partial C_L = 0.15$) appeared within reason, and the pitching-moment data for the new configuration are presented as such.

Thrust effects.- The effects of thrust coefficients from 0 to 2.0 on the longitudinal characteristics are presented in figure 13. As expected, the general trends are the same as for the original configuration, with increasing C_{L_α}, $C_{L,max}$, and improvements in lift-drag polar with increasing C_T. Thrust also reduced the longitudinal instabilities, and the magnitude of these effects tends to be slightly larger than for the original configuration. Since the wing trailing edge of the new configuration is swept aft of the nozzles, any power-induced effects would tend to extend farther out the wing span than on the original configuration, where the trailing edge is swept slightly forward of the nozzle. Therefore, the thrust-induced effects should tend to be larger on the new configuration. As on the original configuration, the new configuration tends to be out of trim at the high thrust coefficients or high nozzle/flap deflections. However, because of the high-static instability allowed on the new configuration, it is in trim at low thrust coefficients and low nozzle/flap deflections.

The thrust-removed aerodynamic data are presented in figure 14. Since the new configuration planform and moment center are different from those on the original configuration, the distance from the nozzle hinge line to the moment center was different ($\bar{x}/\bar{c} = 1.071$). For comparison, the $\Delta C_{L,\Gamma}$ for both the wing-alone and the wing-canard configurations are shown in figure 15. As on the original configuration, the primary thrust effect shown by the data in figure 15 is boundary-layer control rather than induced circulation lift-coefficient increments. At low thrust coefficients ($C_T = 0.1$ and 0.2), the slope of $\Delta C_{L,\Gamma}$ is high, while at high thrust coefficients ($C_T = 1.0$ and 2.0), the slope is rather flat. The high slope region indicates boundary-layer control at low C_T, which tends to reattach separated flow regions on the trailing edge near the nozzle. The increases in the effect at higher angles of attack are indicative of larger separation regions, which when reattached give larger increments in lift. However, at all angles of attack, once the flow is attached, the improvements in $\Delta C_{L,\Gamma}$ at $C_T = 1.0$ or 2.0 are small. This result indicates that predominantly direct thrust effects rather than induced circulation effects are present at high C_T.

Canard incidence.- The effects of canard incidence on the longitudinal aerodynamics of both the high- and low-twist configuration are presented in figure 16. An interesting trend exists in the high-twist configuration at the higher angles of attack: the best lift-drag polar and highest $C_{L,max}$ occur with $i_c = -10^\circ$. This optimum occurs because of the wing-canard interference, which is primarily driven by the canard downwash on the wing. Higher canard deflections, although increasing the canard load, produce a larger downwash, which unloads the inboard portion of the wing and reduces total C_L. Lower canard deflection unloads the canard and reduces the downwash on the wing, but the total effect is a reduction in C_L. These trends are shown in detail in figure 17 for three selected wing-canard configurations and thrust-coefficient combinations. Although the magnitudes differ, the general trends are present in all these configurations; at the lower angles of attack, the lower canard inci-

dence (i_c = -10° to -20°) reduces the configuration C_L as expected, while i_c between -5° and 10° tends to produce almost constant C_L. There were no high-angle-of-attack data obtained for the low-twist configuration, and the i_c range was reduced to ±10°, so that some of these trends are not as obvious in the data. However, the range of C_L between i_c = 0° and 10° is small like that seen in the high-twist configuration data. This result indicates that the same wing-canard interference trends are present with the low-twist configuration.

One of the major efforts of this investigation was to determine the trim capability of the canard. Figure 16 shows that at low thrust coefficients and/or low nozzle deflections, the high-twist configuration could be trimmed to $C_{L,max}$ and the low-twist configuration to α = 26°, the highest angle-of-attack data obtained. A typical trimmed lift-curve and lift-drag polar are presented in figure 18. These indicate that the high-twist configuration, with C_T = 0.2 and $\delta_f = \delta_N$ = 20°, trims to $C_{L,max}$ = 3.0. At increased C_T or δ_N (i.e., $C_T \geq 1.0$ and $\delta_N = \delta_f \geq 20°$), the nose-down pitching moments produced by the deflected thrust could not be trimmed by the canard on either configuration. An analysis using direct thrust from a nose jet as a method for trimming the configuration at high C_T and δ_N is discussed in a later section of this paper.

Comparison of Configurations

A direct comparison between the original and new configurations is difficult because of the different planforms and varying canard-to-wing area ratios. The contribution of the canard to the total lift when the exposed canard area is taken into account is shown in figure 19. The three configurations shown in the figure represent the original wing-canard, the new (high-twist) wing-canard, and a wing-canard from reference 1 similar, except for a wing with higher sweep (Λ_{le} = 60°), to the original wing-canard. The addition of the canard increases the maximum lift more than the increase that would be provided by addition of equivalent exposed canard area to the wing planform for all these cases. The improvement is not as striking for the two configurations with higher wing sweeps, since the leading-edge vortex is clearly well developed and the wing-alone in both cases attains higher maximum lift coefficient. The effect of the canard for both configurations with higher sweep is a modest increase in maximum lift coefficient.

A comparison between the performance data for the original configuration and for the new wing-canard configuration is presented in figure 20. The lift and drag coefficients are based on wing area plus exposed canard area; in comparison to the original configuration both with and without power, the new configuration has higher $C_{L,max}$ and an improved lift-drag polar. Throughout the C_L range (above C_L = 0.5), the induced drag efficiency parameter (fig. 20(b)) for the new wing with high or low twist is higher than the induced drag efficiency of the original configuration.

Trimming for STOL Operations

As mentioned earlier, the canard would not trim the new configuration for high thrust coefficients and nozzle/flap deflections, such as might be required for short take-off and landing (STOL) operations. The use of a nose jet for pitch trim as a method by which fighter-type configurations could attain STOL performance was presented in reference 9. The experimental data corresponding to a takeoff or landing condition, in figures 21(a) and 21(b), respectively, illustrate this method.

Reference 9 shows that takeoff lift coefficients may run as high as 2.5 or more for short takeoff operations. It can be seen in figure 21(a) that at a takeoff angle of attack of 16°, the new configuration with $\delta_f = \delta_N = 20^{\circ}$ and $C_T = 1.0$ produces a lift coefficient of 2.4 and has excess thrust for initial acceleration and climb. However, as shown by the shaded area in figure 21(a), the nose-up pitch capability of the canard is exceeded by 0.1 to 0.2 over the angle-of-attack range from 0° to 24°; in particular, this capability is exceeded by 0.165 at $\alpha = 16^{\circ}$. If the basic ($i_c = 0^{\circ}$) data were trimmed at $\alpha = 16^{\circ}$ by a nose jet, then a lift-coefficient increment due to the jet thrust of 0.173 would be required, provided the jet were located $2.21\bar{c}$ ahead of the configuration moment center. This jet thrust would produce the dashed curves in the figure if the interference effects, usually adverse, from the jet are small. The resulting configuration would be trimmed at $\alpha = 16^{\circ}$ with $C_L = 2.57$, have excess thrust for acceleration and climb, and have nose-up pitch capability from the canard for longitudinal control.

The short landing operation can be more demanding on the configuration aerodynamics than takeoff not only because the lift coefficient must be high and the pitching moments trimmed, but also because the drag level must be such that descent is possible. The above requirements normally involve adjustment of thrust coefficient, nozzle deflection, and canard incidence to assure that a trimmed lift coefficient is attained at a drag level that allows reasonable descent angle. However, for this configuration, these requirements could not be met without such additional pitch control as could be provided by thrust from a nose jet. Reference 9 shows that the landing lift coefficient can run as high as 2.4. Figure 21(b) illustrates how the trimmed lift coefficient might be obtained on the new configuration. As in the takeoff operation, there is a reasonable limit to the angle of attack suitable for landing and such a limit is assumed to be $\alpha = 16^{\circ}$. The data indicate that the new configuration at $\alpha = 16^{\circ}$ with $\delta_f = \delta_N = 40^{\circ}$ and $C_T = 1.0$ produce a lift coefficient of 3.06 and a drag level corresponding to a reasonable descent angle of -3° to -4°. However, as shown by the shaded area in the figure, the nose-up pitch capability of the canard is exceeded by 0.5 to 0.6 over the angle-of-attack range from 0° to 24°. If the thrust coefficient is reduced so that $C_L = 2.4$ at $\alpha = 16^{\circ}$, then the dashed curve shown in the figure may be generated. The nose-up pitch capability is still exceeded, and now the drag is such that a very high descent angle of -11° or -12° must be flown. If direct thrust is used to trim the configuration at $\alpha = 16^{\circ}$, then a lift-coefficient increment of 0.183 is required for the nose jet, and the second dashed curve is generated. The configuration now has a slight excess in lift coefficient, and one or more of several variables, i.e., angle of attack, thrust coefficient, nozzle deflection, and canard incidence, may be adjusted to maintain a trimmed lift coefficient of 2.4.

It should be pointed out that this approach was not intended to approximate a vertical takeoff and landing configuration, but only to represent a possible method whereby the basic longitudinal trim requirements of a fighter configuration were met through the use of small amounts of direct lift. In these two cases, a nose jet with thrust levels of 7 to 8 percent of total lift was used. These trim requirements can be met by moving the moment center about 15 to 20 percent aft if the high, canard fixed instability can be tolerated. If, however, the canard is allowed to float so that it has no effect on configuration stability, this configuration is statically stable even with the 20-percent-aft movement of the moment center. To determine if the center of gravity of a proposed airplane could be moved as much as 20 percent would require a detailed weight estimate of the configuration; such an estimate is beyond the scope of this paper. In a final configuration, it may be reasonable to have a combination of floating canard, aft center of gravity, and nose jet. However, if a nose jet is to be used, an examination of the transition aerodynamics of the configurations becomes necessary, since some of the flight operations can be below normal power-off stall speeds, where a large part of the configuration lift is produced by direct and induced thrust effects.

Transition Aerodynamics

Although the two wing-canard configurations were tested primarily to obtain high-angle-of-attack and conventional takeoff and landing data, both were tested as V/STOL configurations with a nose jet used to provide direct thrust for lift and pitch trim. These data have been compared with data for several previous V/STOL configurations (refs. 11 to 14) that have been tested in the Langley V/STOL tunnel and 300-MPH 7- by 10-foot low-speed tunnel. Because the wing-canard configurations have the rear nozzles at the wing trailing edge, they showed beneficial jet interference at transition velocity ratios. This is shown for the new wing-canard configuration in figure 22 together with data for the Harrier-type configuration showing the detrimental jet interference typical of configurations having nozzles under the wing. In order to compare one configuration directly with another, figure 23(a) presents L/T versus V_e for several configurations. From this more traditional approach, the new wing-canard appears to be the superior configuration. However, this approach does not account for wing-to-jet area ratios that may be different on each configuration. If, however, the data are compared as $(L/T)/(A_j/S)$ versus V_e^2, an entirely different relative comparison is evident, as shown in figure 23(b). The parameter $(L/T)/(A_j/S)$ is

$$\frac{L}{T}\frac{A_j}{S} = \frac{A_j}{S}\sin(\alpha + \delta_N) + \frac{C_L\big|_{T=0} V_e^2}{2}$$

where the first term is an intercept and a function of jet area and the second term is a slope and a function of the power-off configuration C_L. Therefore, the higher the power-off C_L, the better the configuration should be in transition. In addition, the larger the disk or jet area, and hence lower disk loading, the better the configuration should be in hover. Several points can be

noted from the experimental data: (1) the $(L/T)/(A_j/S)$ parameter is nearly linear with V_e^2; (2) the slope of the parameter indicates how rapidly the configuration produces wing lift and thus how well it might perform in transition flight; (3) the intercept at $V_e = 0$ indicates how well the configuration would hover; (4) any difference between the data and the calculated $(L/T)/(A_j/S)$ indicates the interference present. The data in figure 23(b) show the same interference trends for the wing-canard and Harrier configurations as figure 22. In figure 23(b) the wing-canard shows a better transition performance but a less efficient hover performance.

These configurations were compared at several angles of attack and nozzle deflections (fig. 24), and the following general trends were noted. Those configurations with nozzles at or near the wing trailing-edge flaps showed generally beneficial interference effects, indicating potentially good transition characteristics. However, these configurations tended to have small nozzle areas and a resultant high thrust loading, which make them poor hovering configurations. Those configurations with nozzles below the wing had a detrimental interference, indicating potentially poorer transition characteristics. However, these configurations usually had larger jet areas and showed better hovering characteristics.

SUMMARY OF RESULTS

Several investigations into the low-speed longitudinal aerodynamic characteristics of two close-coupled wing-canard configurations have indicated the following results:

1. The addition of a canard and strake to a wing planform will increase the lift-curve slope and maximum lift coefficient and improve the lift-drag polars, but vortex flow from the strake and flow separation on the wing trailing-edge flaps may cause a decrease in longitudinal stability, especially at the higher angles of attack. The decrease in stability caused by flow separation on the flap can be reduced through thrust effects which provide boundary-layer control to maintain attached flow over the flaps.

2. As expected, the effects of thrust increase the lift-curve slope and maximum lift coefficient and improve the lift-drag polars primarily through boundary-layer control rather than induced circulation effects.

3. Canard incidence of -10° provides the maximum lift at high angles of attack. Lower canard incidence unloads the canard and reduces downwash effects, reducing total configuration lift coefficient. Higher canard incidence increases the canard load, but the resulting high downwash unloads the inboard portion of the wing to the point where total configuration lift coefficient is again reduced. At lower angles of attack, these effects are not as apparent. However, at canard incidence between -0° and 10°, lift coefficients for the total configuration remain almost constant. This result indicates that as the canard load is increased, it is canceled by the downwash effects unloading the wing.

4. The high-twist or maneuvering configuration will trim to maximum lift coefficient at a thrust coefficient of 0.2. The low-twist or takeoff and landing configuration could be trimmed to an angle of attack of 26°, the maximum angle-of-attack data obtained, at a low thrust coefficient and nozzle deflection. At the high nozzle deflection and high thrust coefficients appropriate for takeoff and landing conditions, the nose-down pitching moments caused by the deflected thrust and flaps could not be trimmed by the canard.

5. A possible method for trimming the new configuration at a high thrust coefficient and nozzle deflection angle is the use of small amounts of direct thrust from a nose jet. This would allow STOL operations but would not imply a VTOL capability.

6. The transition aerodynamics for the two wing-canard configurations indicate better or equal transition characteristics and generally poorer hovering characteristics compared with previous V/STOL configurations.

Langley Research Center
National Aeronautics and Space Administration
Hampton, VA 23665
October 9, 1979

APPENDIX

DESIGN OF NEW WING-CANARD CONFIGURATION

The inability to trim the original configuration (as described in the Introduction) and a desire to test a more realistic transonic maneuvering design led to the new wing-canard configuration shown in figure 25. The planforms of both configurations are overlaid for comparison in figure 26. It can be seen that both configurations used the same fuselage and two-dimensional nozzle, but that the new configuration had higher sweep representative of a more realistic transonic maneuvering configuration. The wing leading- and trailing-edge sweeps were increased to reduce nonlinear compressibility effects and also to move the aerodynamic center rearward so that the nose-down moments due to thrust are reduced for a given level of stability. This resulted in a 40° sweep for the midchord line of the wing. A glove was added inboard on the wing in an attempt to sweep the isobars forward and give a more two-dimensional type loading outboard. The canard has the same leading- and trailing-edge sweeps as the wing; the span of both the wing and canard were equal to those of the original configuration.

An optimum three-dimensional wing design requires iteration with a nonlinear transonic analysis program. Linear theory can be used directly to calculate an initial estimate of the camber surface. Since the intent was to develop a representative configuration to be tested at subsonic speeds and not transonic speeds, the camber surface used was obtained from linear theory as described below.

The wing and canard twist, camber, and thickness were determined as shown in figures 27 and 28. Basically, a supercritical airfoil section known to have good two-dimensional viscous and compressibility characteristics at transonic speed was modified for three-dimensional induced effects. Using the Korn-Garabedian program (ref. 15), a design curve of section-lift coefficient C_l versus drag divergence Mach number M_{dd} was developed for scaled versions of the original airfoil (see fig. 27). Using the nonplanar unified vortex-lattice theory of reference 16, the sweep of the chordwise center of pressure $(x/c)_{cp}$ was calculated at the design Mach number of 0.9. Using the infinite swept-wing analogy $C_{l,\infty} = C_{l,\perp} \cos^2 \Lambda$ and the two-dimensional drag divergence plot, the maximum free-stream section-lift coefficients which were below drag divergence were generated for both the wing and canard.

An inverse program was used to calculate the twist and cambers required on the planform. The local free-stream section lift was chosen as the maximum from figure 27 and held constant across the span, realizing the resulting twists would have to be modified in the root and tip regions. The chordwise loading was chosen as the two-dimensional subcritical loading of the original section. The resulting twists and cambers are shown in figure 28. The twists were fitted approximately to the theoretical distributions as shown by the dashed line. Two versions of the research model, identical except for the levels of twist, were fabricated. The low-twist version was used to study conventional takeoff and landing high-lift performance; the high-twist version, high-angle-of-attack maneuver performance. Both versions had full-span

variable leading- and trailing-edge devices on both the wing and canard. The canard incidence was variable so that trimmed high lift could be obtained. The design procedure was not meant to produce an optimum transonic design. Rather, a configuration that realistically represented one required for transonic maneuvering conditions was intended.

REFERENCES

1. Gloss, Blair B.: Effect of Wing Planform and Canard Location and Geometry on the Longitudinal Aerodynamic Characteristics of a Close-Coupled Canard Wing Model at Subsonic Speeds. NASA TN D-7910, 1975.

2. Winston, Matthew M.; Weston, Robert P.; and Mineck, Raymond E.: Propulsion-Induced Interference Effects on Jet-Lift VTOL Aircraft. AIAA Paper No. 75-1215, Sept.-Oct. 1975.

3. Capone, Francis J.: Supercirculation Effects Induced by Vectoring a Partial-Span Rectangular Jet. J. Aircr., vol. 12, no. 8, Aug. 1975, pp. 633-638.

4. Yip, Long P.; and Paulson, John W., Jr.: Effects of Deflected Thrust on the Longitudinal Aerodynamic Characteristics of a Close-Coupled Wing-Canard Configuration. NASA TP-1090, 1977.

5. Thomas, J.; Paulson, J.; and Yip, L.: Effects of Deflected Thrust on the Stability and Performance Characteristics of a Close-Coupled Canard Fighter Configuration. AIAA Paper No. 77-887, July 1977.

6. Paulson, John W., Jr.; Thomas, James L.; and Yip, Long P.: Low-Speed Power Effects on Advanced Fighter Configuration With Two-Dimensional Deflected Thrust. NASA TM X-74010, 1977.

7. Thomas, James L.; Paulson, John W., Jr.; and Yip, Long P.: Deflected Thrust Effects on a Close-Coupled Canard Configuration. J. Aircr., vol. 15, no. 5, May 1978, pp. 287-292.

8. Paulson, John W., Jr.; and Thomas, James L.: Effect of Twist and Camber on the Low-Speed Aerodynamic Characteristics of a Powered Close-Coupled Wing-Canard Configuration. NASA TM-78722, 1978.

9. Paulson, John W., Jr.; Thomas, James L.; and Winston, Matthew M.: Transition Aerodynamics for Close-Coupled Wing-Canard Configuration. AIAA Paper 79-0336, Jan. 1979.

10. Mechtly, E. A.: The International System of Units - Physical Constants and Conversion Factors (Second Revision). NASA SP-7012, 1973.

11. Mineck, Raymond E.; and Schwendemann, Myles F.: Aerodynamic Characteristics of a Vectored-Thrust V/STOL Fighter in the Transition-Speed Range. NASA TN D-7191, 1973.

12. Margason, Richard J.; Vogler, Raymond D.; and Winston, Matthew M.: Wind-Tunnel Investigation at Low Speeds of a Model of the Kestrel (XV-6A) Vectored-Thrust V/STOL Airplane. NASA TN D-6826, 1972.

13. Wooten, W. H.; and Hoff, G. E.: Deflected Exhaust Jet Effects on V/STOL Fighter Performance. Rep. No. R73AEG279 (Contract No. N00019-72-C0614), Aircraft Engine Group, General Electric Co., July 1973.

14. Winston, Matthew M.: Induced Interference Effects on the Aerodynamic Characteristics of a 0.16-Scale Six-Jet V/STOL Model in Transition. NASA TN D-5727, 1970.

15. Bauer, Frances; Garabedian, Paul; Korn, David; and Jameson, Anthony: Supercritical Wing Sections II. Volume 108 of Lecture Notes in Economics and Mathematical Systems, Springer-Verlag, 1975.

16. Tulinius, J.: Unified Subsonic, Transonic, and Supersonic NAR Vortex Lattice. TFD-72-523, Los Angeles Div., North American Rockwell, Apr. 27, 1972.

TABLE I.- BASIC MODEL GEOMETRY FOR ORIGINAL WING-CANARD CONFIGURATION

Body:	
Length, cm (in.)	231.65 (91.20)
Width, cm (in.)	18.29 (7.20)
Wing:	
A	2.5
S, m^2 (ft^2)	0.59 (6.40)
b, m (ft)	1.22 (4.00)
Λ_{le}, deg	44
$\bar{c}$, cm (in.)	55.98 (22.04)
c_{root}, cm (in.)	81.25 (31.99)
c_{tip}, cm (in.)	16.28 (6.41)
Moment center ($-0.06\bar{c}$) model station from nose, cm (in.)	135.66 (53.41)
Airfoil:	
Section	Circular-arc
t/c at root	0.06
t/c at tip	0.04
Wing flap:	
b_f, exposed, m (ft)	0.76 (2.50)
c_f, side of body, cm (in.)	11.05 (4.35)
c_f, outboard, cm (in.)	3.30 (1.30)
Nozzles:	
b_N, exposed, m (ft)	0.28 (0.90)
c_N, side of body, cm (in.)	10.29 (4.05)
c_N, outboard, cm (in.)	8.76 (3.45)
Canard:	
A_c	2.71
S_c, m^2 (ft^2)	0.25 (2.74)
S_c, exposed, m^2 (ft^2)	0.21 (2.27)
b_c, m (ft)	0.83 (2.72)
Λ_{le}, deg	51.7
c_{root}, cm (in.)	52.73 (20.76)
c_{tip}, cm (in.)	8.59 (3.38)
Airfoil:	
Section	Circular-arc
t/c at root	0.06
t/c at tip	0.04
Height of canard above wing, cm (in.)	11.43 (4.50)

TABLE II.- BASIC MODEL GEOMETRY FOR NEW WING-CANARD CONFIGURATION

Body:	
Length, cm (in.)	231.65 (91.20)
Width, cm (in.)	18.29 (7.20)
Wing:	
A	3.26
S, m^2 (ft^2)	0.46 (4.90)
b, m (ft)	1.22 (4.00)
Λ_{le}, deg	50.0
Λ_{te}, deg	23.4
Twist at tip:	
High	-12.0
Low	-6.0
$\bar{c}$, cm (in.)	42.11 (16.58)
c_{root}, cm (in.)	60.48 (23.81)
c_{tip}, cm (in.)	14.22 (5.60)
Moment center, cm (in.)	B.S. 191.8 (75.53)
Airfoil:	
Section	6 percent aft cambered
t/c at root	0.06
t/c at tip	0.06
Wing flap:	
b_f, exposed, m (ft)	0.76 (2.50)
c_f, side of body, cm (in.)	6.32 (2.49)
c_f, outboard, cm (in.)	2.13 (0.84)
Wing leading-edge droop (constant chord), cm (in.)	6.22 (2.45)
Nozzles:	
b_N, exposed, m (ft)	0.28 (0.90)
c_N, side of body, cm (in.)	10.29 (4.05)
c_N, outboard, cm (in.)	8.76 (3.45)

TABLE II.- Concluded

Canard:	
A_c	2.29
S_c, m (ft)	0.31 (3.32)
S_c, exposed, m^2 (ft^2)	0.17 (1.79)
b_c, m (ft)	0.83 (2.72)
Λ_{le}, deg	50.0
Λ_{te}, deg	23.3
Twist at tip, deg:	
High	-7.0
Low	-3.5
c_{root}, cm (in.)	51.89 (20.43)
c_{tip}, cm (in.)	20.32 (8.00)
Airfoil:	
Section	6 percent aft cambered
t/c at root	0.06
t/c at tip	0.06
Height of canard above wing, cm (in.)	7.75 (3.03)
Canard flap:	
b_f, m (ft)	0.32 (1.06)
$c_{side\ of\ body}$, cm (in.)	7.06 (3.78)
$c_{outboard}$, cm (in.)	3.05 (1.20)
Canard leading-edge droop (constant chord), cm (in.)	5.87 (2.31)

L-76-2218

Figure 1.- Original wing-canard model installed in Langley V/STOL tunnel.

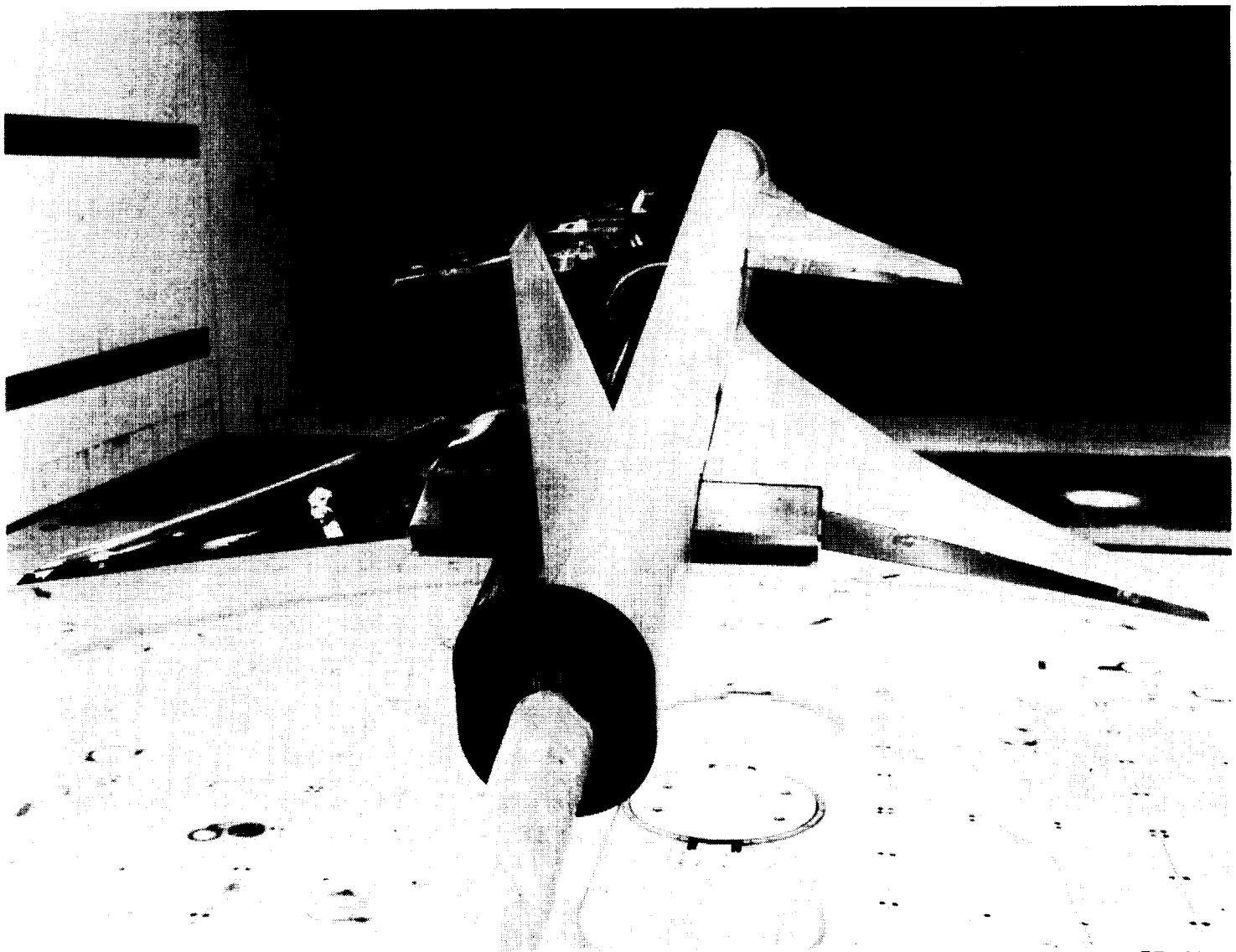

L-77-6077

Figure 2.- Rear view of new wing-canard model installed in Langley V/STOL tunnel.

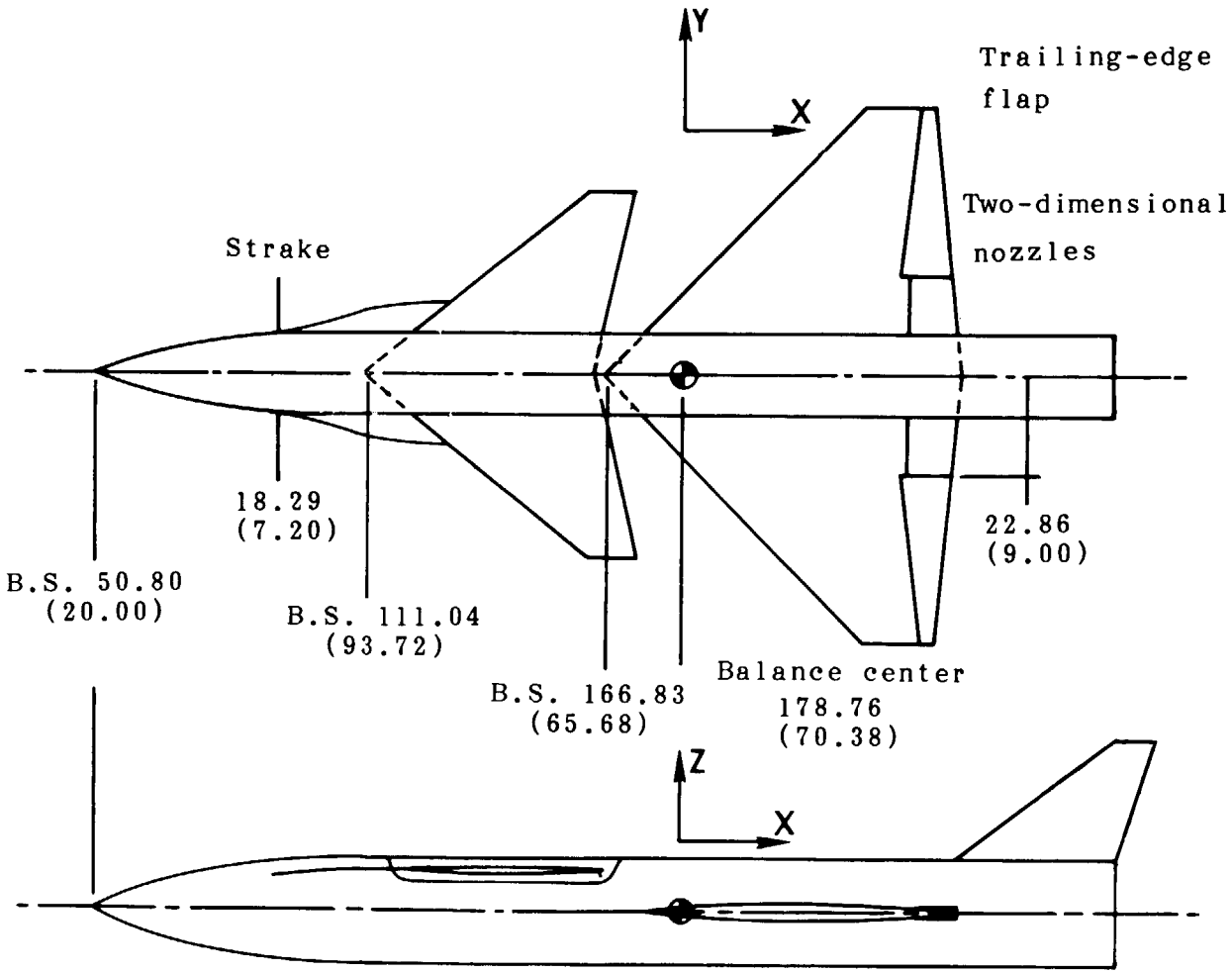

Figure 3.- Original wing-canard model geometry. (Dimensions are in cm (in.)).

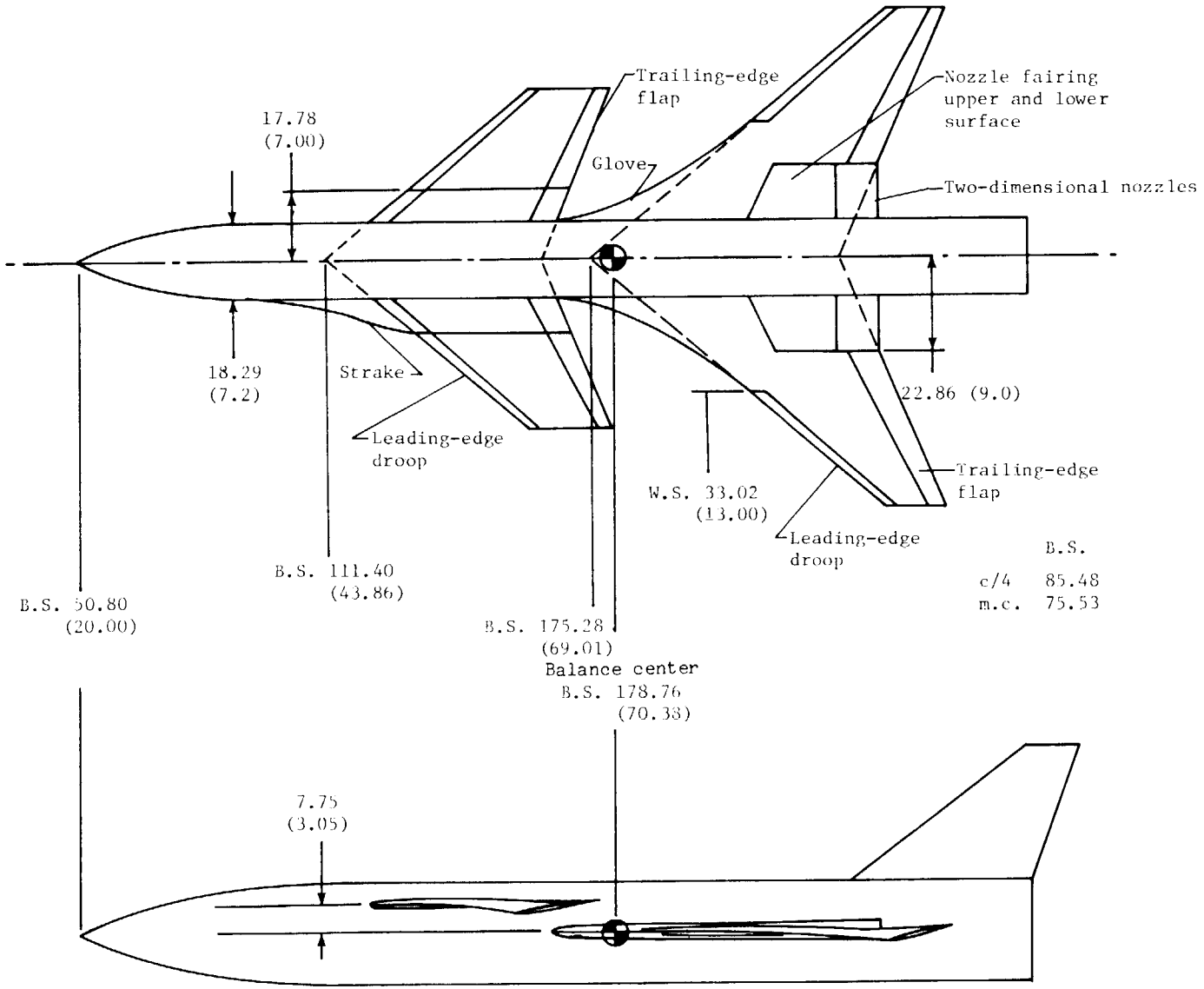

Figure 4.- New wing-canard model geometry. (Dimensions are in cm (in.)).

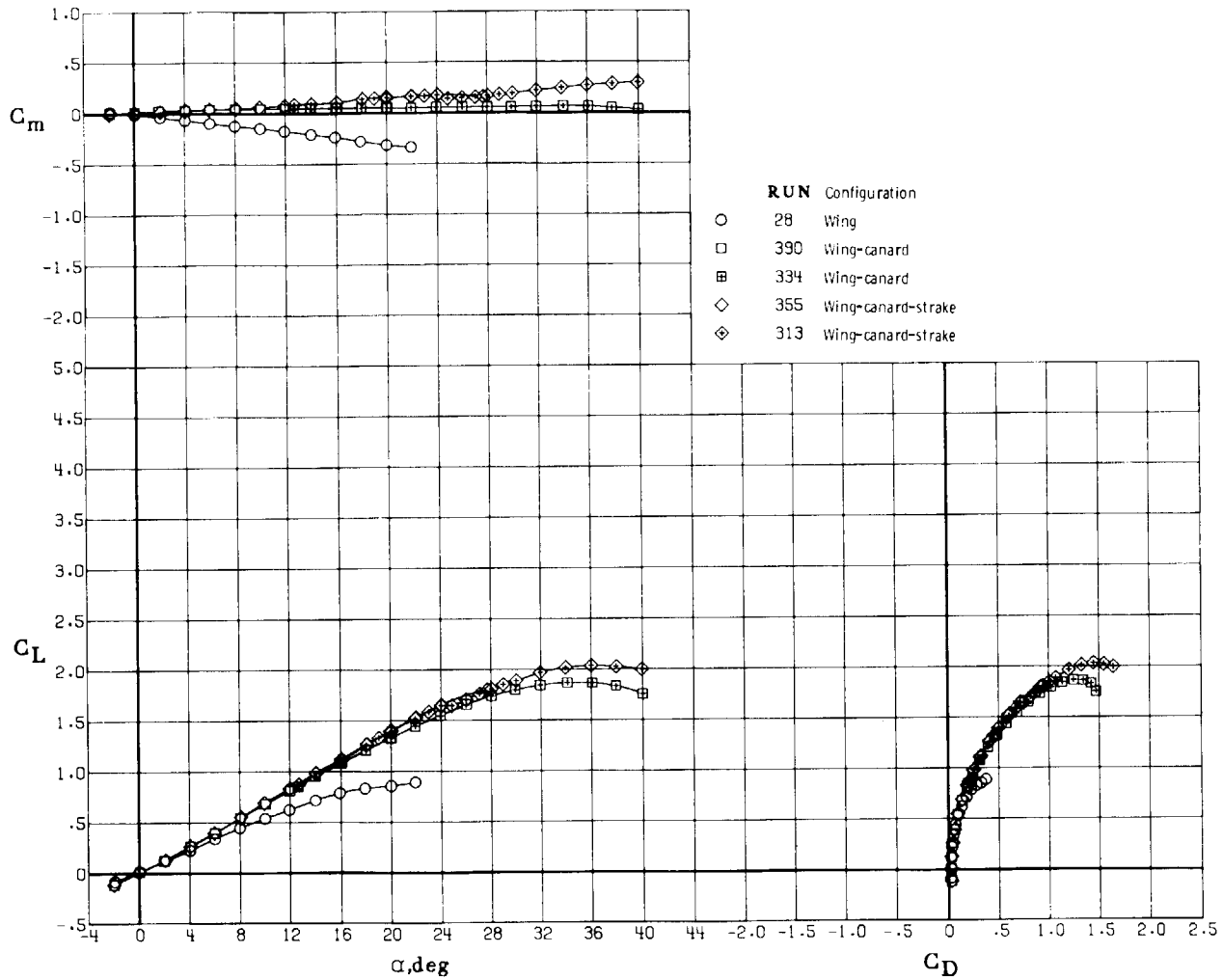

Figure 5.- Effect of adding canard and strake to original wing-alone configuration; $\delta_N = \delta_f = 0^o$ and $C_T = 0$.

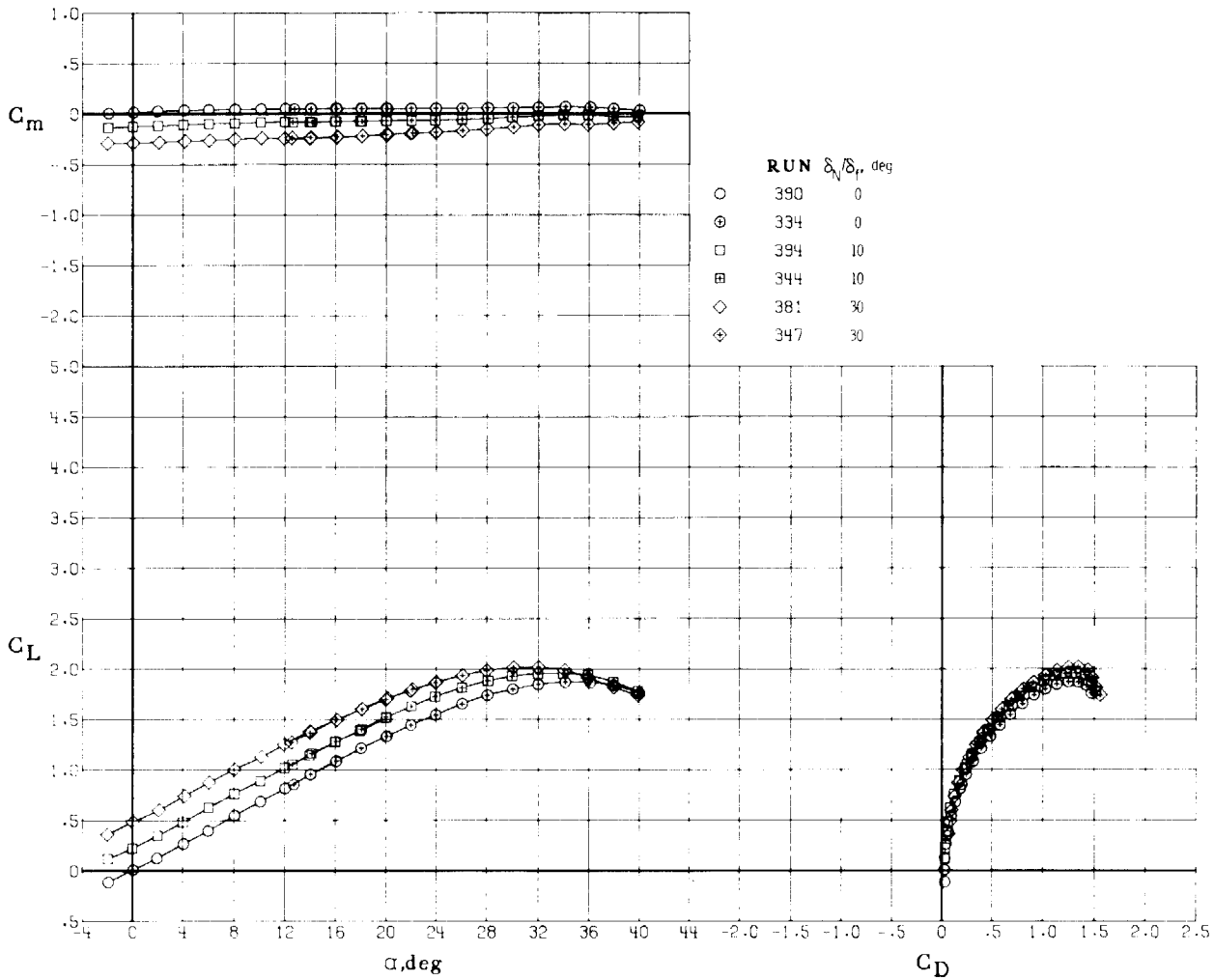

(a) $C_T = 0.$

Figure 6.- Effect of nozzle/flap deflections on longitudinal aerodynamic characteristics of original wing-canard configuration at various thrust coefficients.

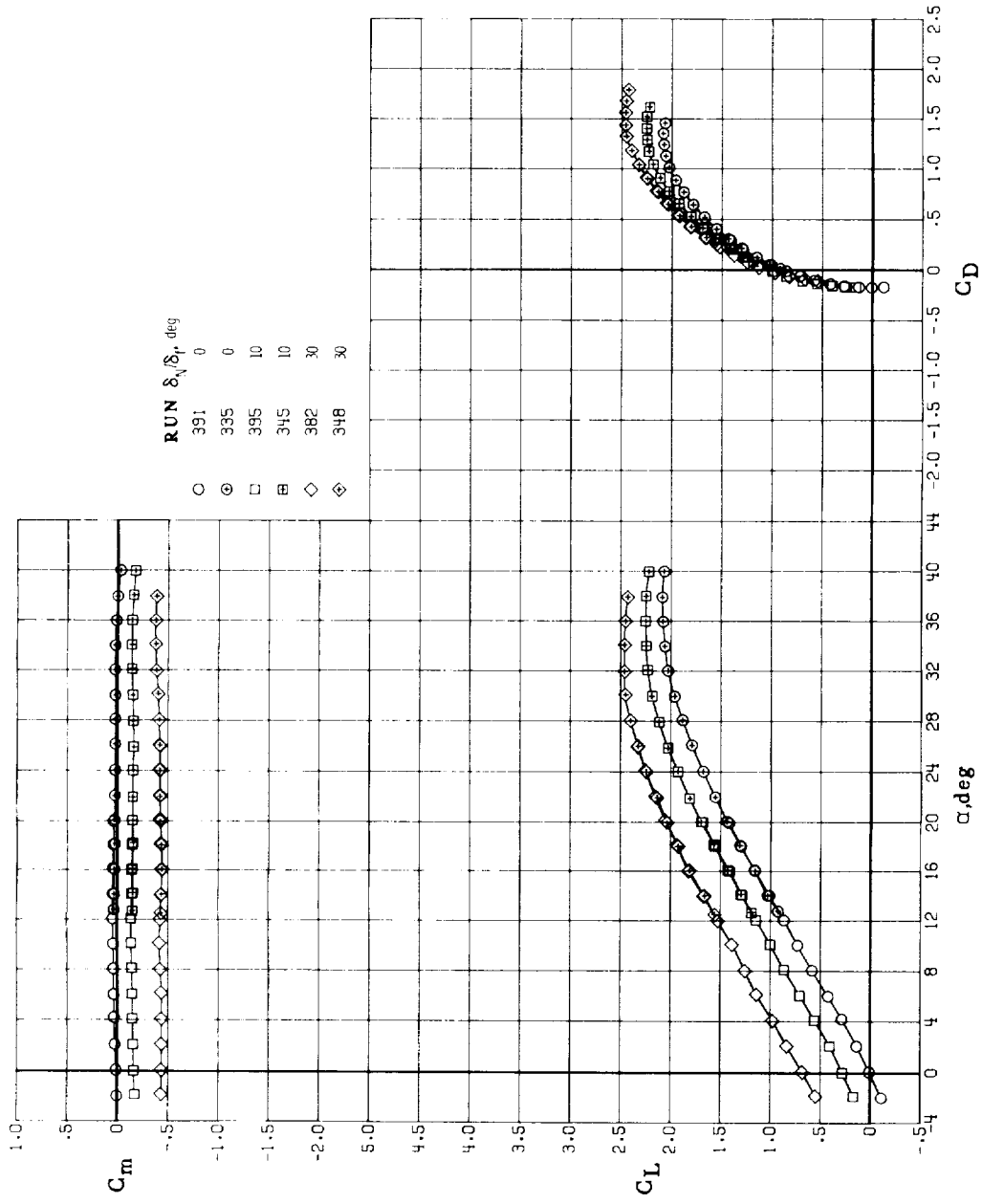

(b) $C_T = 0.2$.

Figure 6.- Continued.

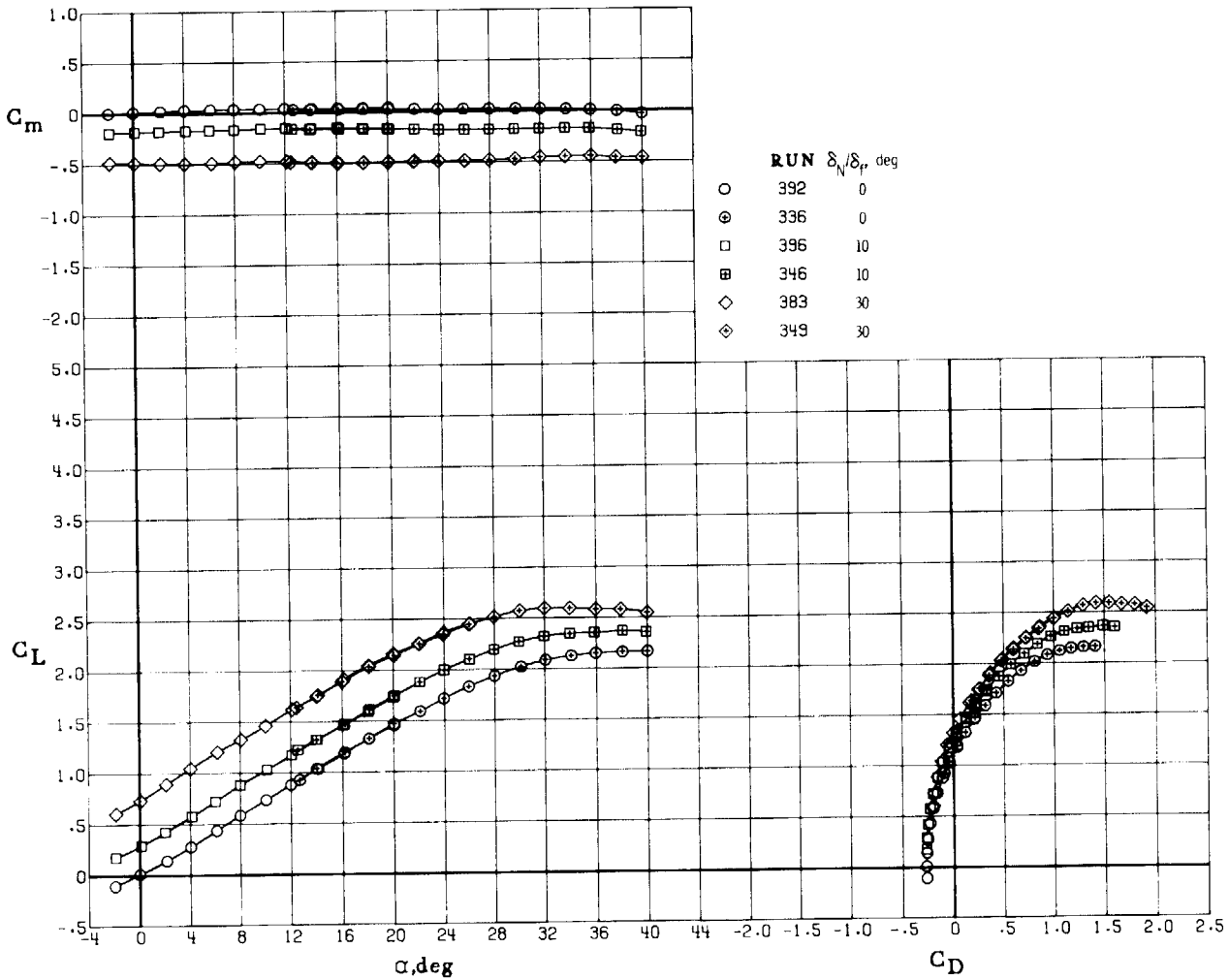

(c) $C_T = 0.3$.

Figure 6.- Concluded.

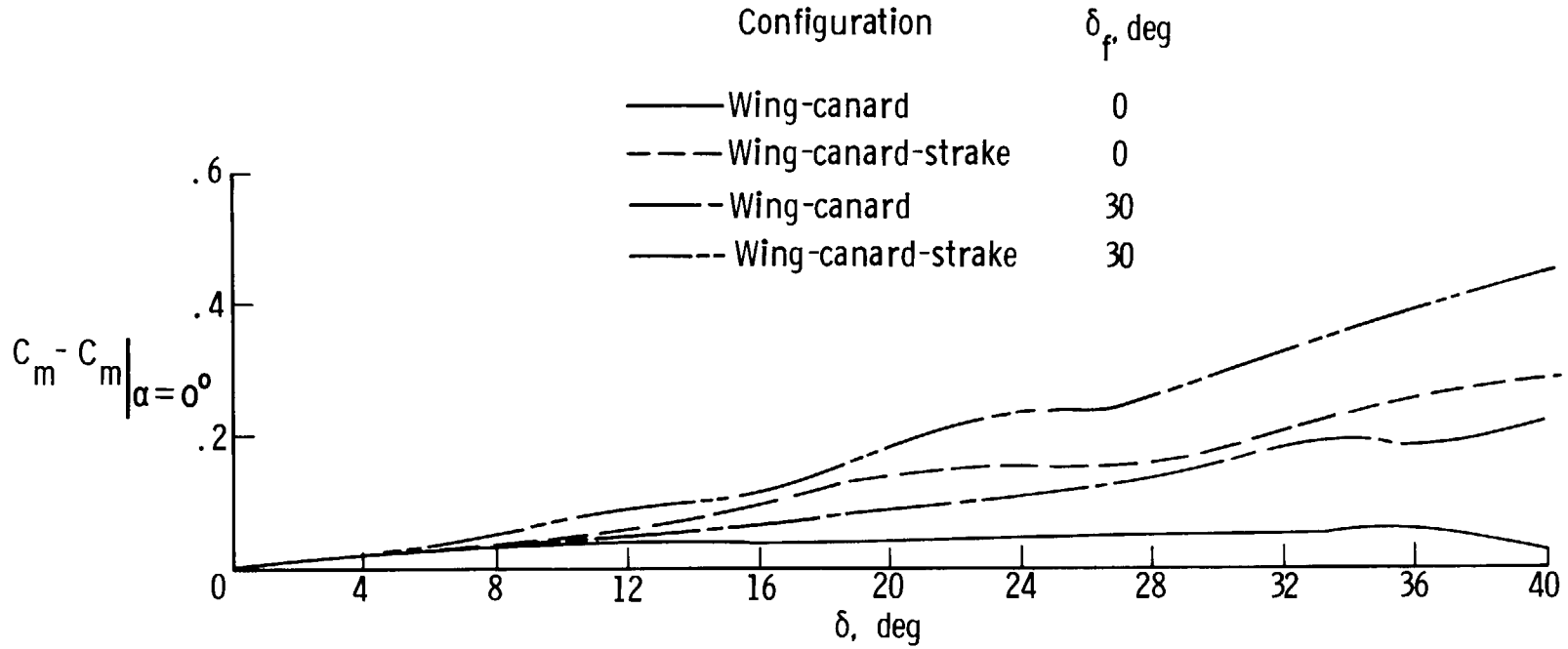

Figure 7.- Pitching-moment coefficient increments due to strake and nozzle/flap deflections for original wing-canard configuration. $C_T = 0$.

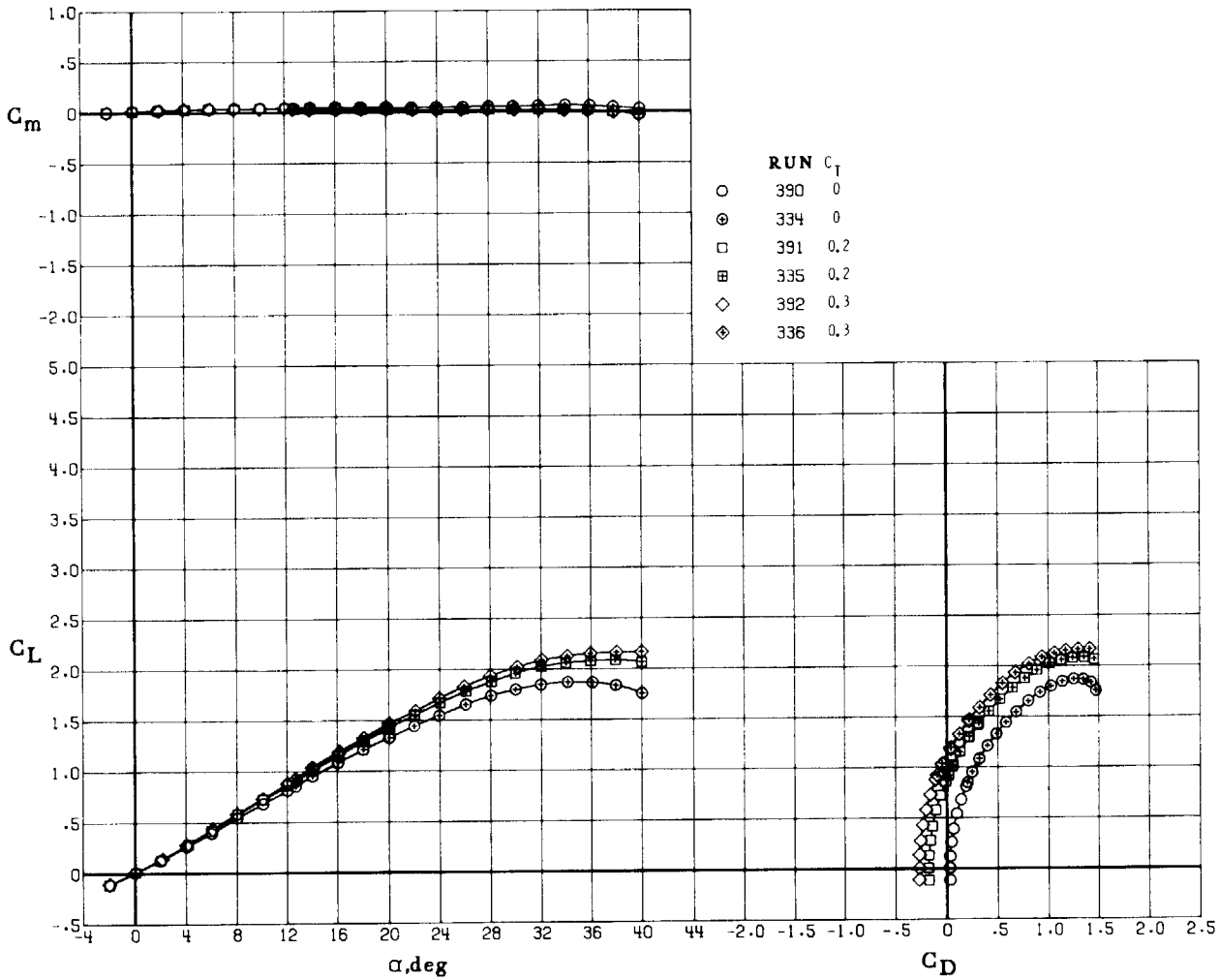

(a) $\delta_N = \delta_f = 0^o$.

Figure 8.- Effect of thrust coefficient on longitudinal aerodynamic characteristics of original wing-canard configuration with various nozzle/flap deflections.

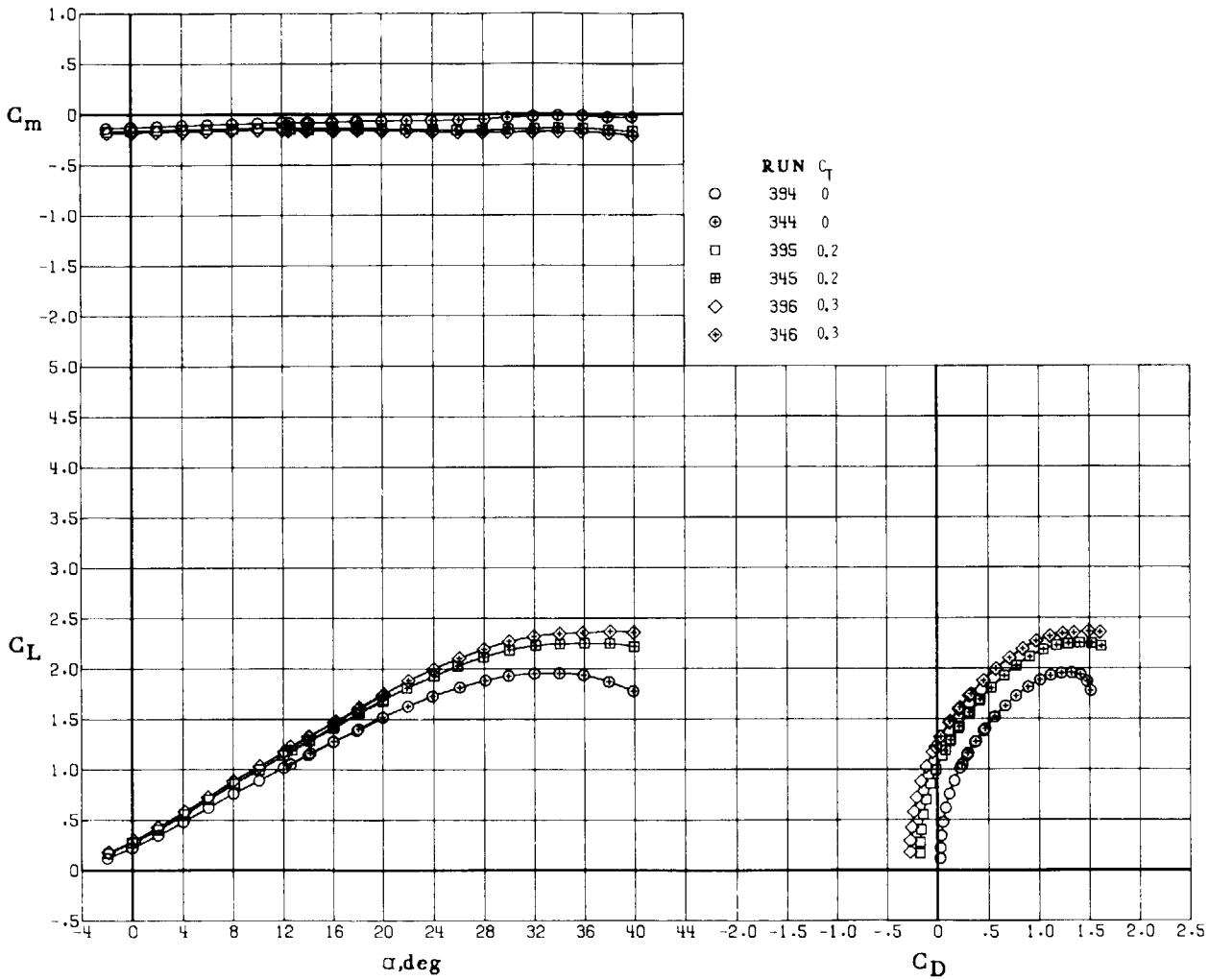

(b) $\delta_N = \delta_f = 10^o$.

Figure 8.- Continued.

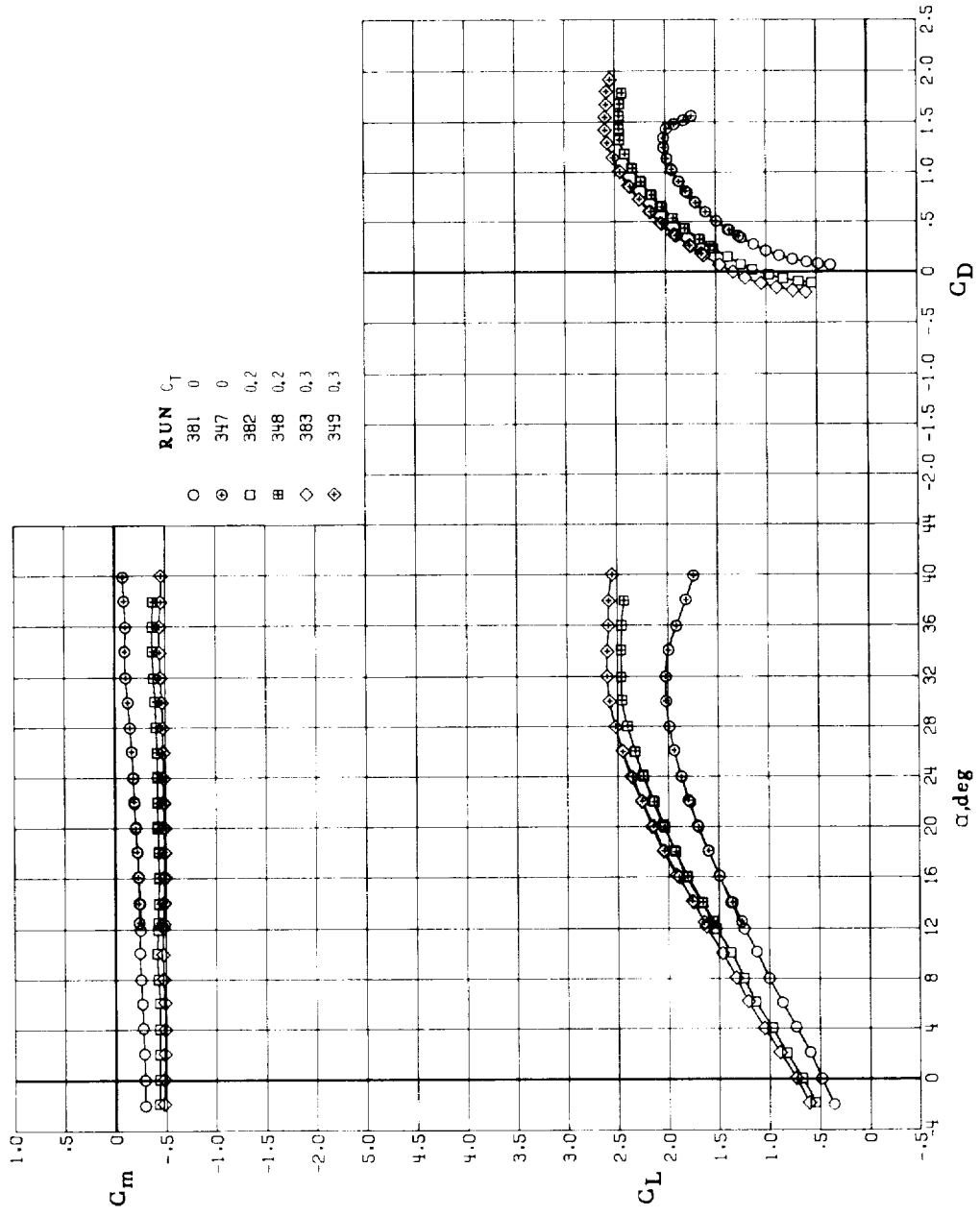

(c) $\delta_N = \delta_f = 30^o$.

Figure 8.- Concluded.

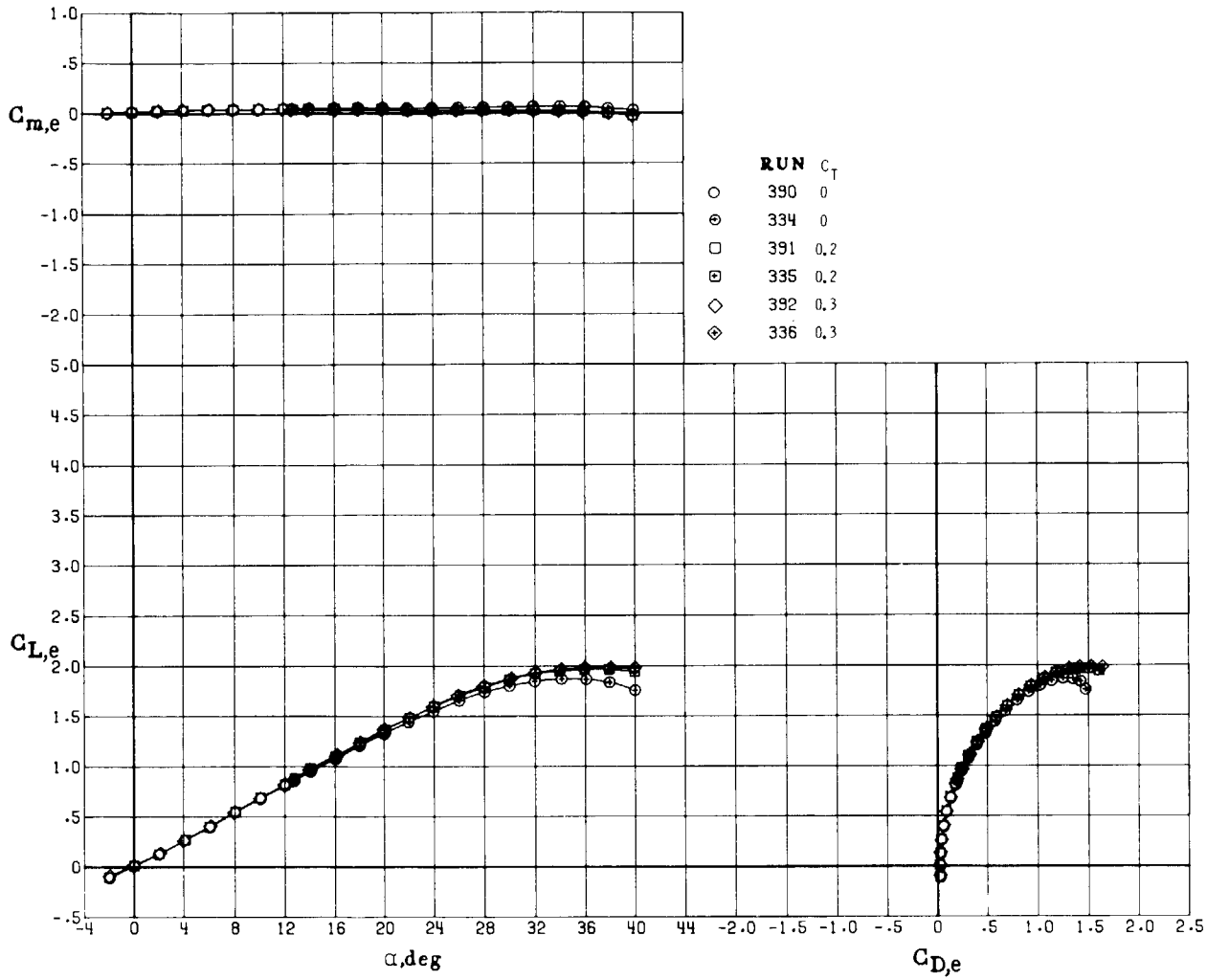

(a) $\delta_N = \delta_f = 0^o$.

Figure 9.- Effect of thrust coefficient on thrust-removed longitudinal aerodynamic characteristics of original wing-canard configuration at various nozzle/flap deflections.

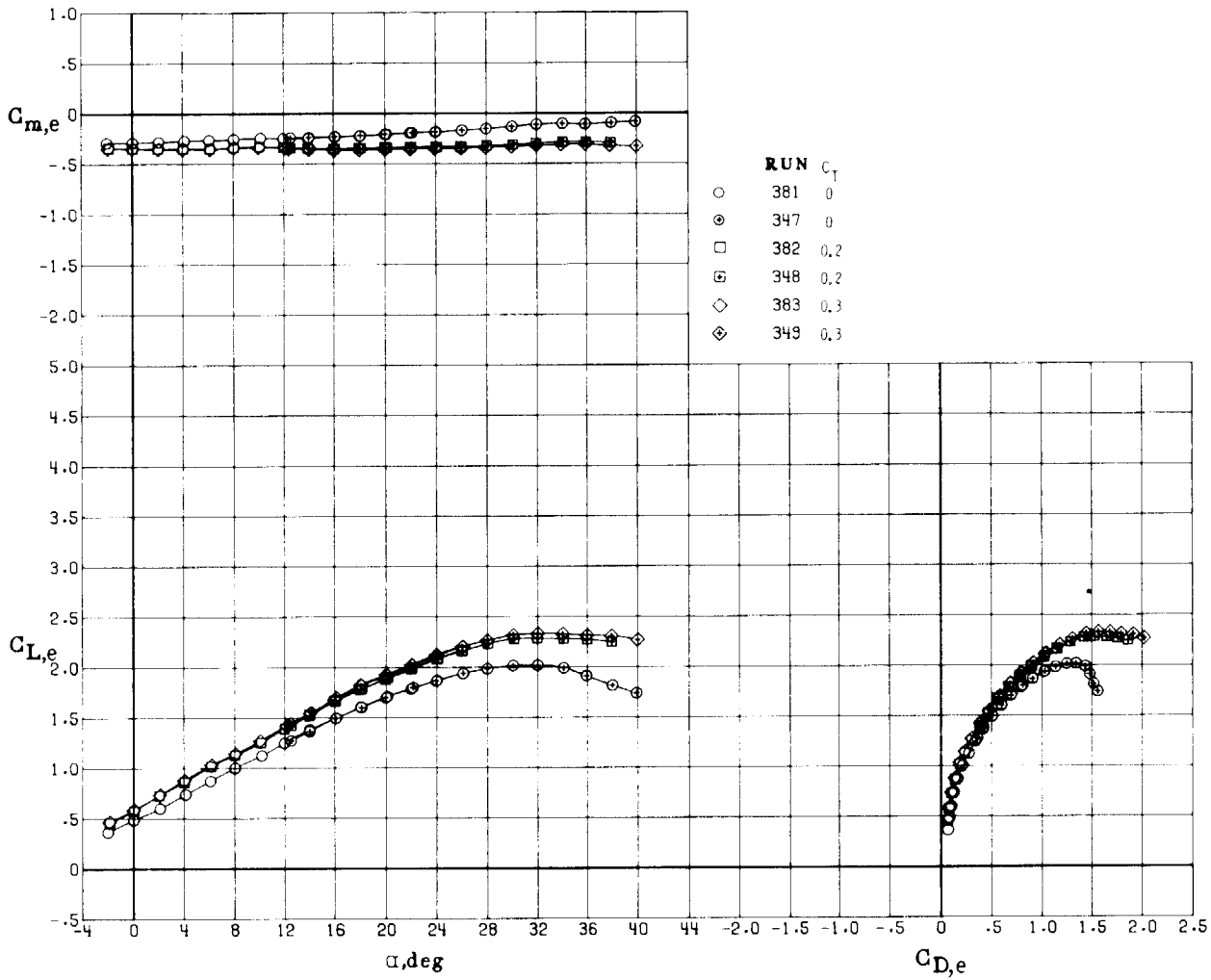

(b) $\delta_N = \delta_f = 30^o$.

Figure 9.- Concluded.

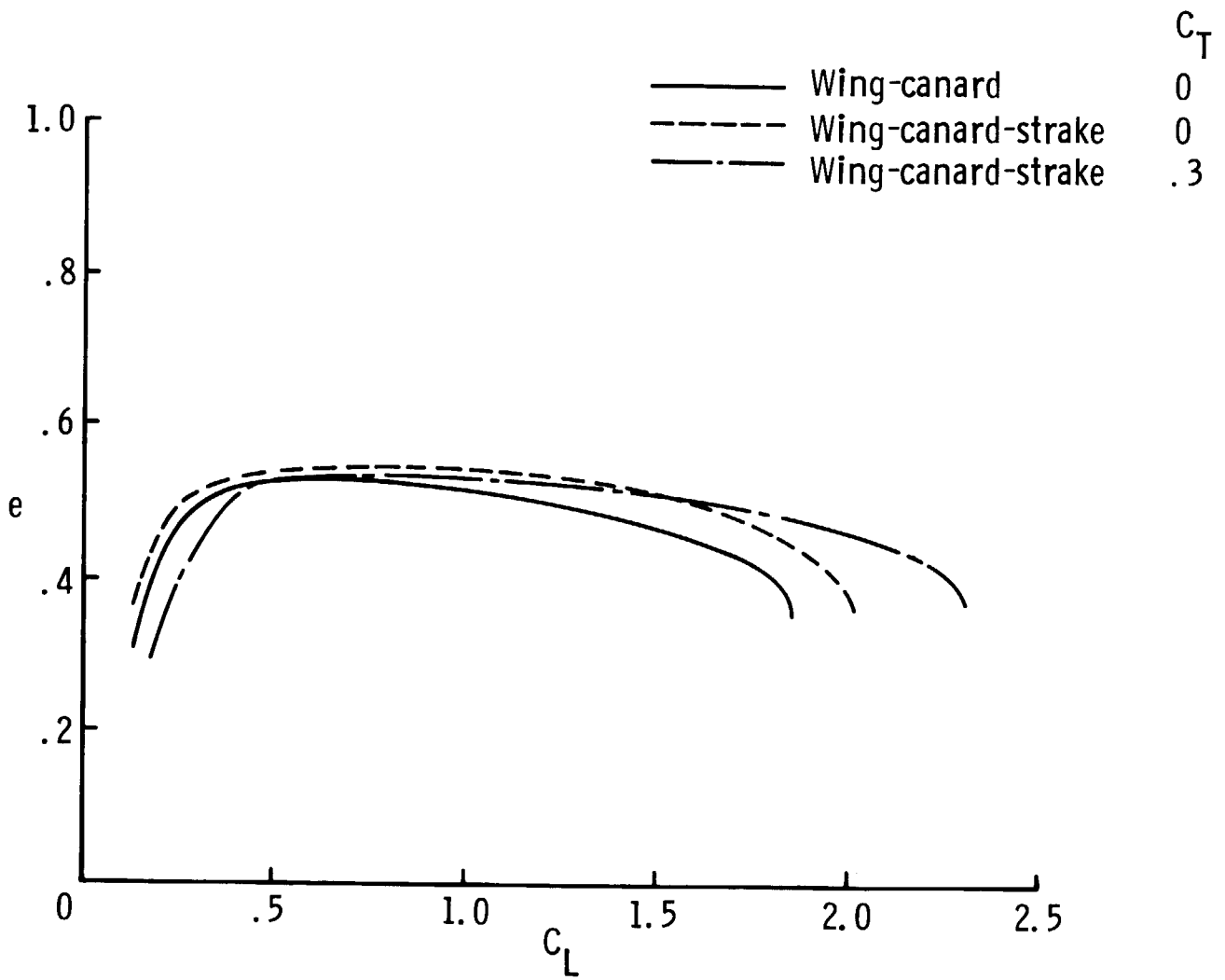

Figure 10.- Drag-due-to-lift efficiency factor for original wing-canard configuration.

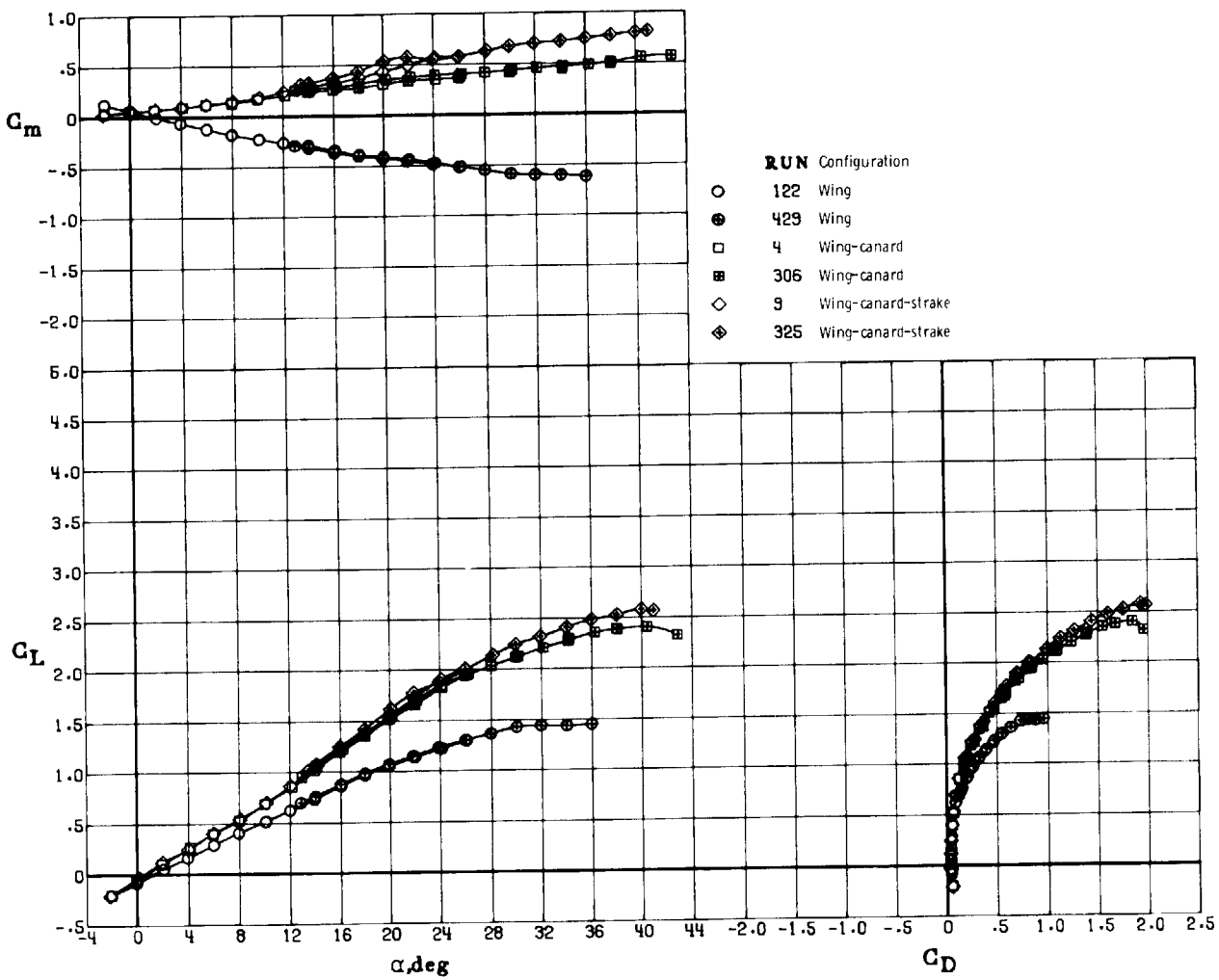

Figure 11.- Effect of adding canard and strake to new wing-alone configuration; $\delta_N = \delta_f = 0^\circ$ and $C_T = 0$.

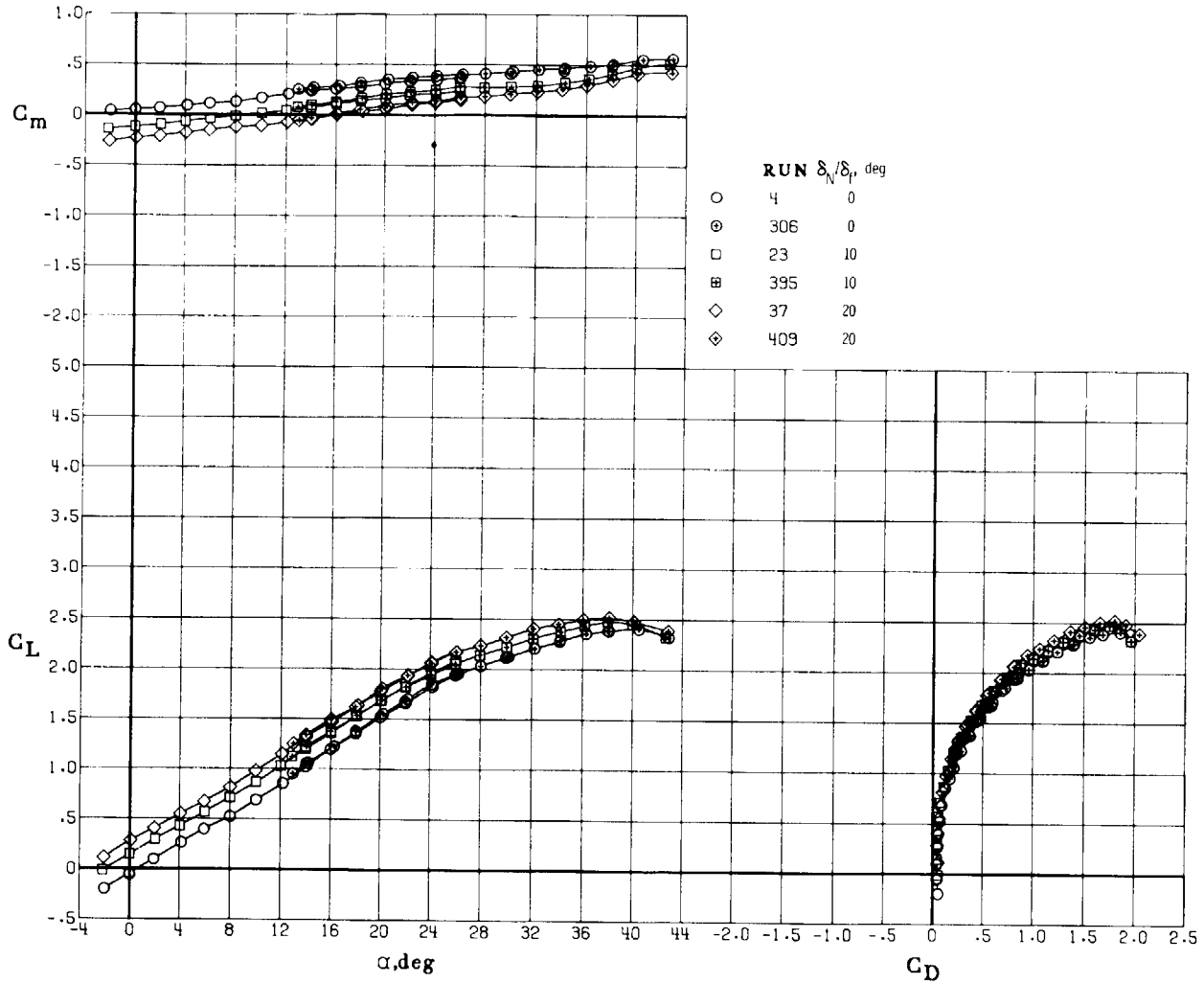

(a) $C_T = 0$; $\epsilon_w = -12^o$.

Figure 12.- Effect of nozzle/flap deflections on longitudinal aerodynamic characteristics of new wing-canard configuration at various thrust coefficients; $\delta_{le} = \delta_{le,c} = \delta_{f,c} = i_c = 0^o$.

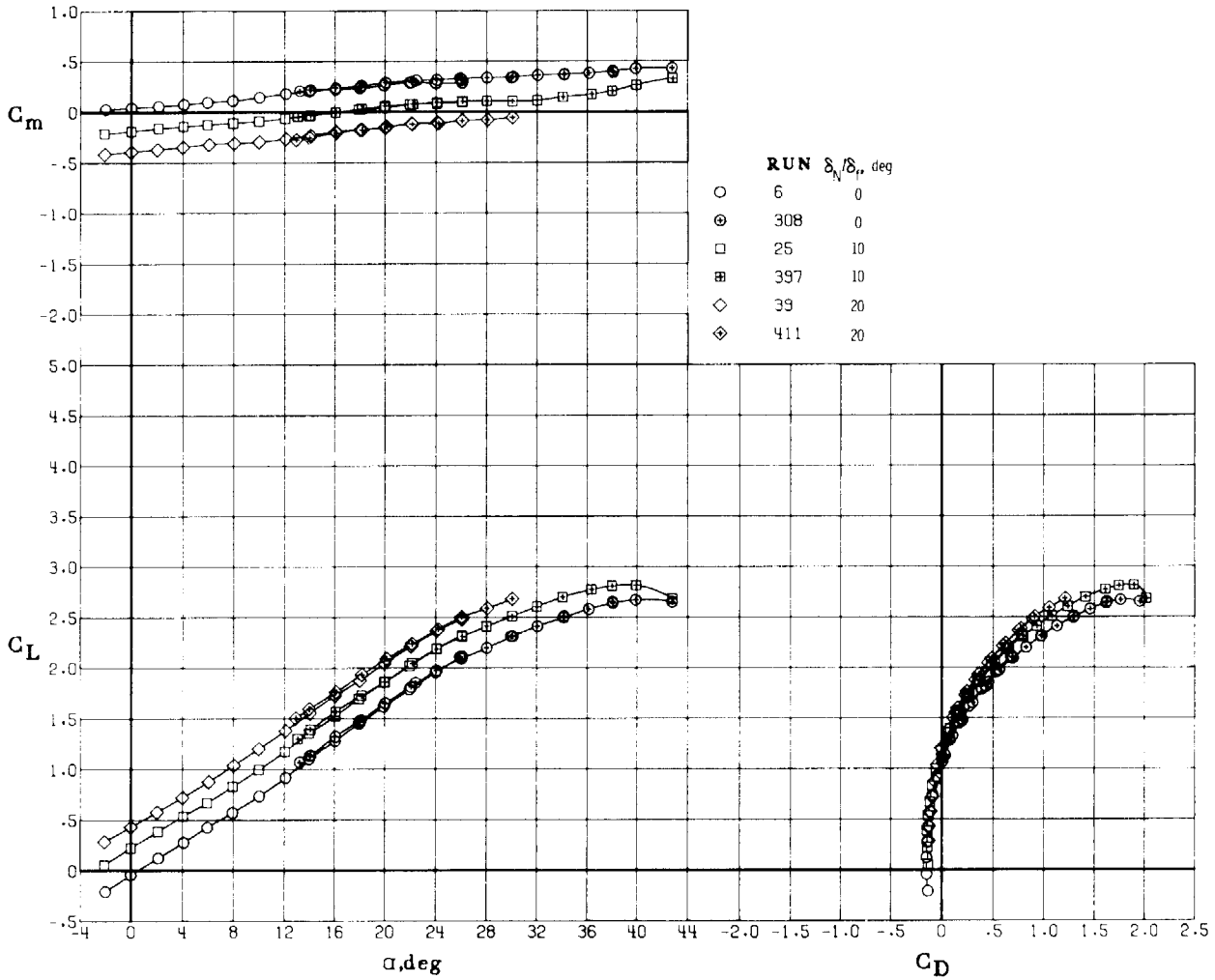

(b) $C_T = 0.2$; $\epsilon_w = -12^o$.

Figure 12.- Continued.

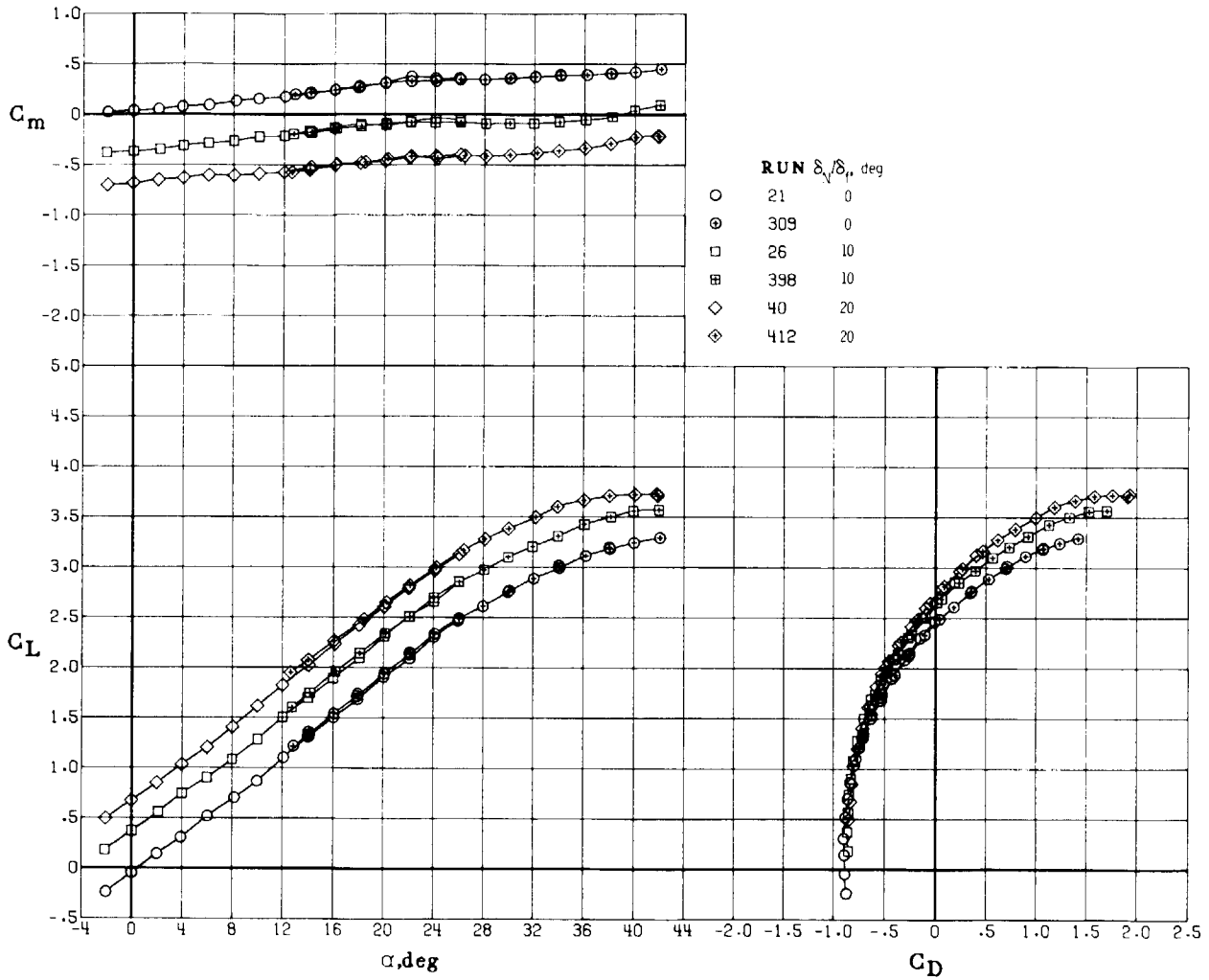

(c) $C_T = 1.0$; $\varepsilon_w = -12^o$.

Figure 12.- Continued.

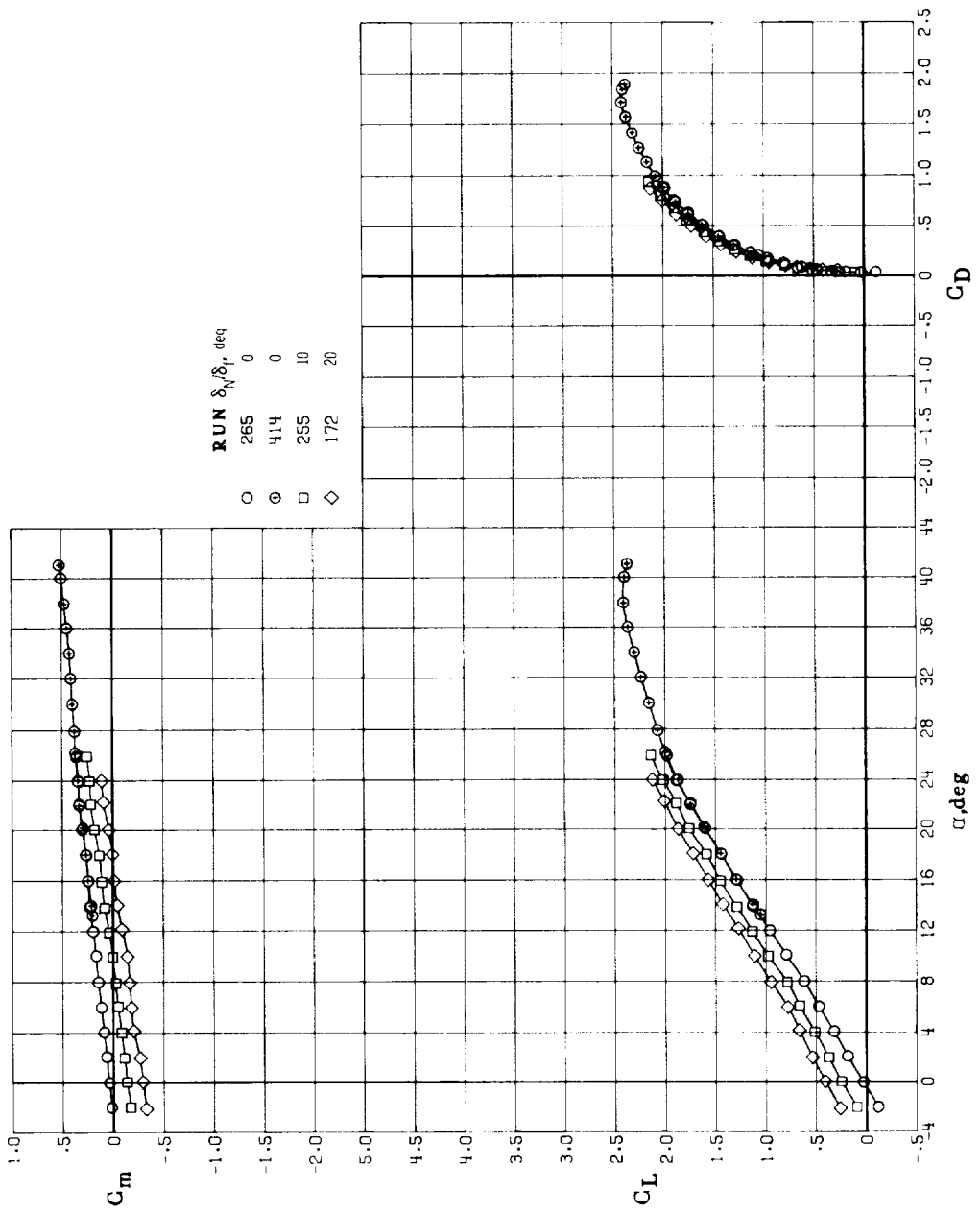

(d) $C_T = 0$; $\varepsilon_w = -6^o$.

Figure 12.- Continued.

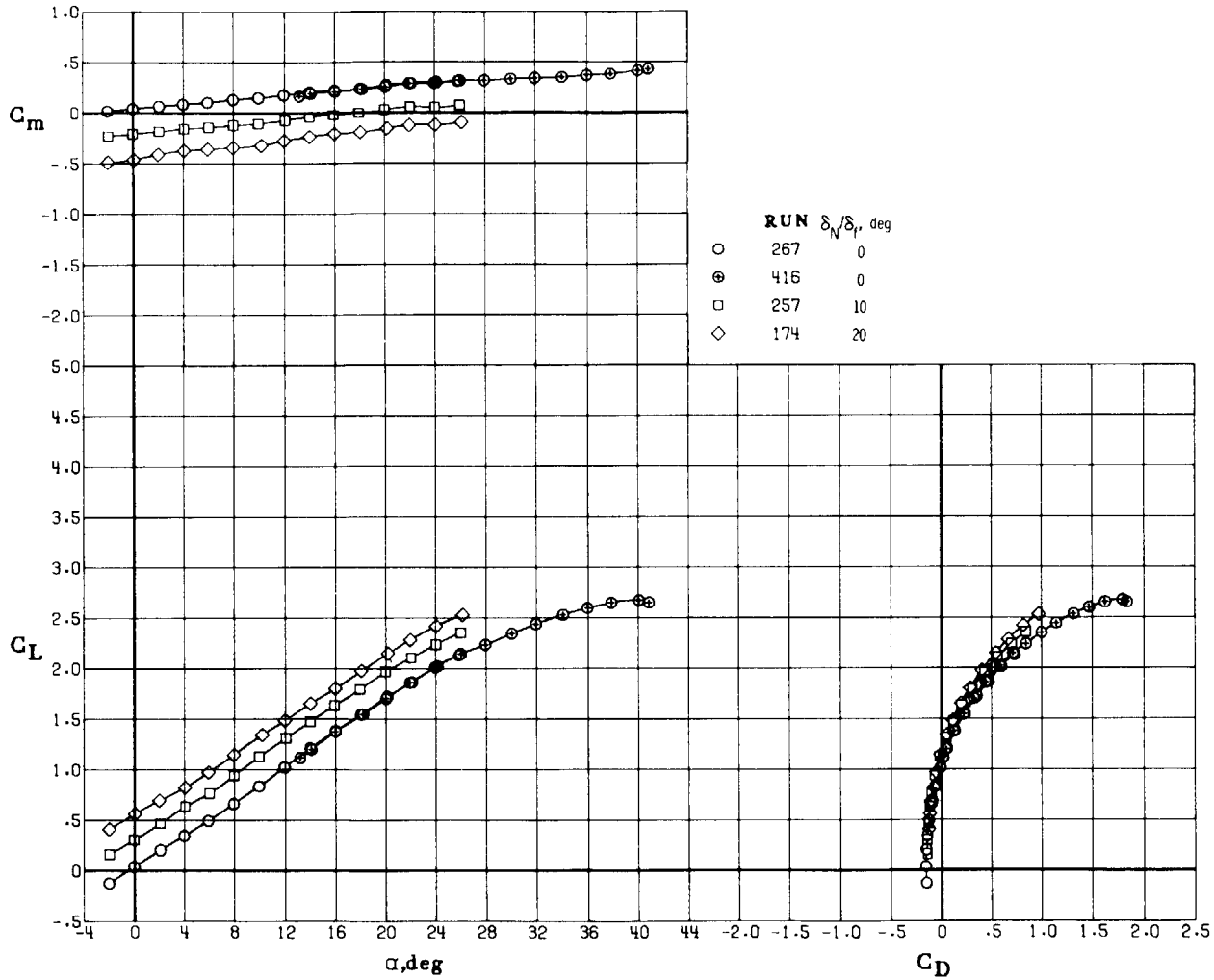

(e) $C_T = 0.2$; $\varepsilon_w = -6^o$.

Figure 12.- Continued.

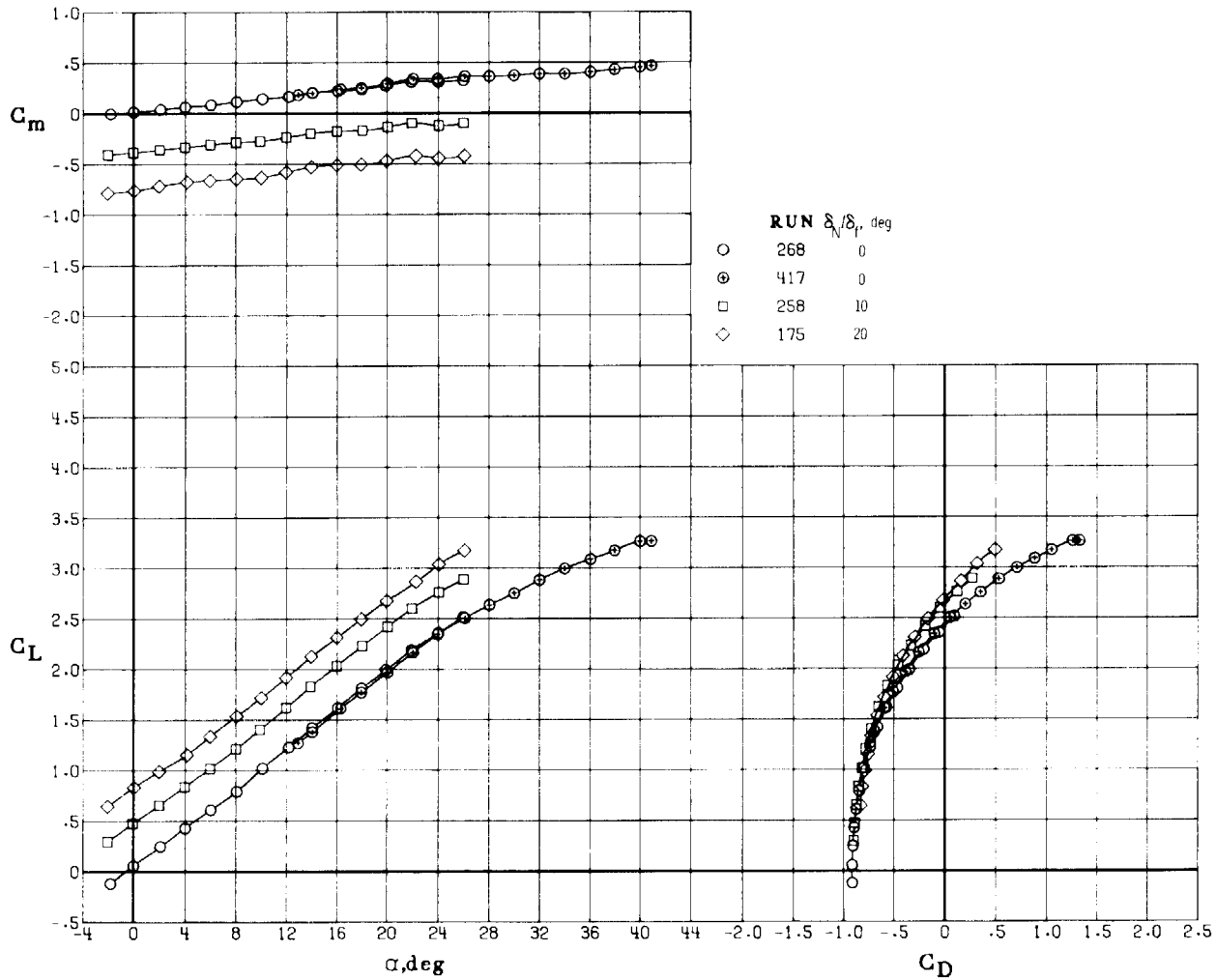

(f) $C_T = 1.0$; $\varepsilon_W = -6^o$.

Figure 12.- Concluded.

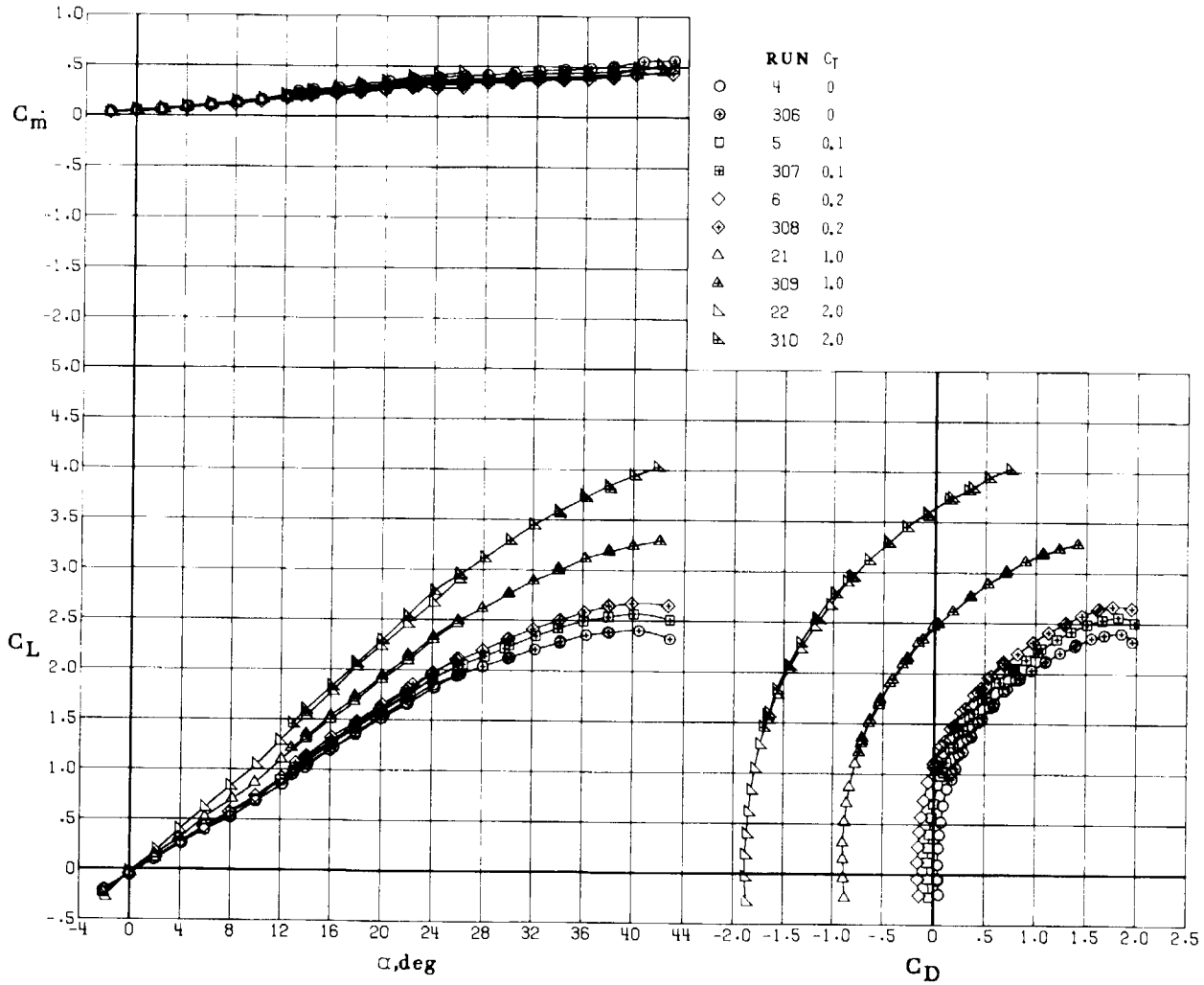

(a) $\delta_N = \delta_f = 0^o$; $\varepsilon_w = -12^o$.

Figure 13.- Effect of thrust coefficient on longitudinal aerodynamic characteristics of new wing canard configuration with various nozzle/flap deflections; $\delta_{le} = \delta_{le,c} = \delta_{f,c} = i_c = 0^o$.

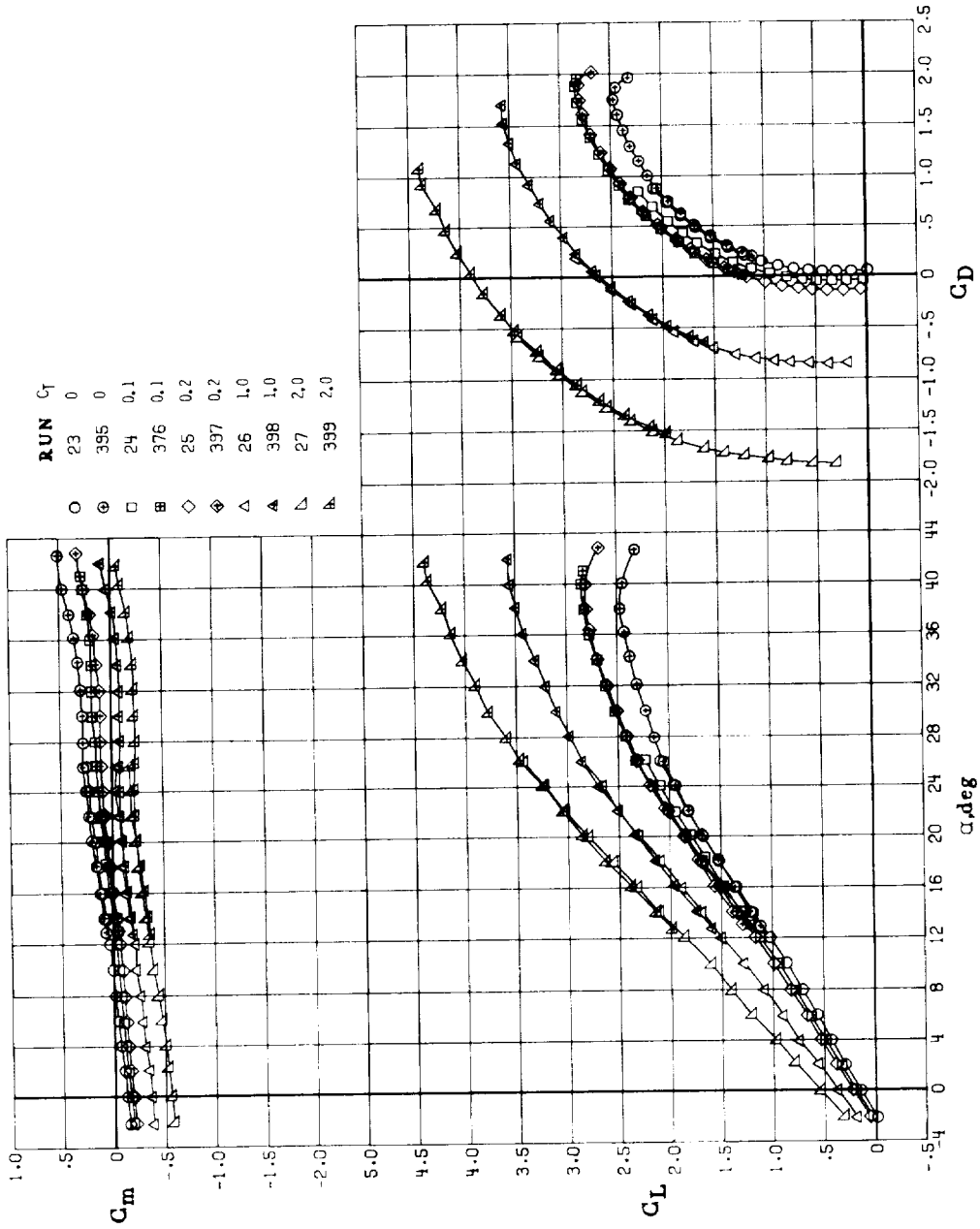

(b) $\delta_N = \delta_f = 10^o$; $\varepsilon_w = -12^o$.

Figure 13.- Continued.

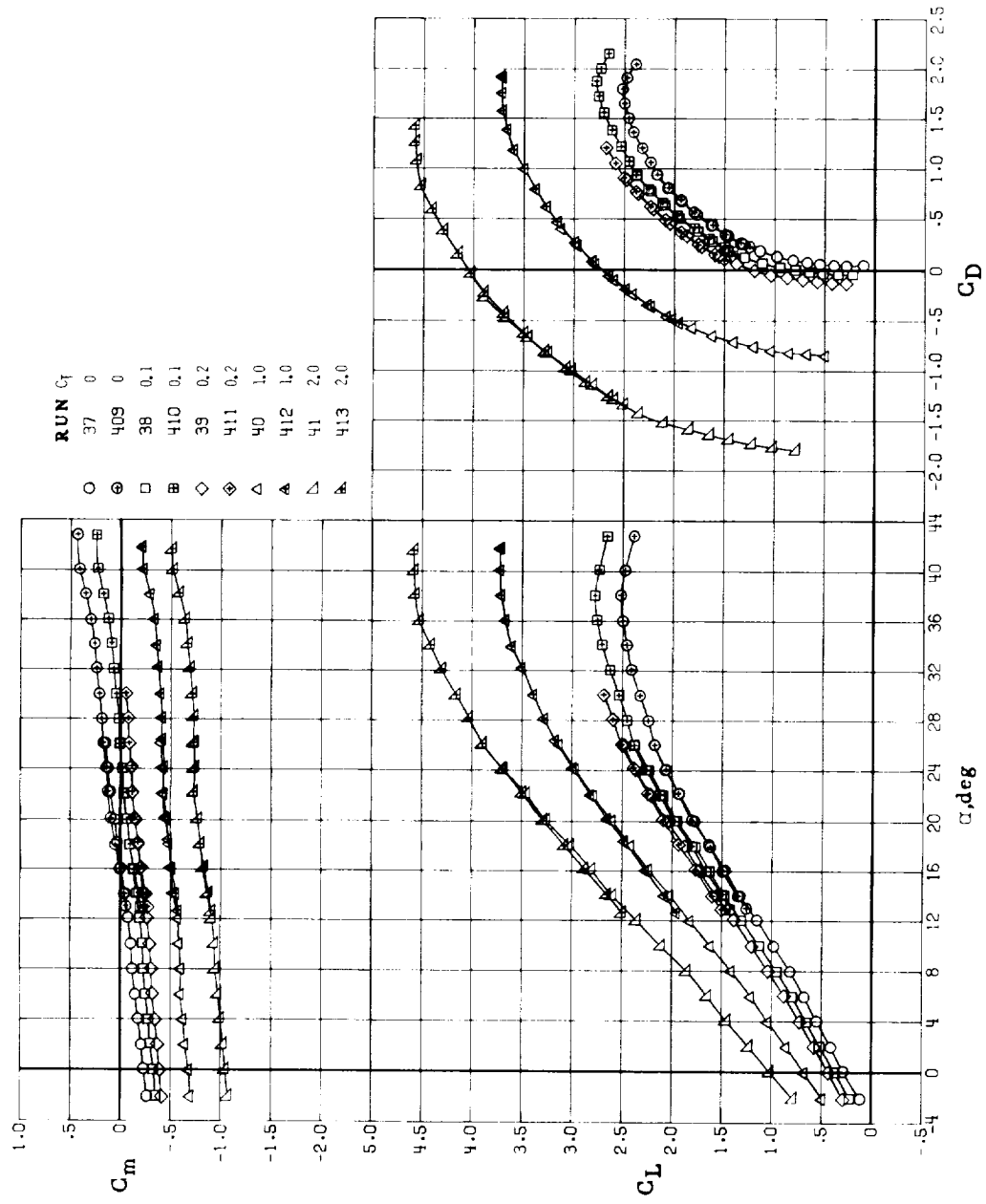

(c) $\delta_N = \delta_f = 20°$; $\varepsilon_w = -12°$.

Figure 13.- Continued.

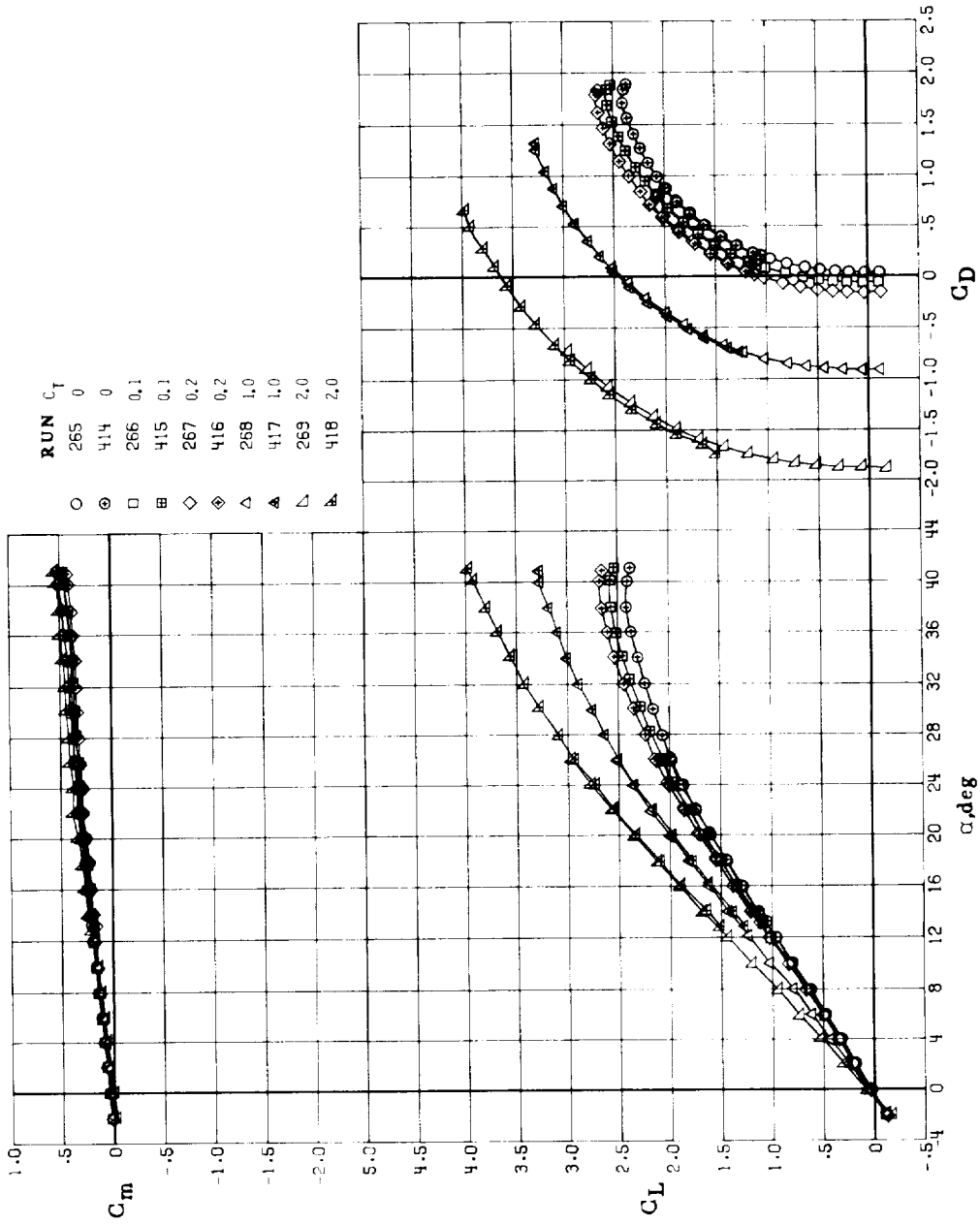

(d) $\delta_N = \delta_f = 0°$; $\epsilon_w = -6°$.

Figure 13.- Continued.

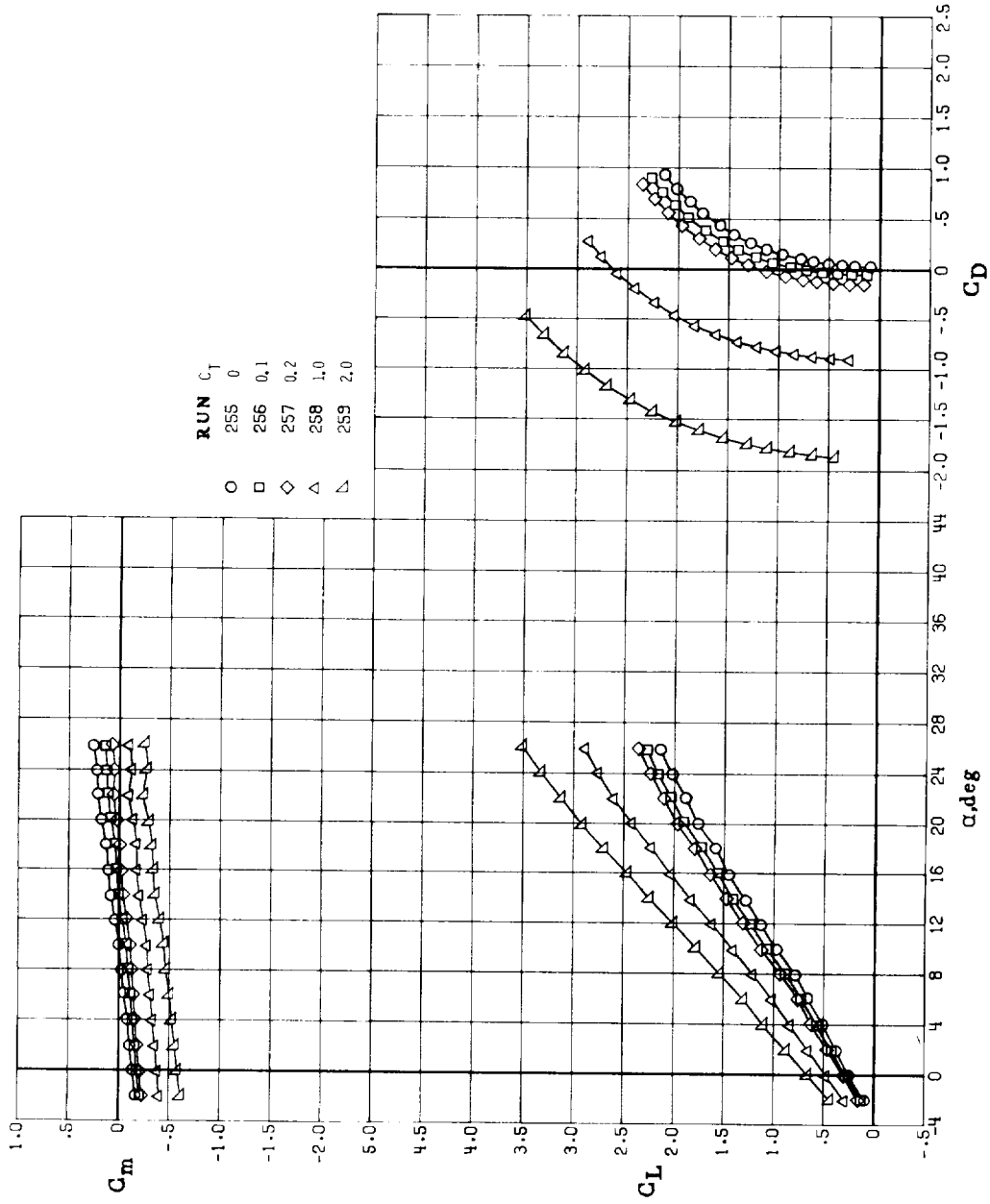

(e) $\delta_N = \delta_f = 10°$; $\varepsilon_w = -6°$.

Figure 13.- Continued.

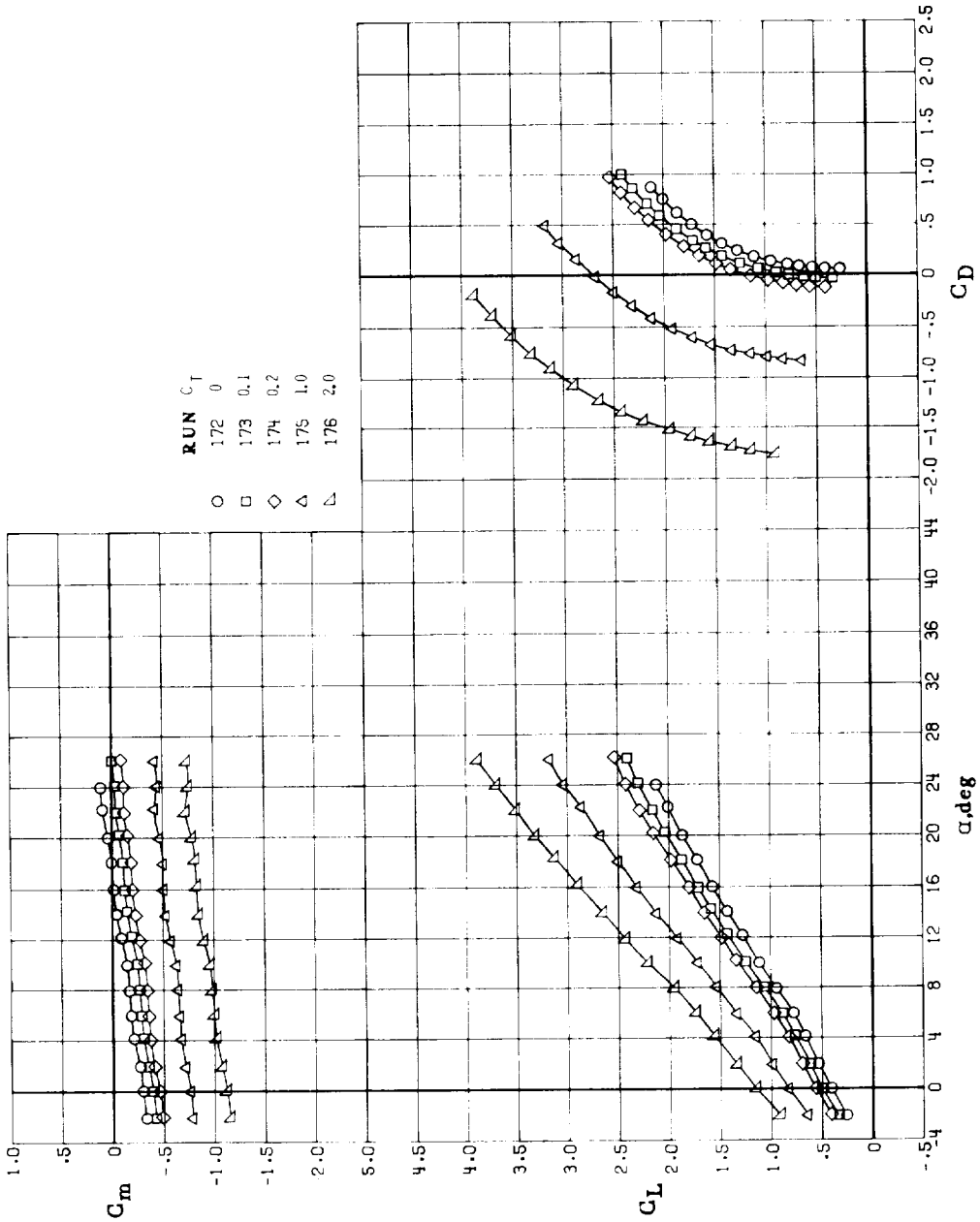

(f) $\delta_N = \delta_f = 20^o$; $\varepsilon_w = -6^o$.

Figure 13.- Continued.

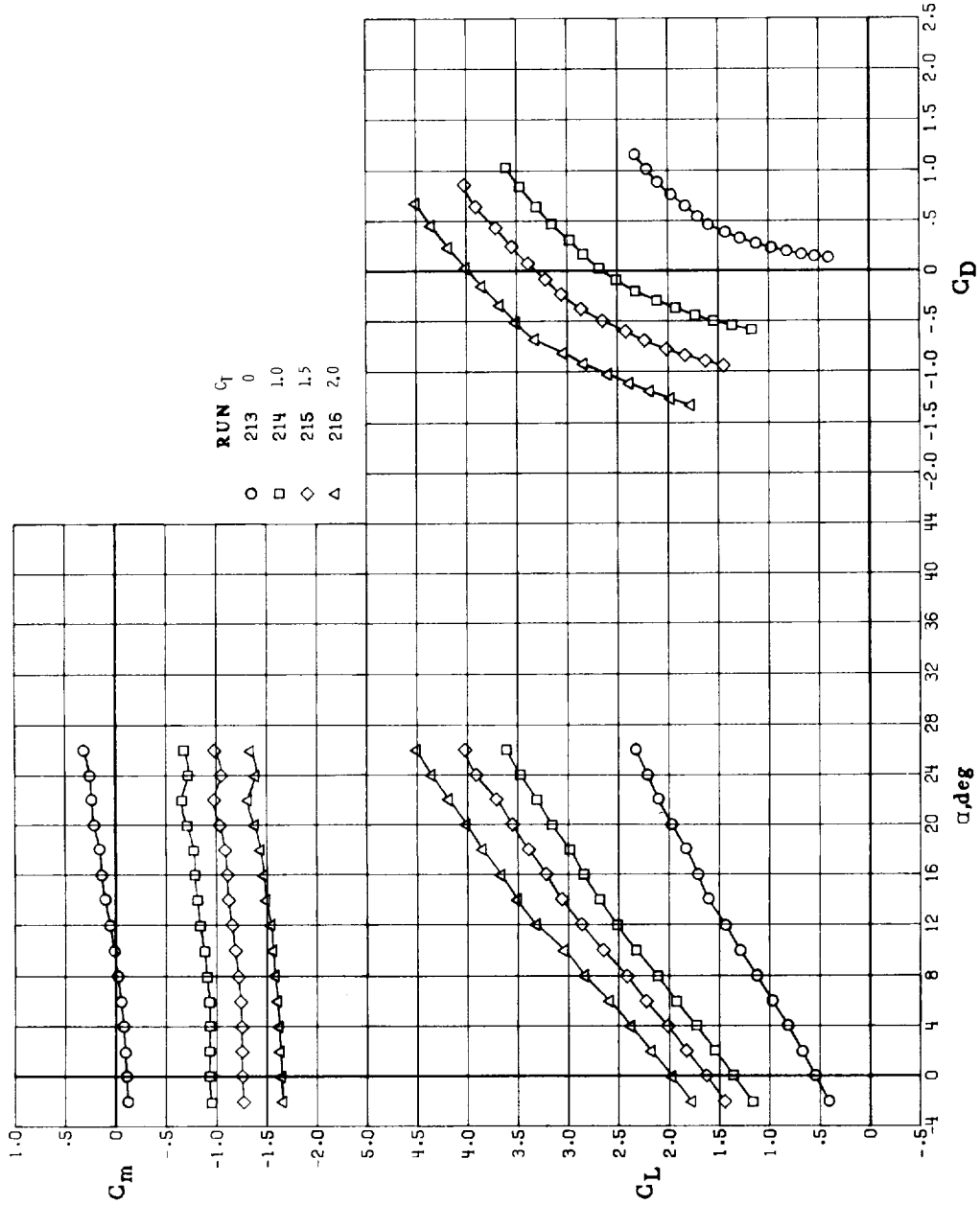

(g) $\delta_N = \delta_f = 40°$; $\varepsilon_w = -6°$.

Figure 13.- Concluded.

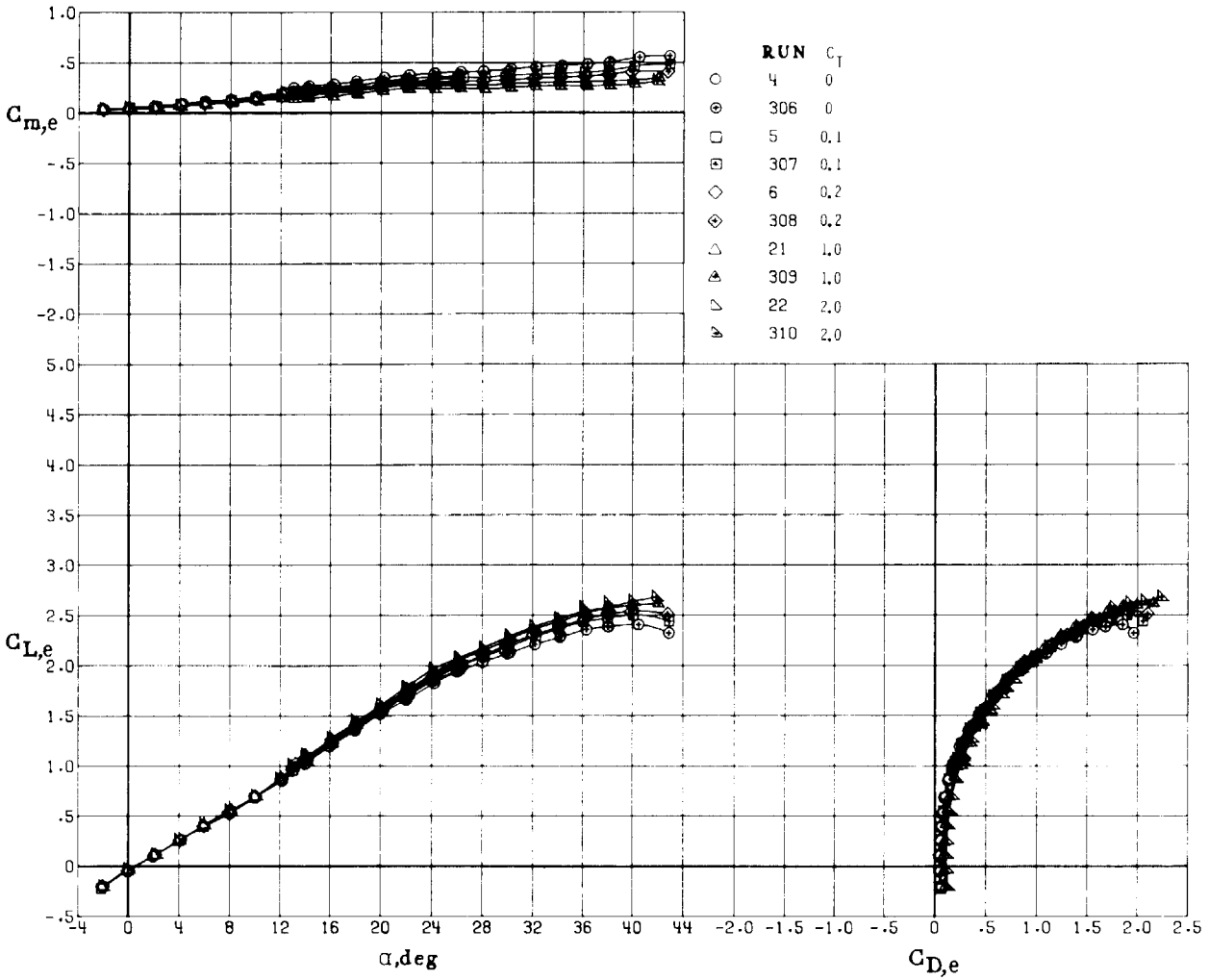

(a) $\delta_N = \delta_f = 0^o$.

Figure 14.- Effect of thrust coefficient on thrust-removed longitudinal aerodynamic characteristics of new wing-canard configuration at various nozzle/flap deflections; $\varepsilon_w = -12^o$.

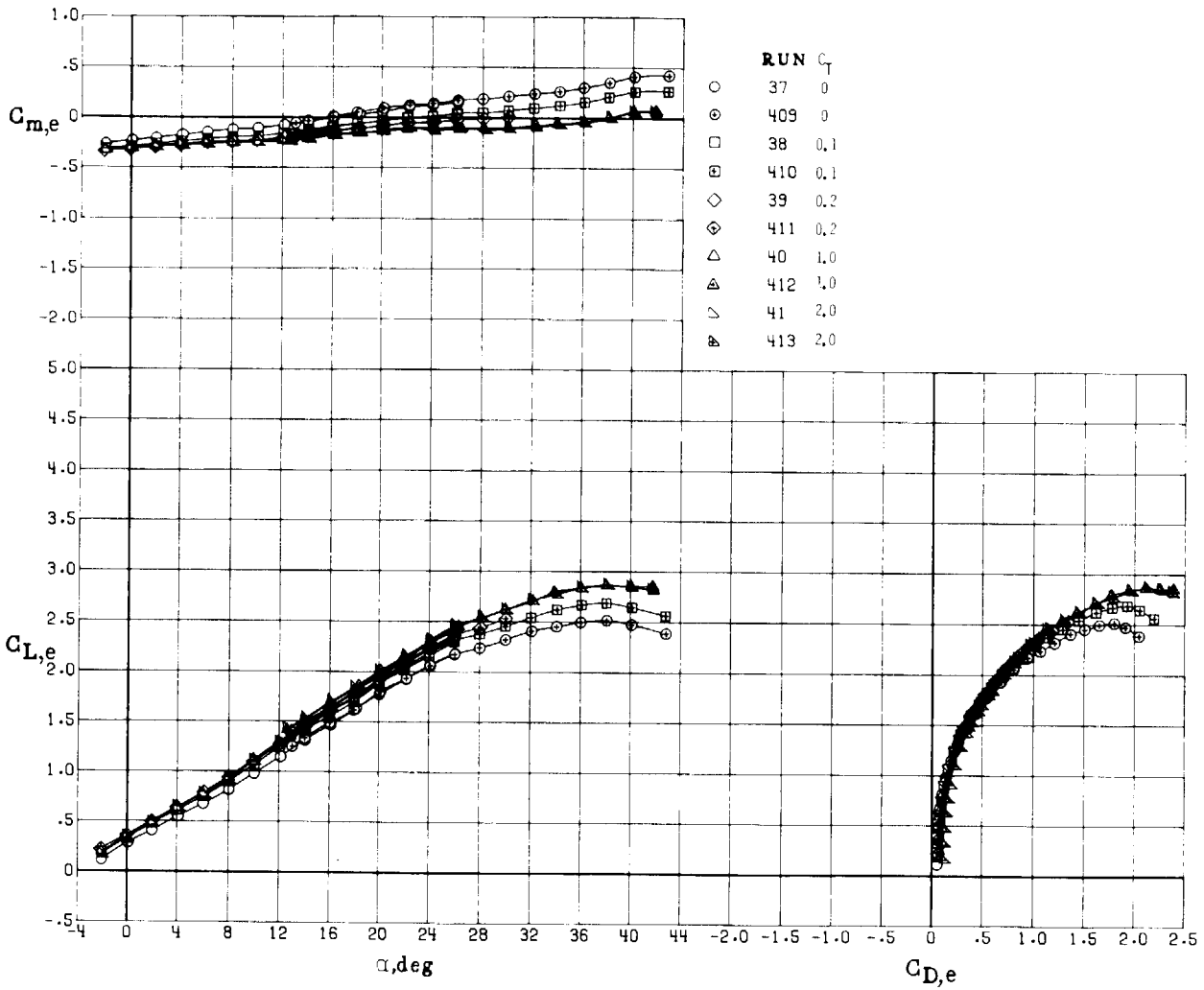

(b) $\delta_N = \delta_f = 20^o$.

Figure 14.- Concluded.

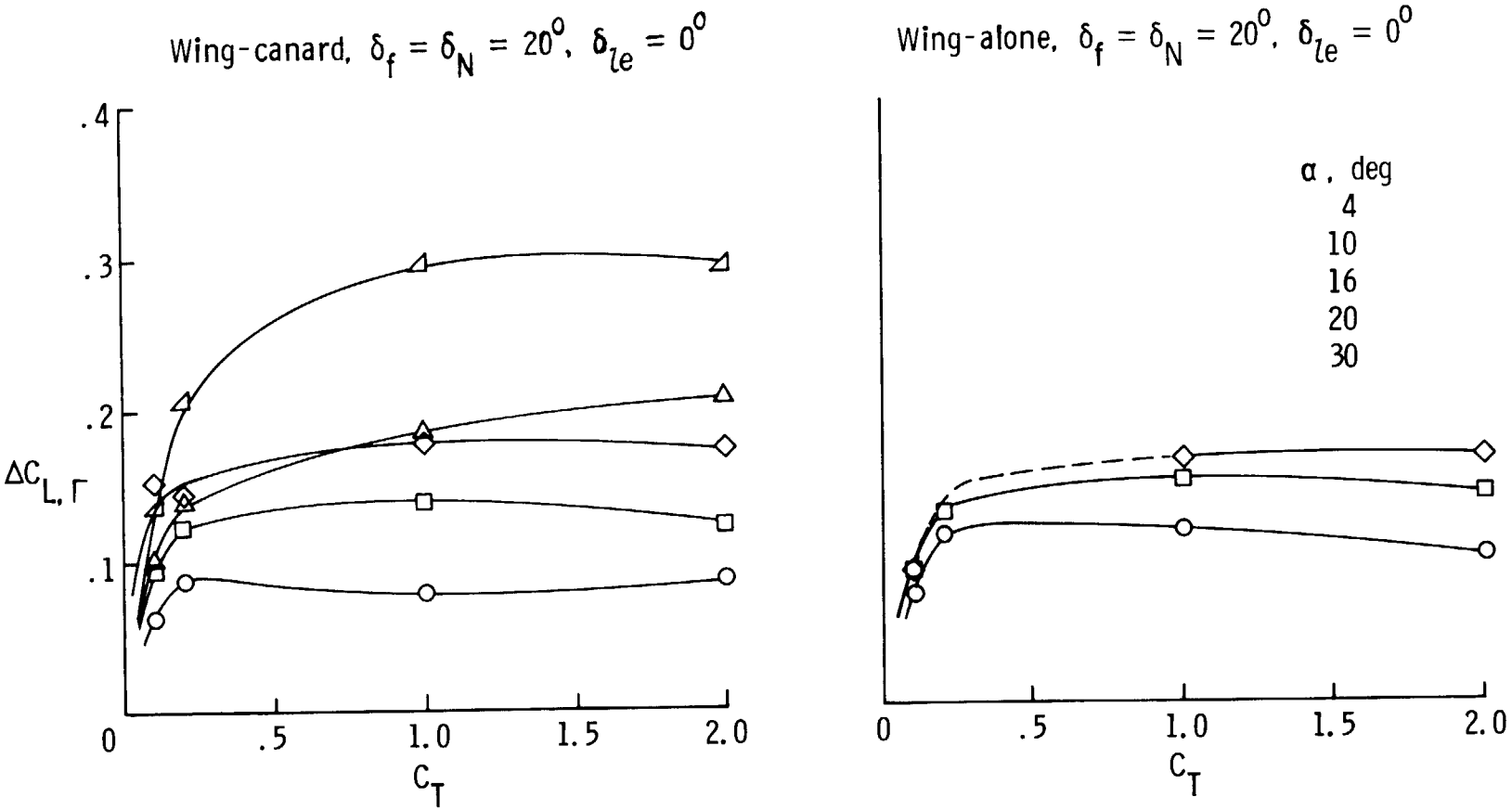

Figure 15.- Thrust induced lift increments for new wing-canard configuration; $\epsilon_w = -12^o$.

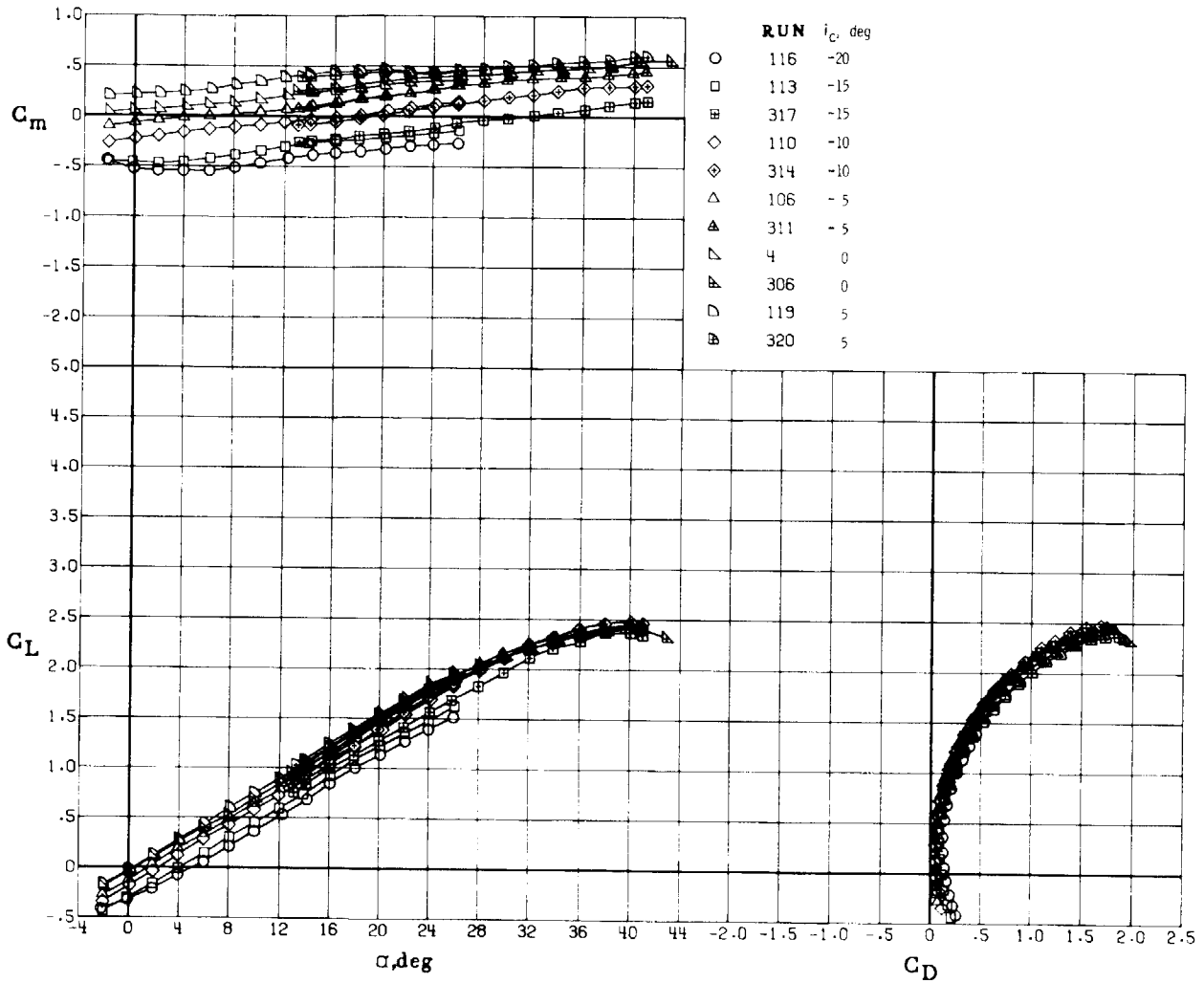

(a) $C_T = 0$; $\delta_N = \delta_f = \delta_{le} = 0^o$; $\varepsilon_w = -12^o$.

Figure 16.- Effect of canard incidence on longitudinal aerodynamic characteristics of new wing-canard configuration at various thrust coefficients and nozzle/flap and leading-edge deflections; $\delta_{f,c} = \delta_{le,c} = 0^o$.

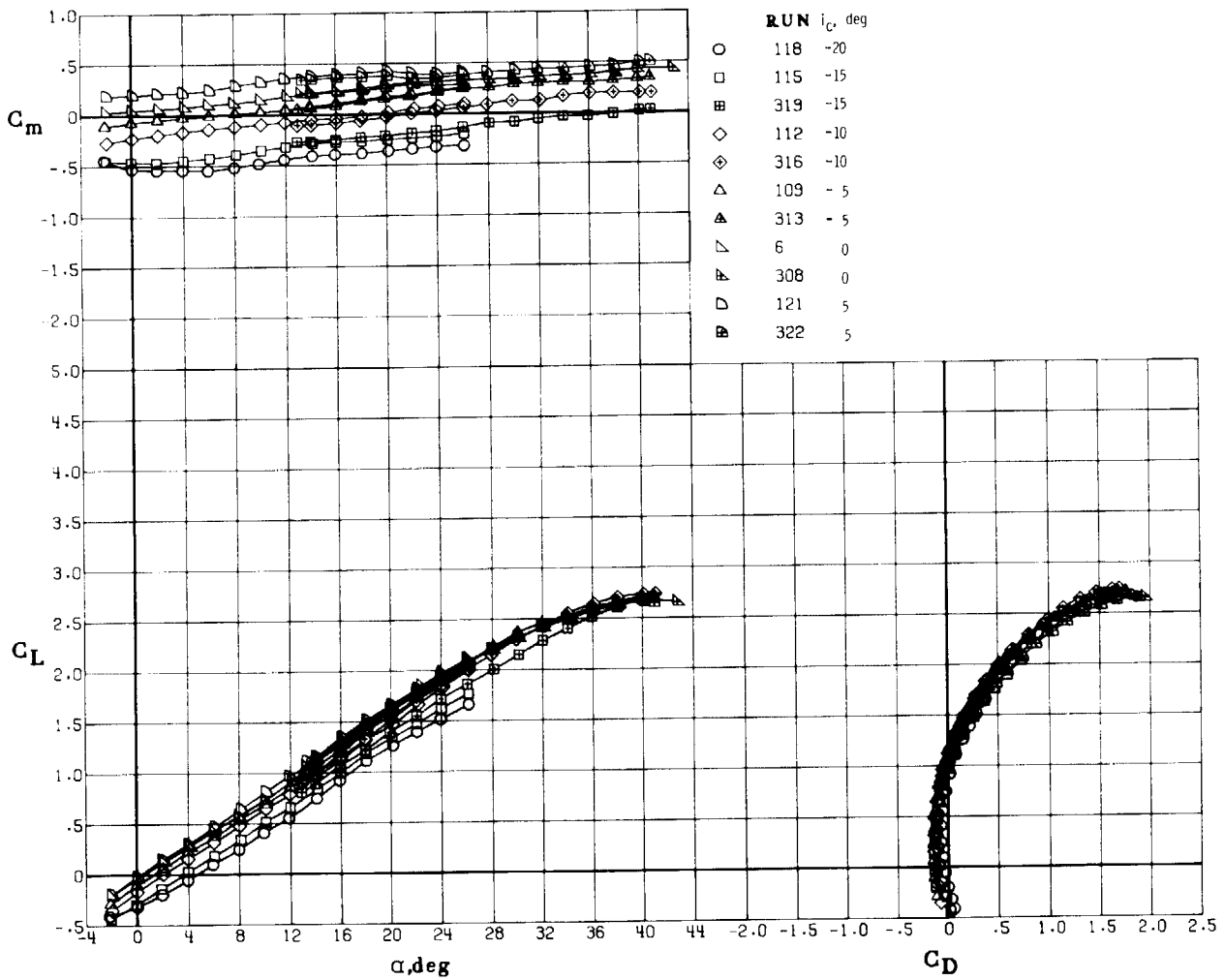

(b) $C_T = 0.2$; $\delta_N = \delta_f = \delta_{le} = 0^o$; $\epsilon_w = -12^o$.

Figure 16.- Continued.

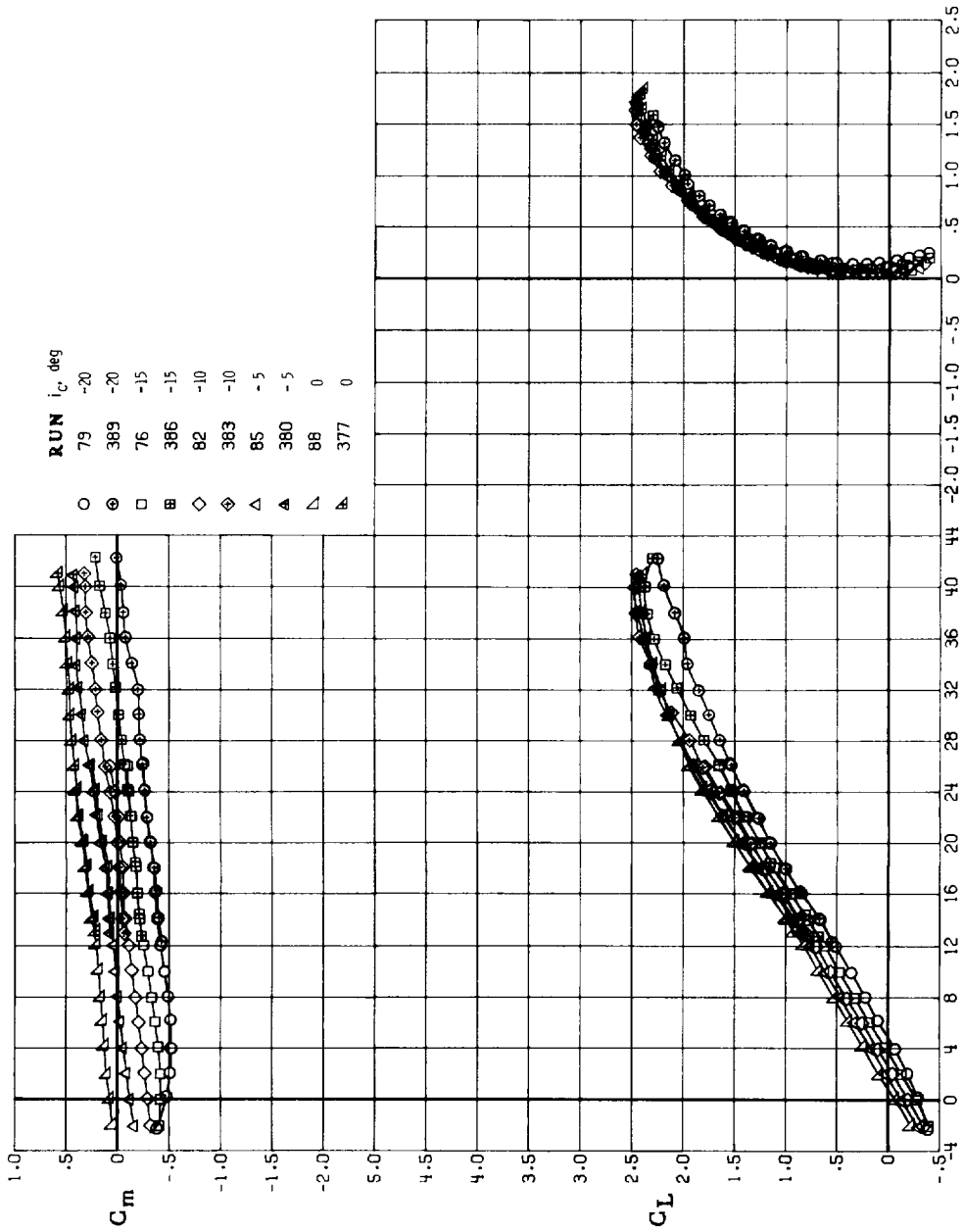

(c) $C_T = 0$; $\delta_N = \delta_f = 0°$; $\delta_{le} = 20°$; $\varepsilon_W = -12°$.

Figure 16.- Continued.

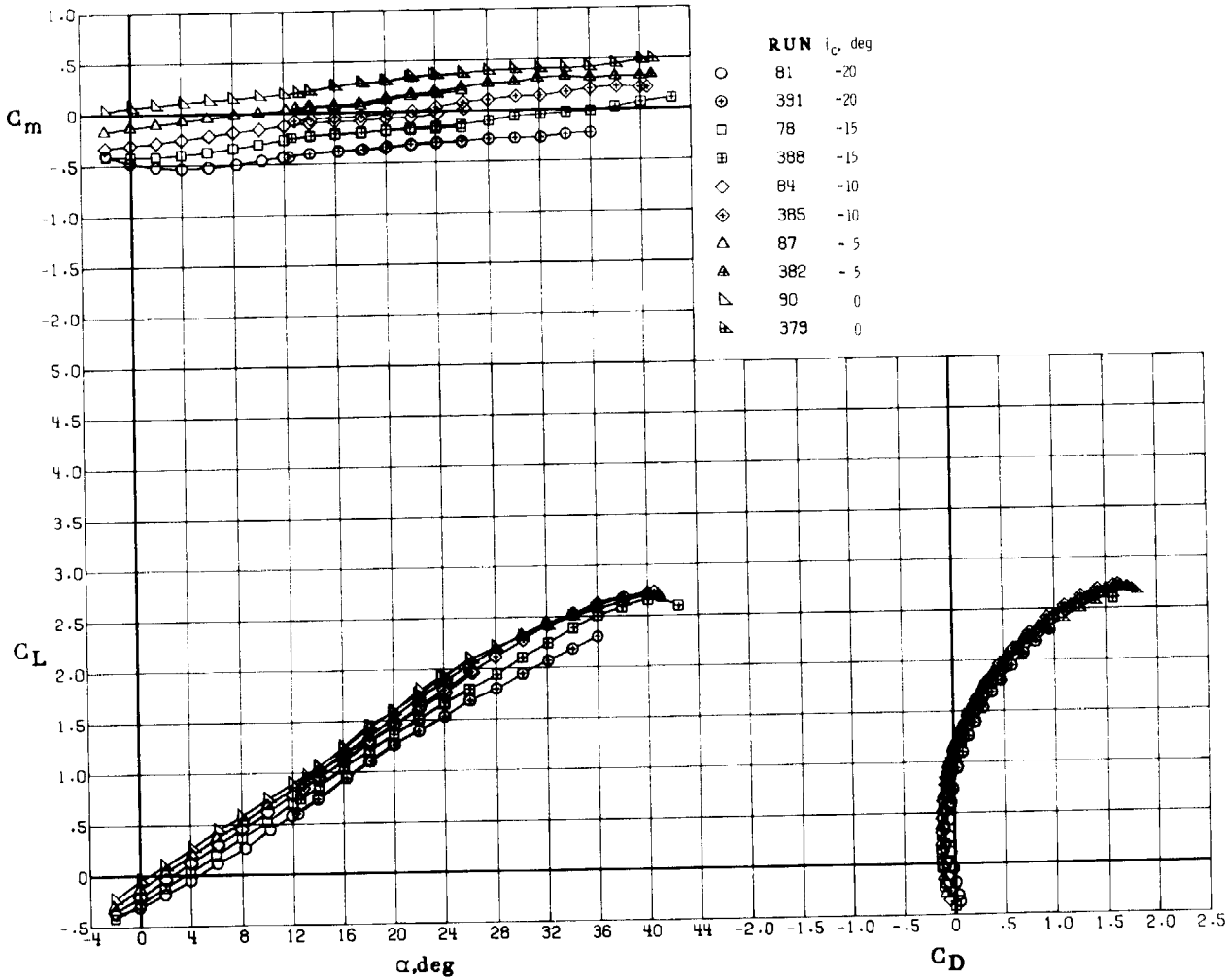

(d) $C_T = 0.2$; $\delta_N = \delta_f = 0^o$; $\delta_{le} = 20^o$; $\varepsilon_w = -12^o$.

Figure 16.- Continued.

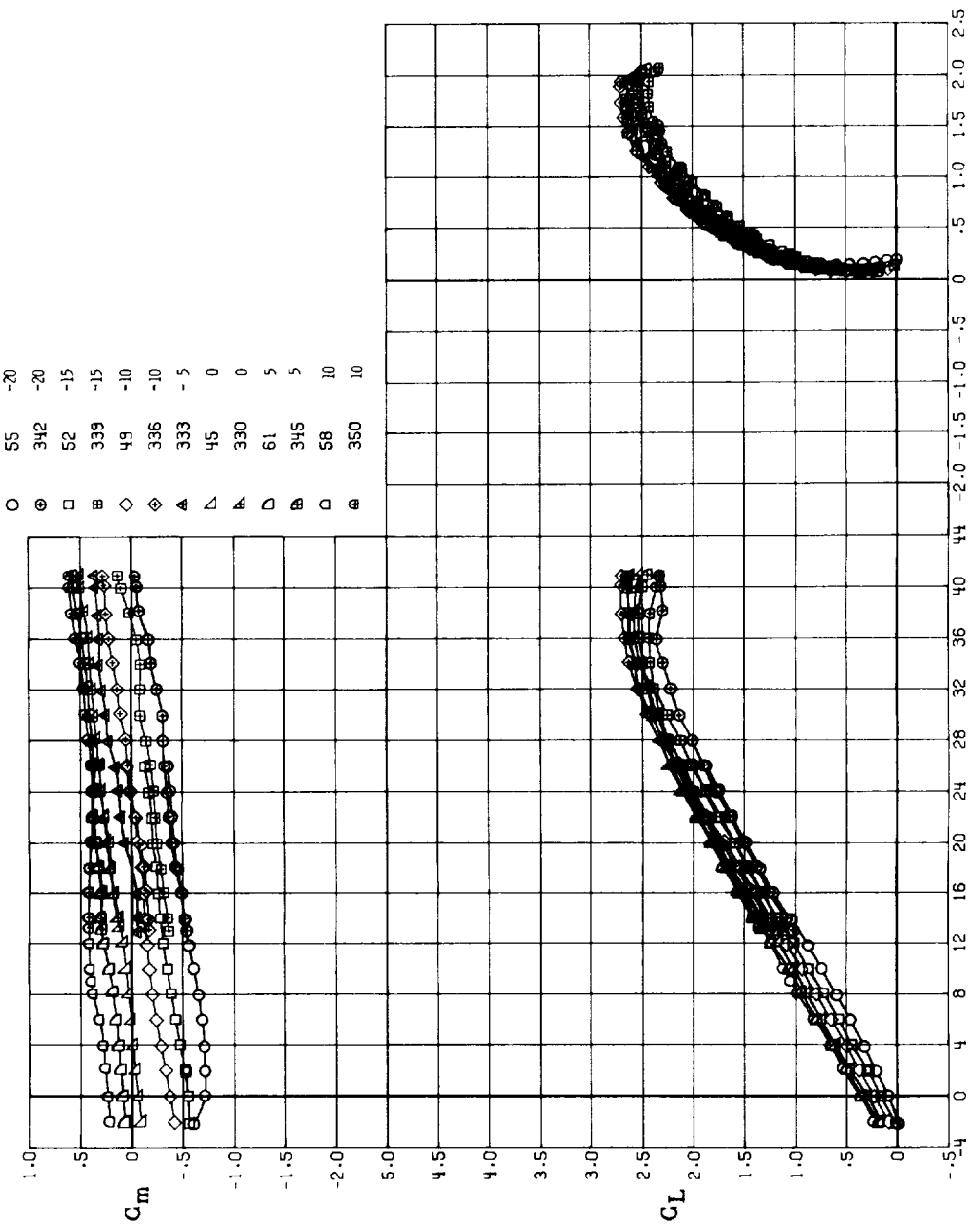

(e) $C_T = 0$; $\delta_N = \delta_f = 20°$; $\delta_{le} = 20°$; $\epsilon_w = -12°$.

Figure 16.- Continued.

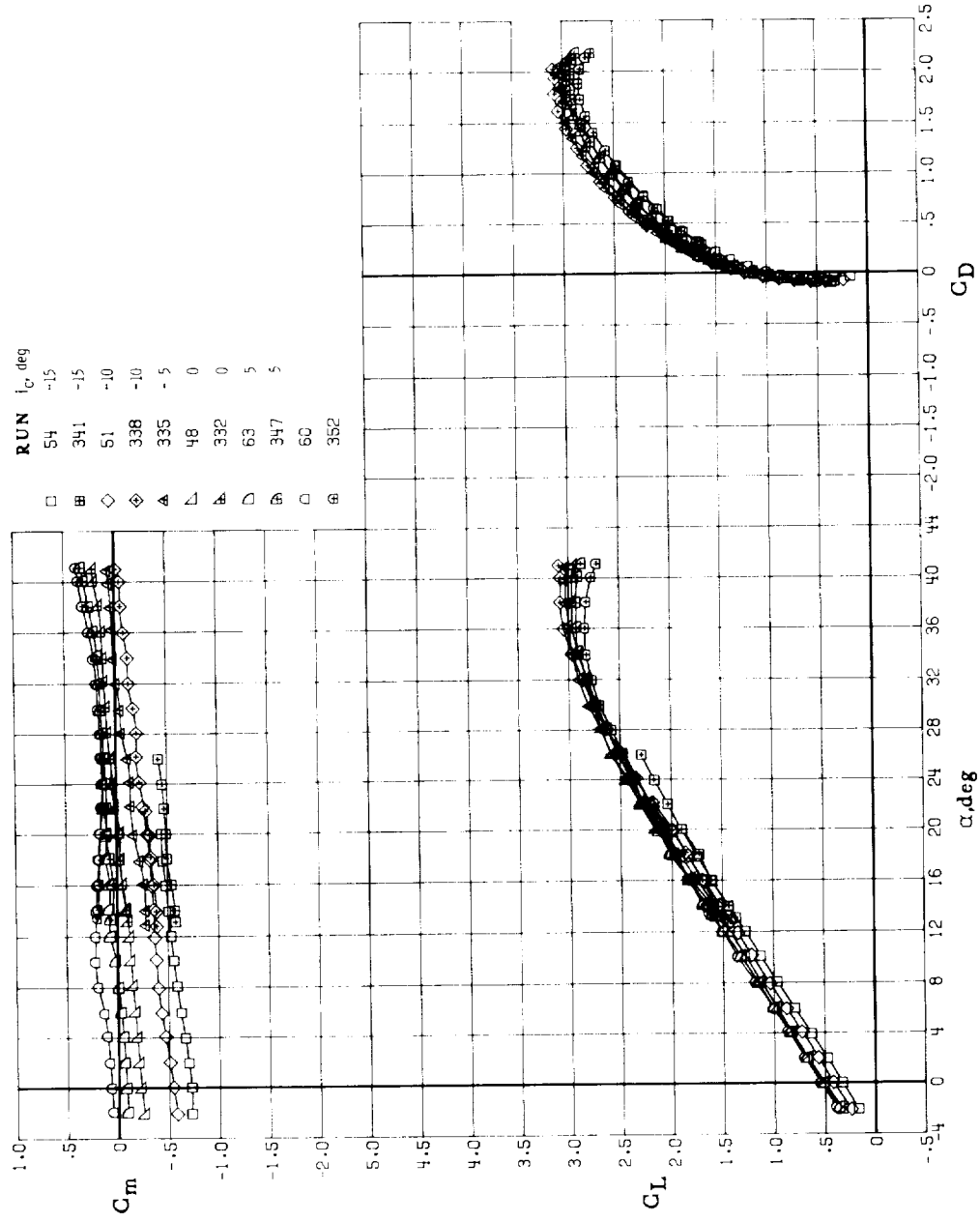

(f) $C_T = 0.2$; $\delta_N = \delta_f = 20°$; $\delta_{le} = 20°$; $\varepsilon_w = -12°$.

Figure 16.- Continued.

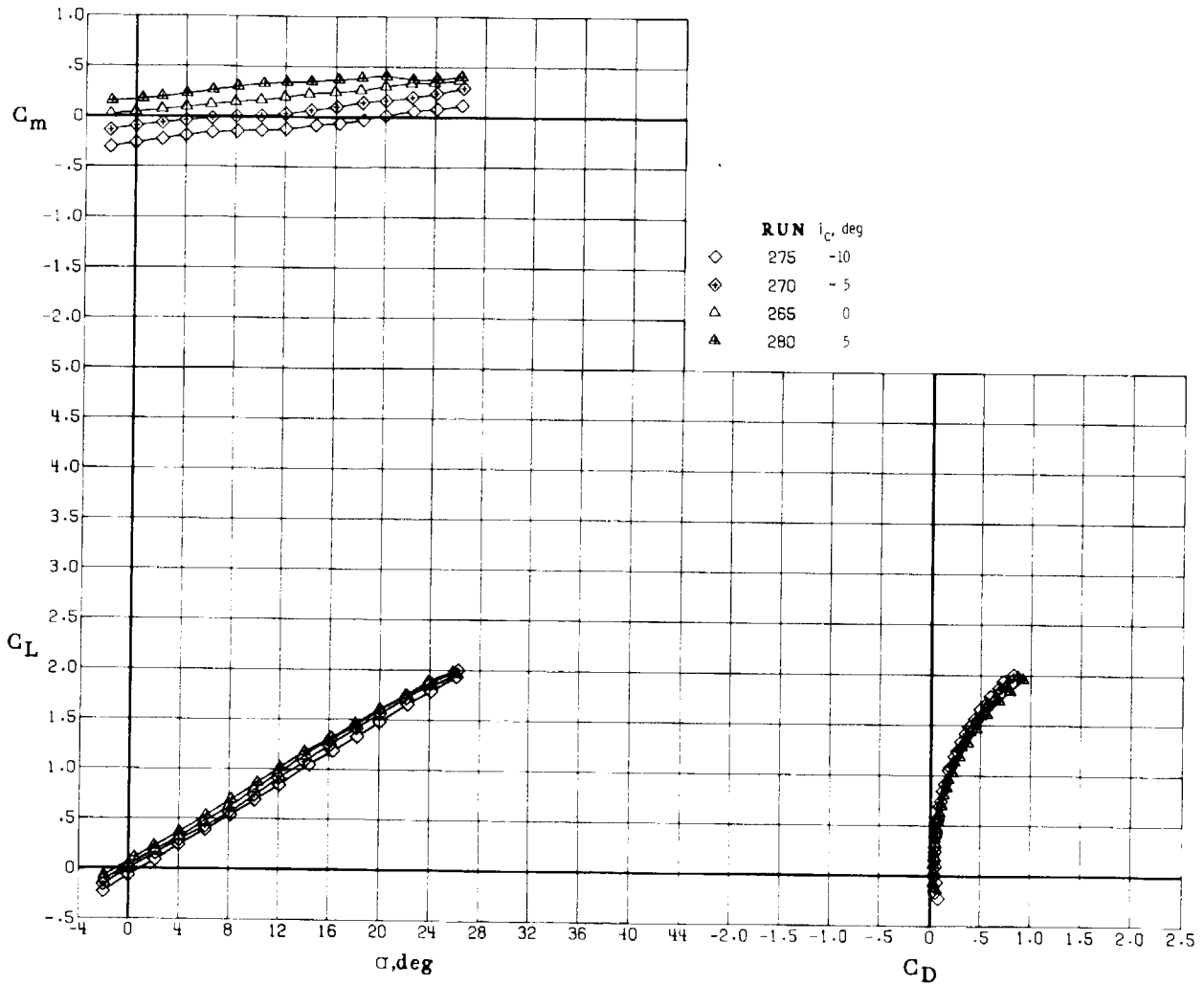

(g) $C_T = 0$; $\delta_N = \delta_f = \delta_{le} = 0^o$; $\varepsilon_w = -6^o$.

Figure 16.- Continued.

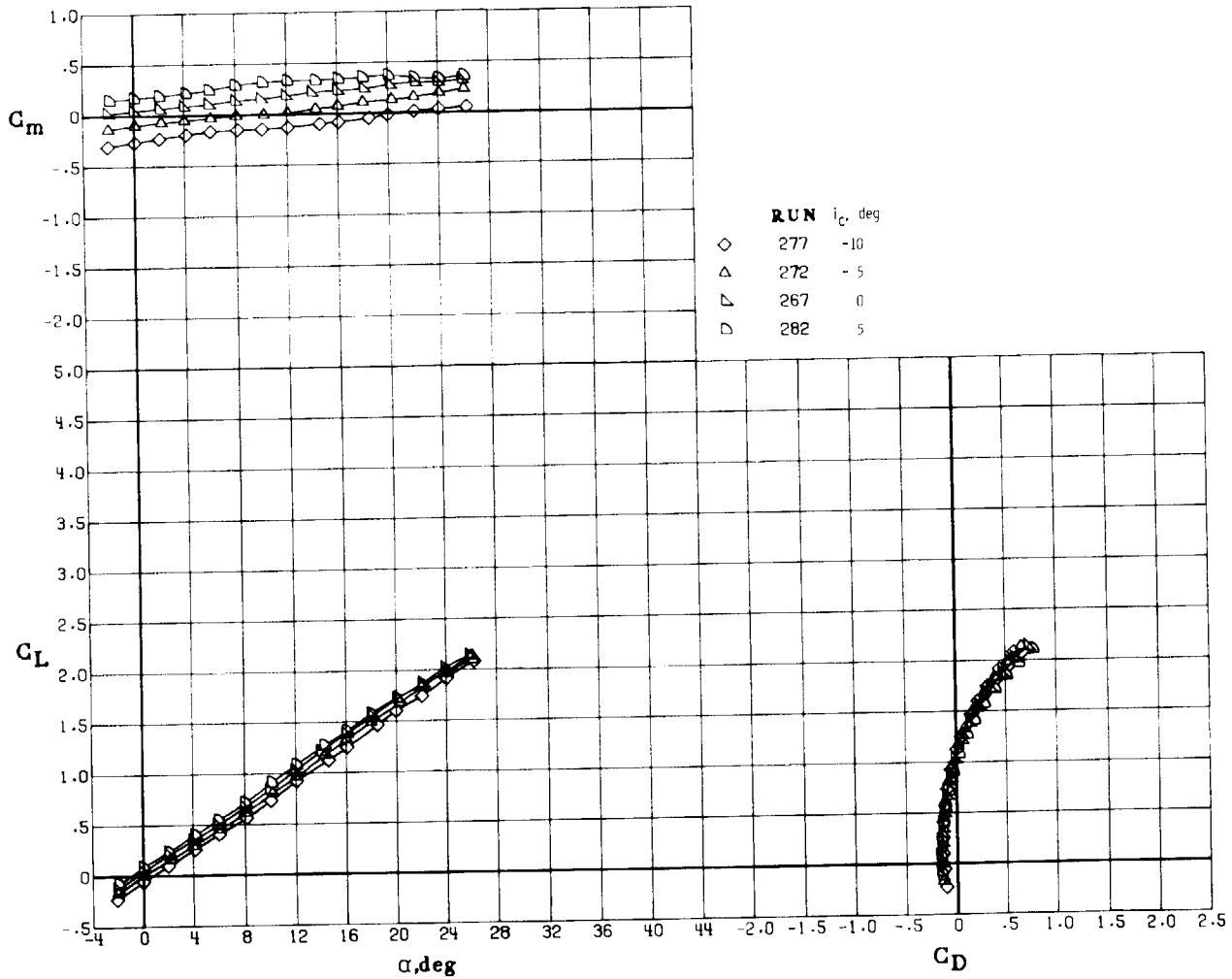

(h) $C_T = 0.2$; $\delta_N = \delta_f = \delta_{le} = 0^o$; $\varepsilon_w = -6^o$.

Figure 16.- Continued.

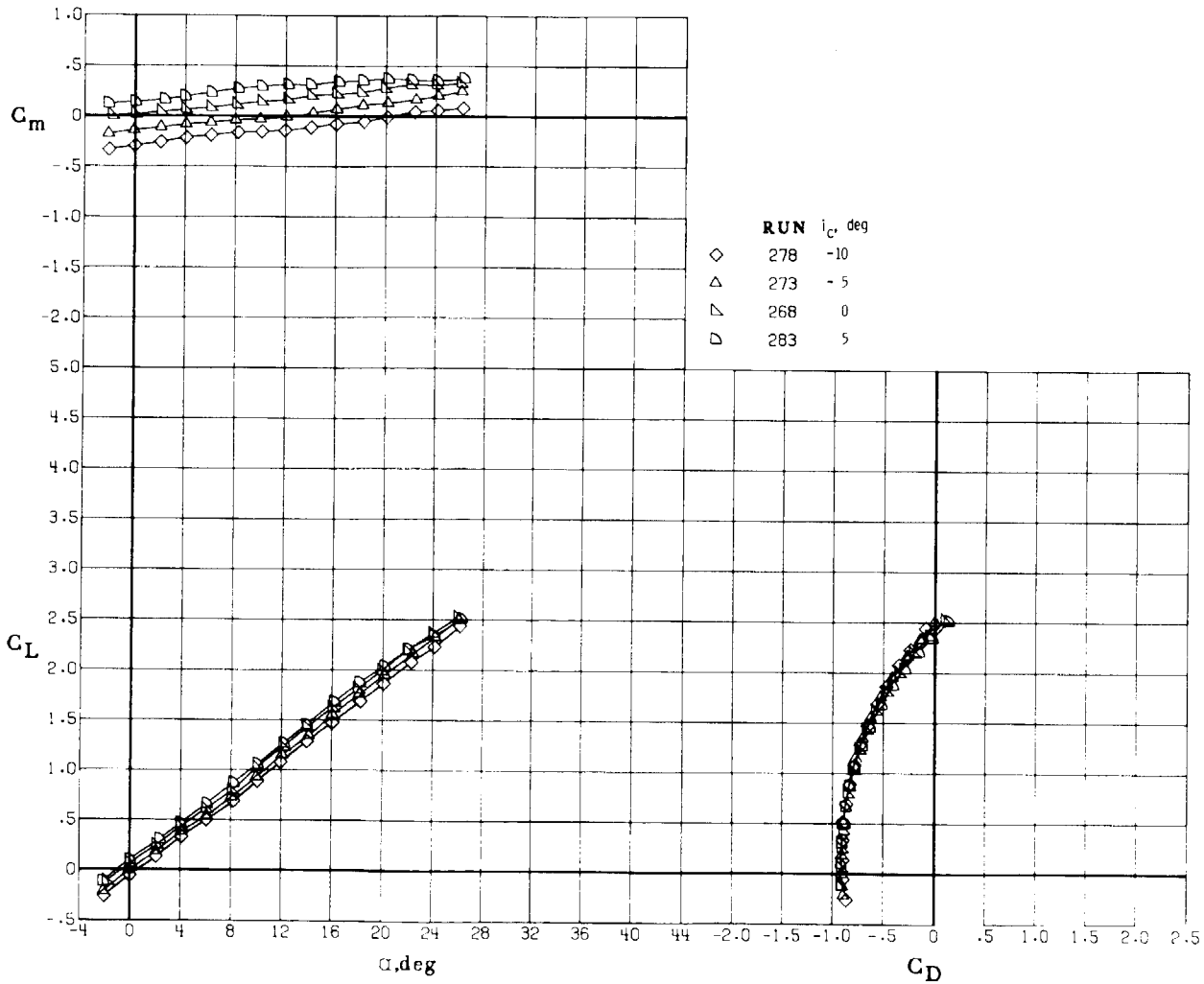

(i) $C_T = 1.0$; $\delta_N = \delta_f = \delta_{le} = 0^o$; $\varepsilon_w = -6^o$.

Figure 16.- Continued.

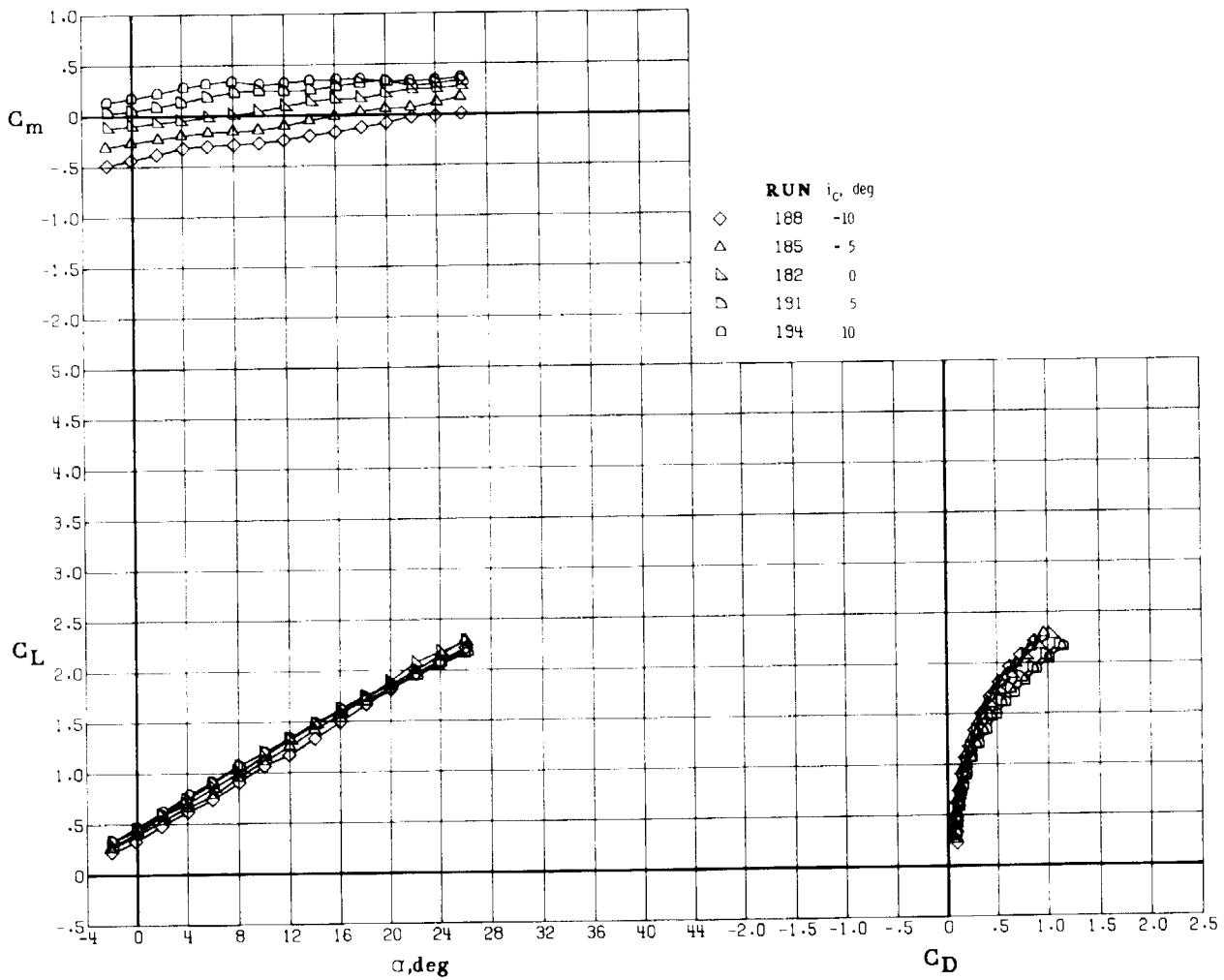

(j) $C_T = 0$; $\delta_N = \delta_f = 20^o$; $\delta_{le} = 0^o$; $\delta_{f,c} = 20^o$; $\varepsilon_w = -6^o$.

Figure 16.- Continued.

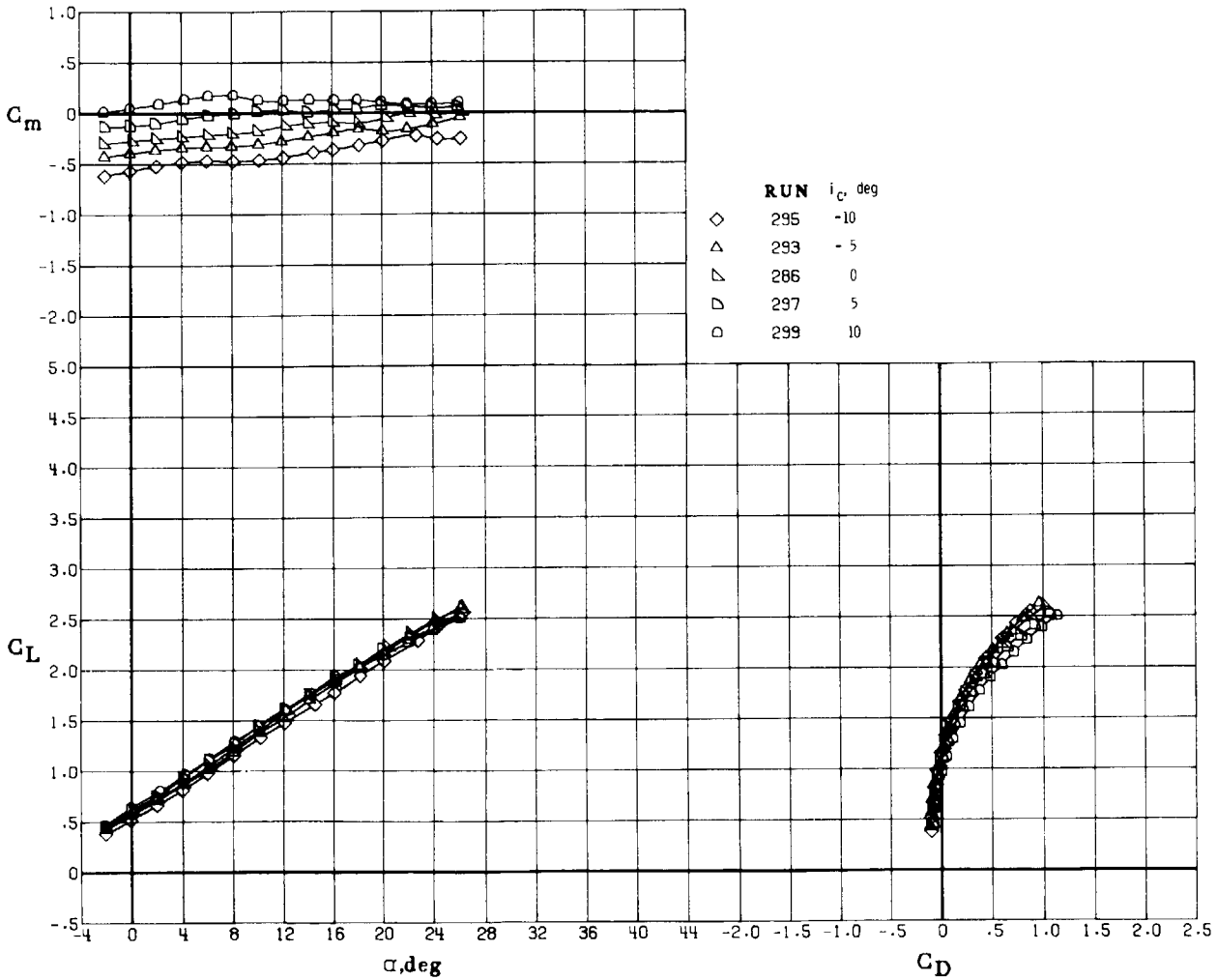

(k) $C_T = 0.2$; $\delta_N = \delta_f = 20^o$; $\delta_{le} = 0^o$; $\delta_{f,c} = 20^o$; $\epsilon_w = -6^o$.

Figure 16.- Continued.

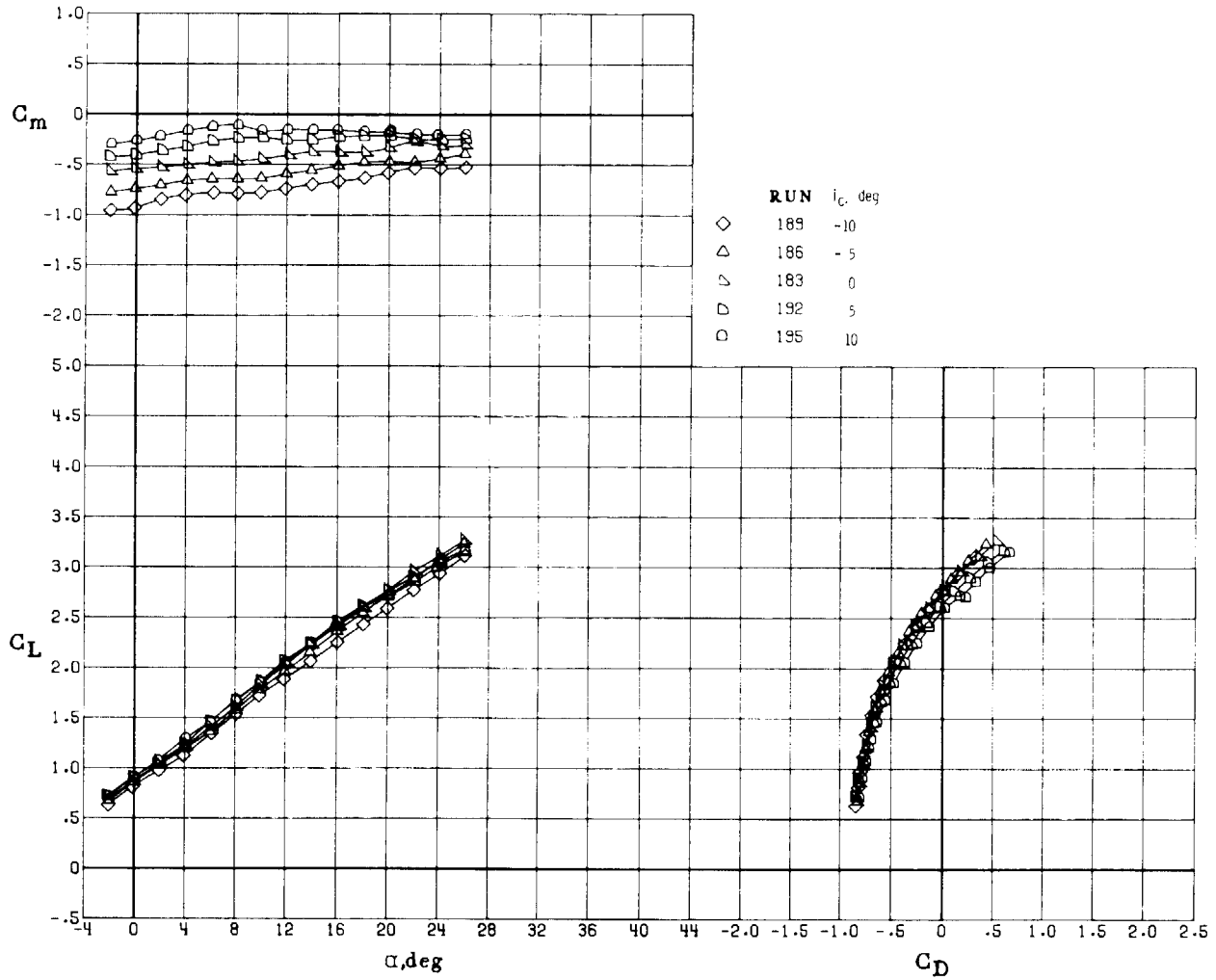

(l) $C_T = 1.0$; $\delta_N = \delta_f = 20^o$; $\delta_{le} = 0^o$; $\delta_{f,c} = 20^o$; $\varepsilon_w = -6^o$.

Figure 16.- Continued.

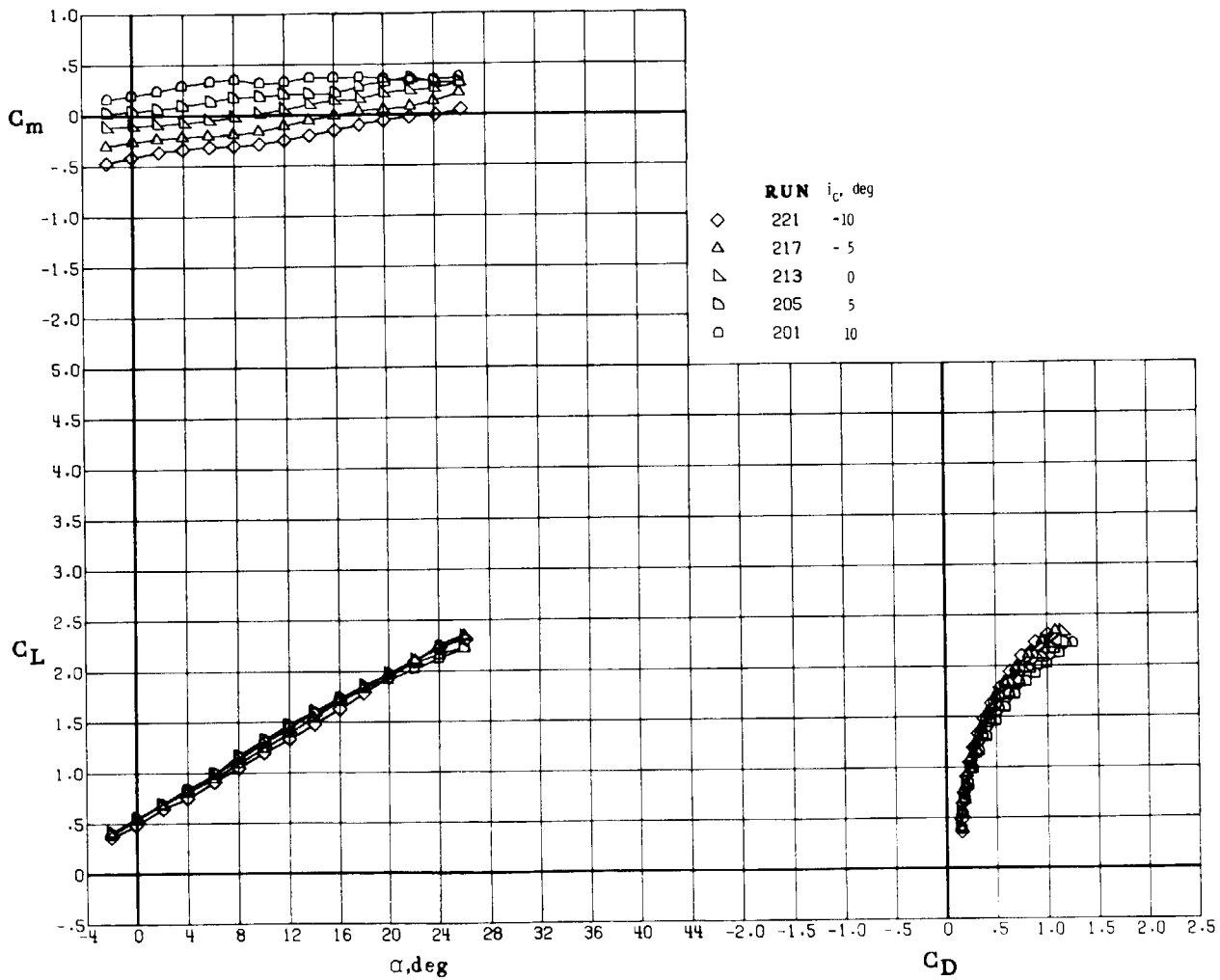

(m) $C_T = 0$; $\delta_N = \delta_f = 40^o$; $\delta_{le} = 0^o$; $\delta_{f,c} = 40^o$; $\varepsilon_w = -6^o$.

Figure 16.- Continued.

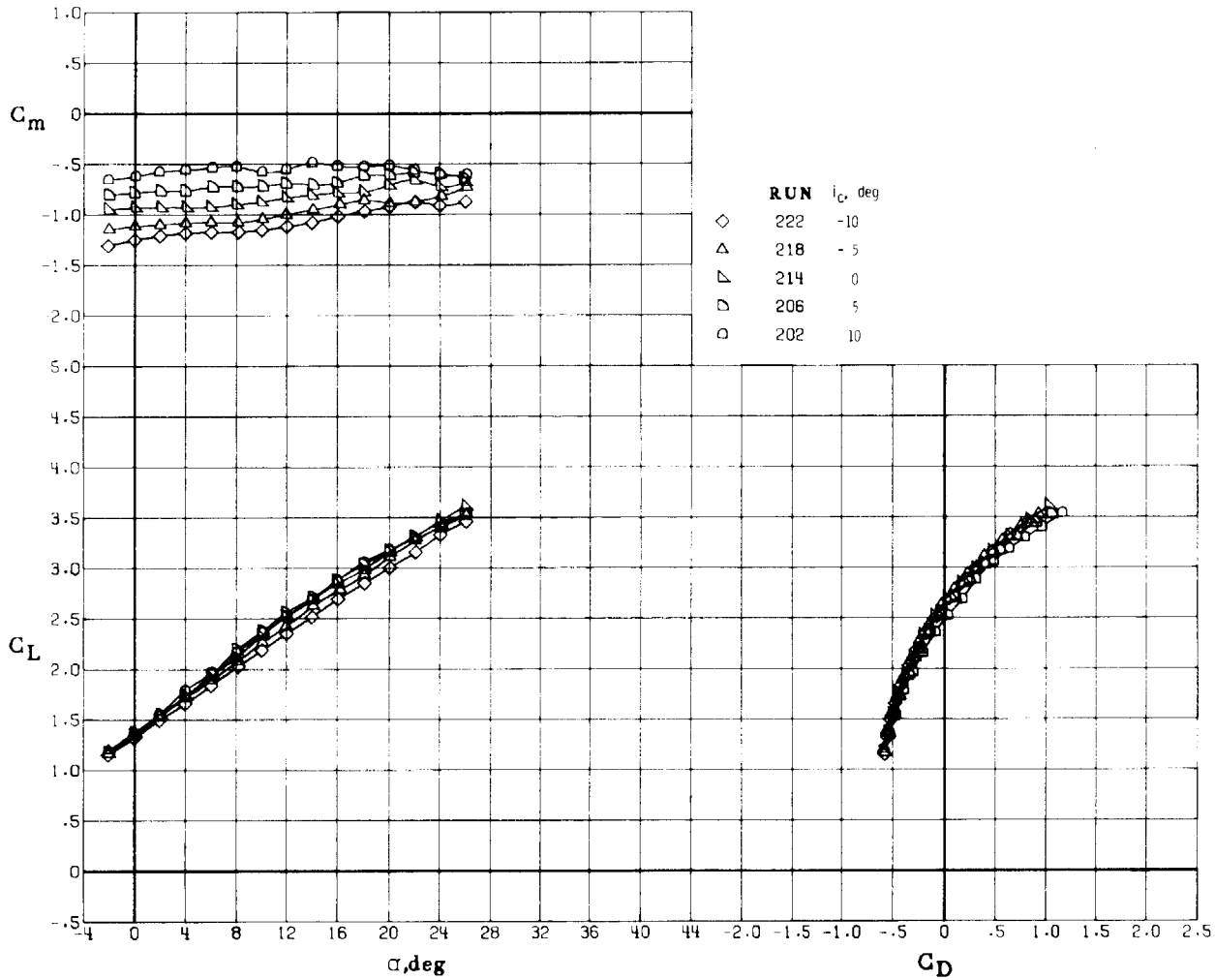

(n) $C_T = 1.0$; $\delta_N = \delta_f = 40^o$; $\delta_{le} = 0^o$; $\delta_{f,c} = 40^o$; $\varepsilon_w = -6^o$.

Figure 16.- Continued

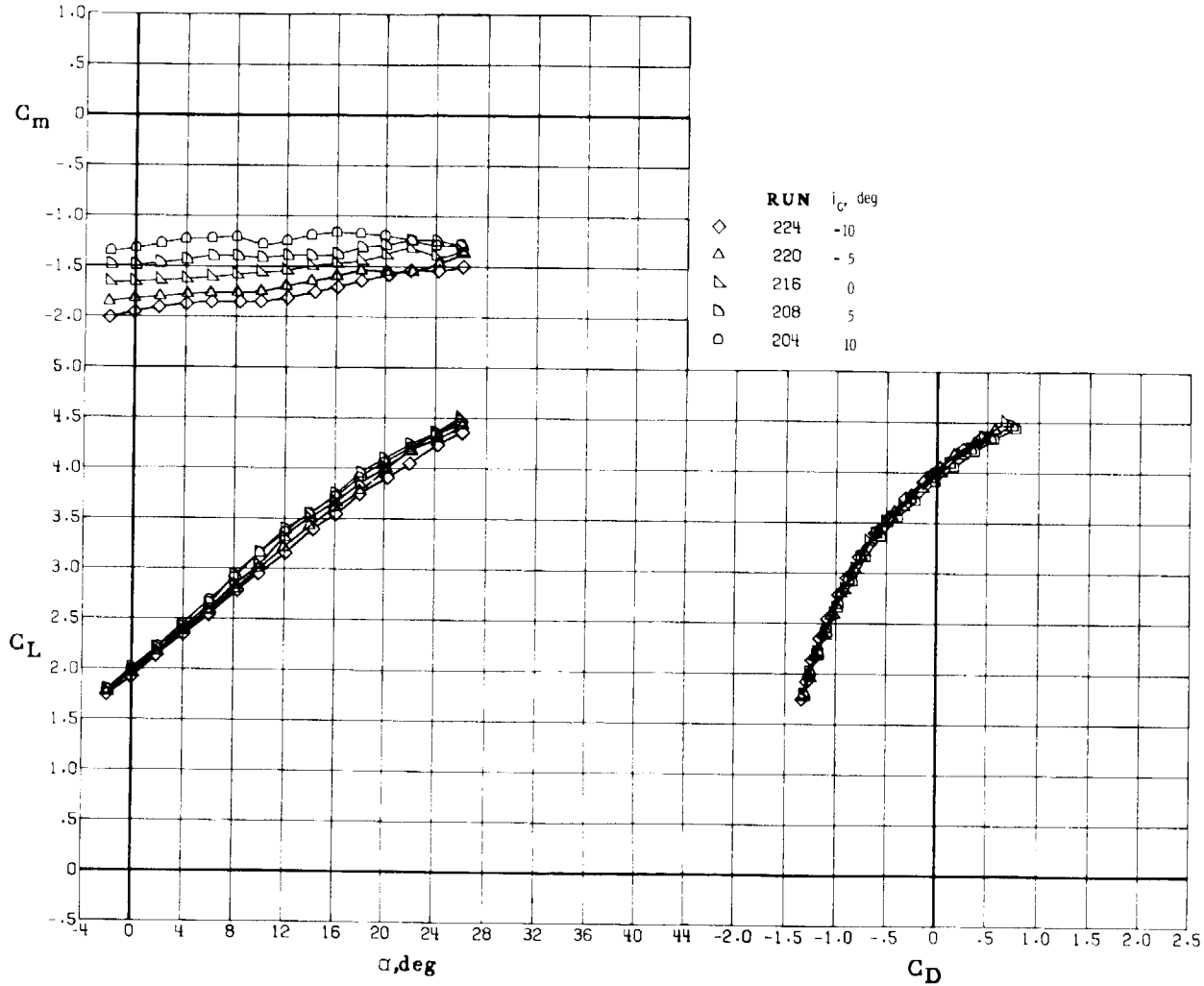

(o) $C_T = 2.0$; $\delta_N = \delta_f = 40^o$; $\delta_{le} = 0^o$; $\delta_{f,c} = 40^o$; $\varepsilon_w = -6^o$.

Figure 16.- Concluded.

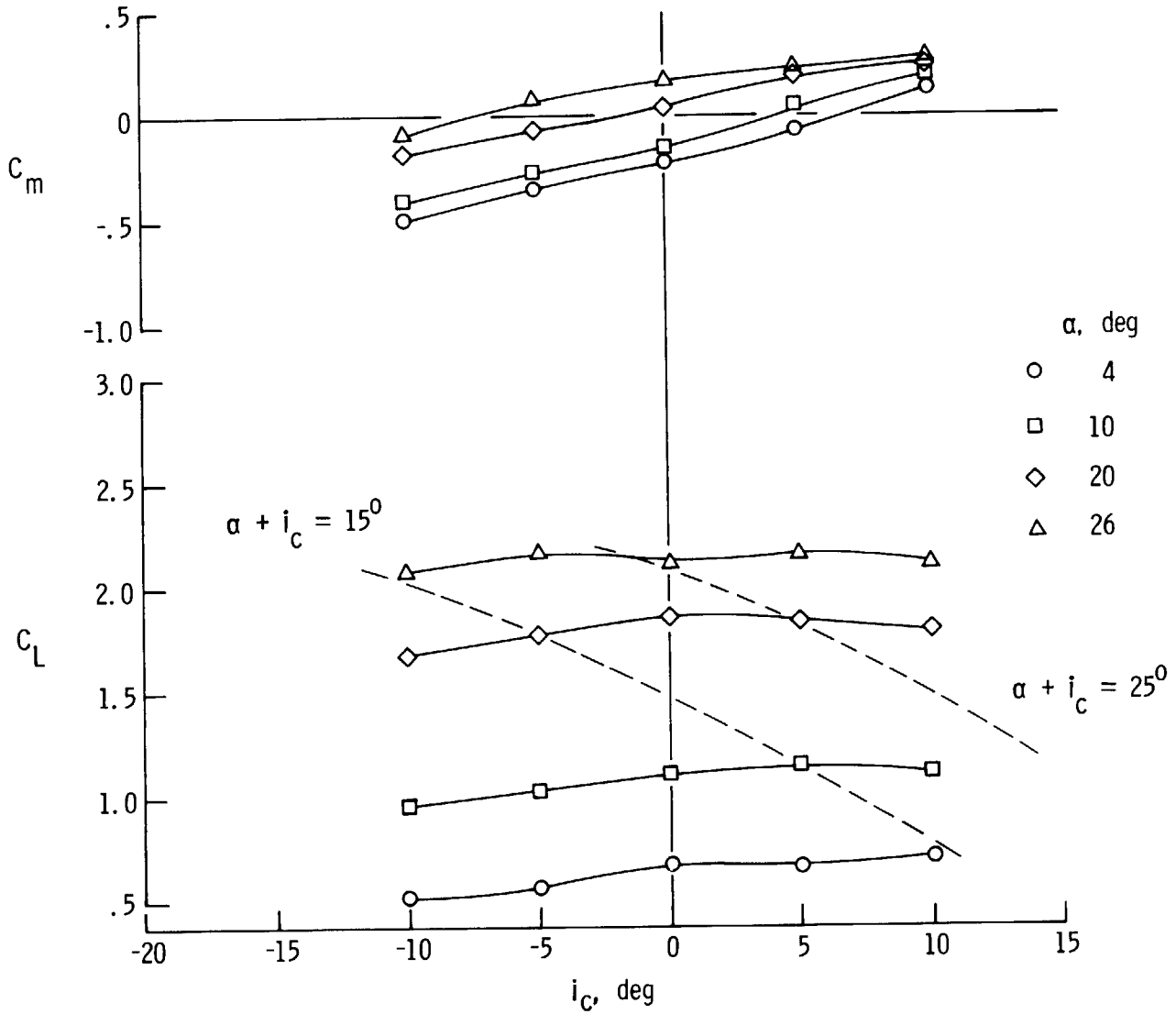

(a) $\delta_f = \delta_N = 20^o$; $\delta_{le} = \delta_{f,c} = \delta_{le,c} = 0$; $C_T = 0$; $\epsilon_w = -6^o$.

Figure 17.- Detailed effect of canard incidence on C_L and C_m for new wing-canard configuration.

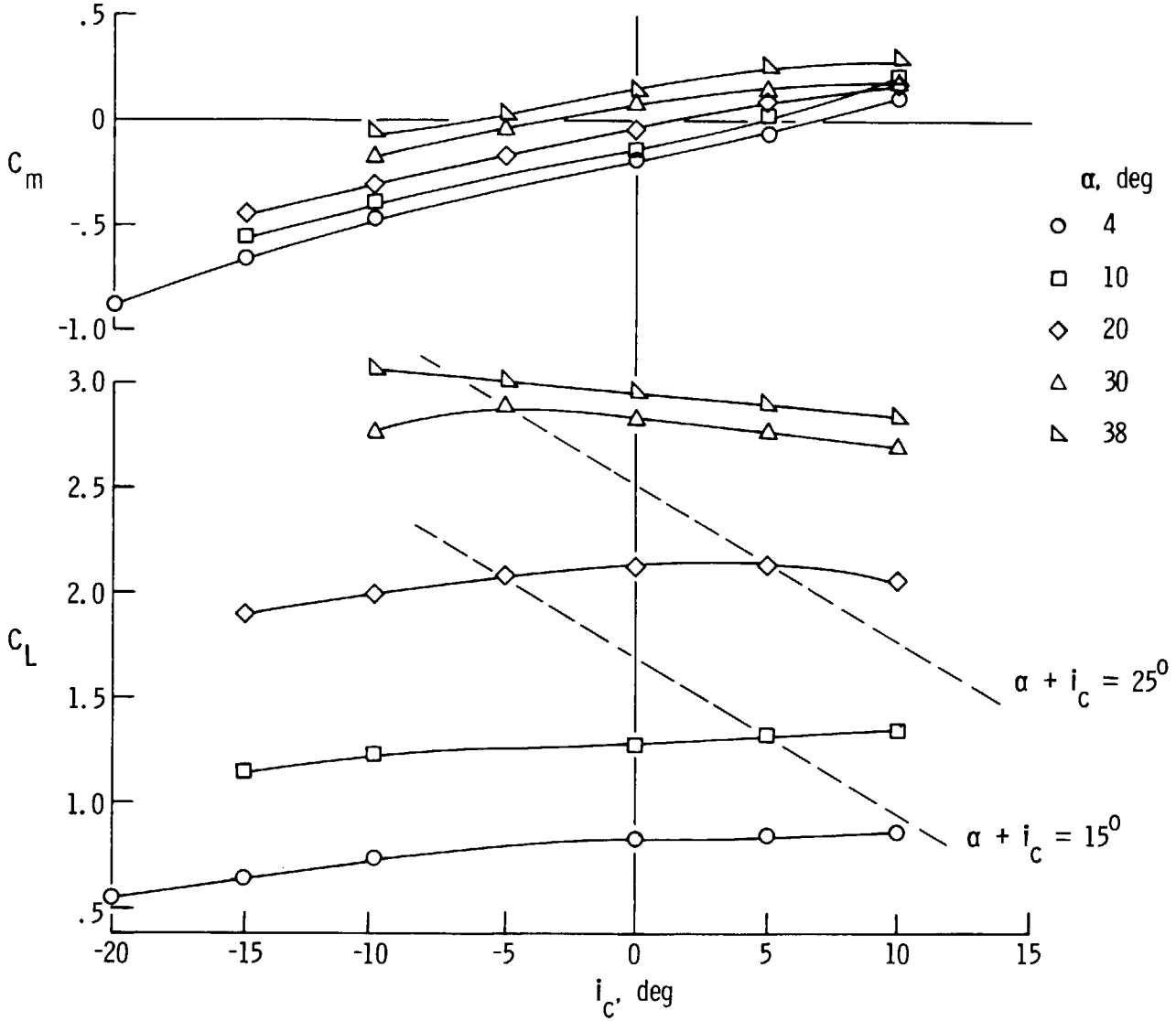

(b) $\delta_f = \delta_N = \delta_{le} = \delta_{f,c} = \delta_{le,c} = 20^o$; $C_T = 0.2$; $\varepsilon_w = -12^o$.

Figure 17.- Continued.

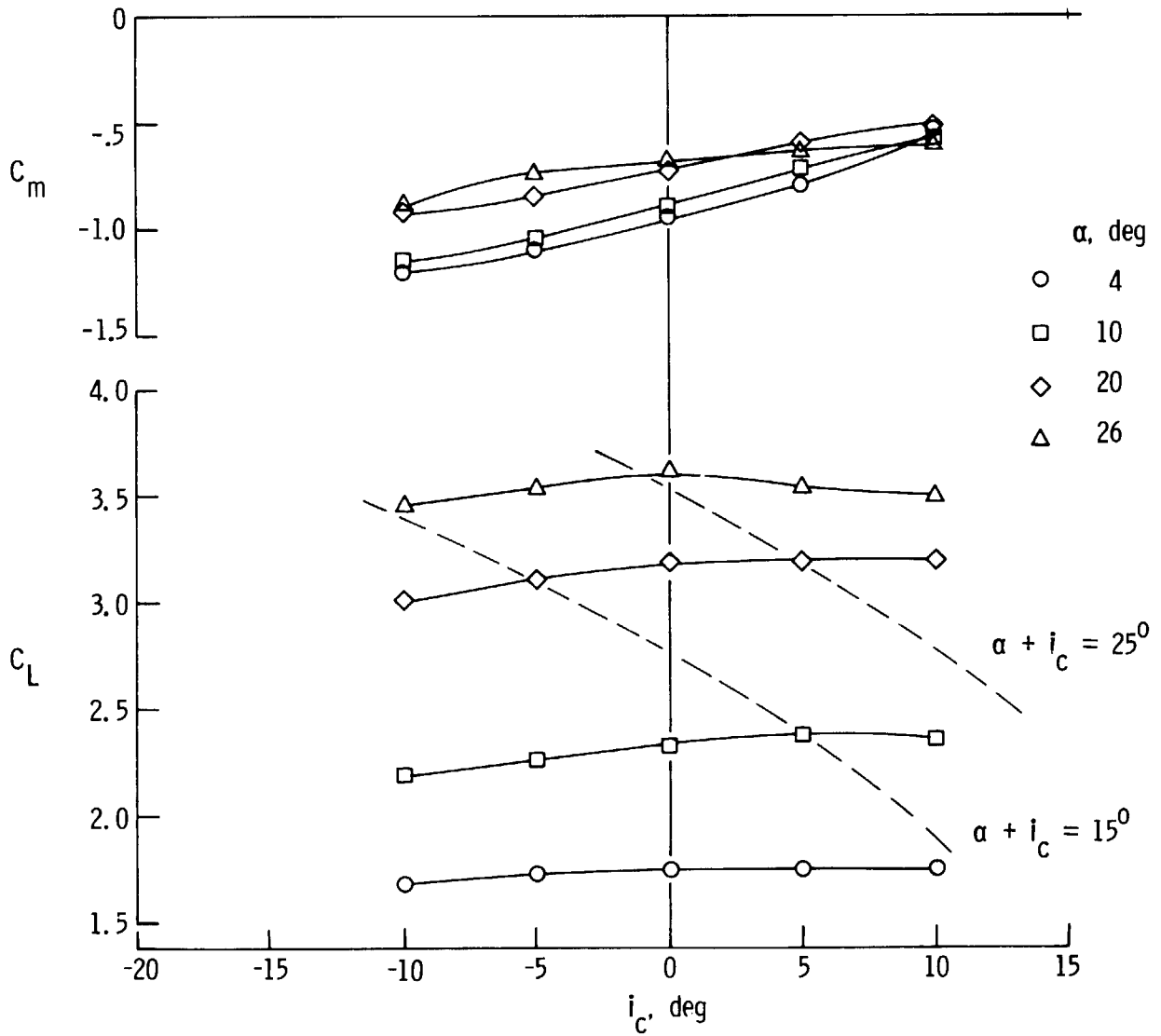

(c) $\delta_f = \delta_N = 40^o$; $\delta_{le} = 0^o$; $\delta_{f,c} = 40^o$; $\delta_{le,c} = 0^o$; $C_T = 1.0$; $\varepsilon_w = -6^o$.

Figure 17.- Concluded.

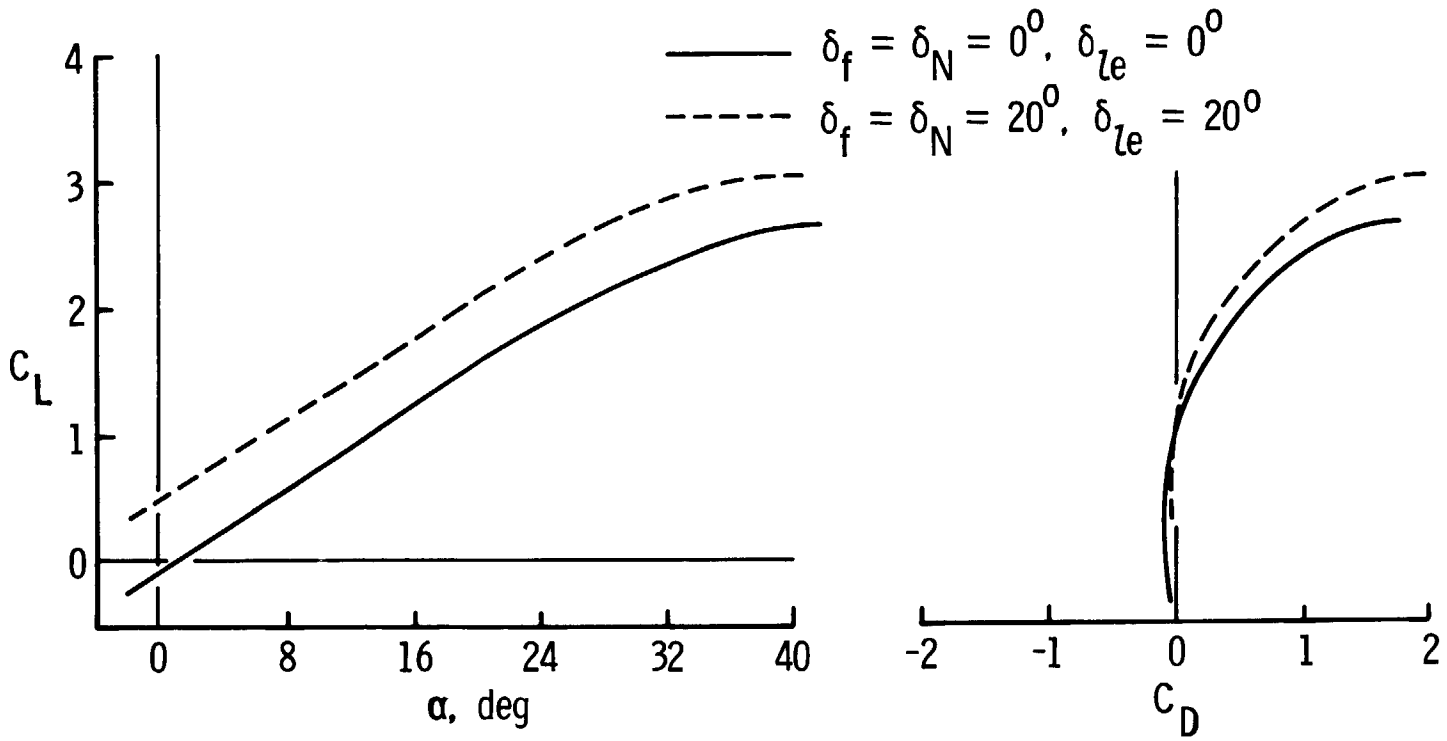

Figure 18.- Trimmed lift curve and lift-drag polars for new wing-canard configuration. $C_T = 0.2$; $\delta_{f,c} = \delta_{le,c} = 0^o$; $\varepsilon_w = -12^o$.

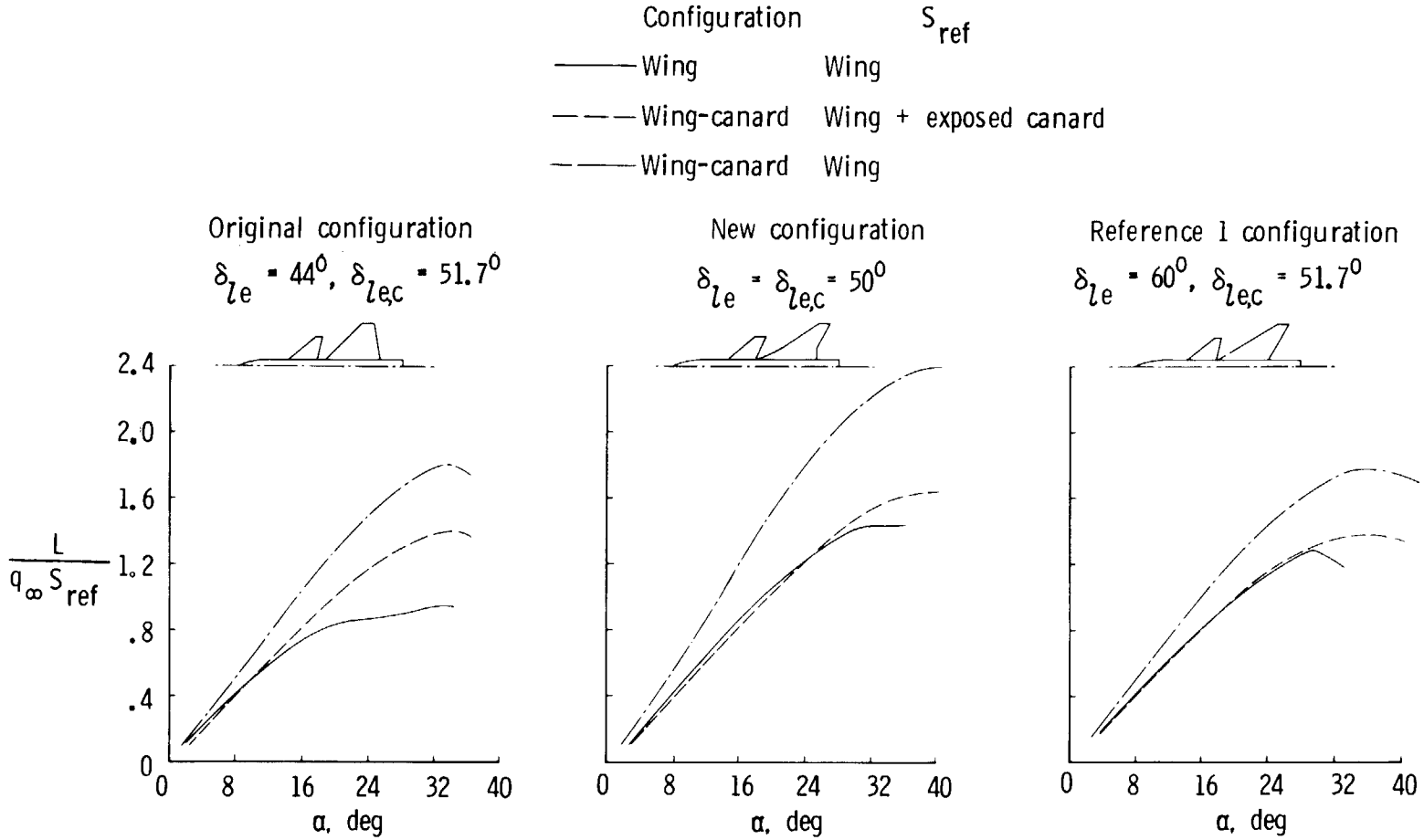

Figure 19.- Comparison of several configurations for canard effect on lift coefficient based on wing area and wing area plus exposed canard area. $C_T = 0$.

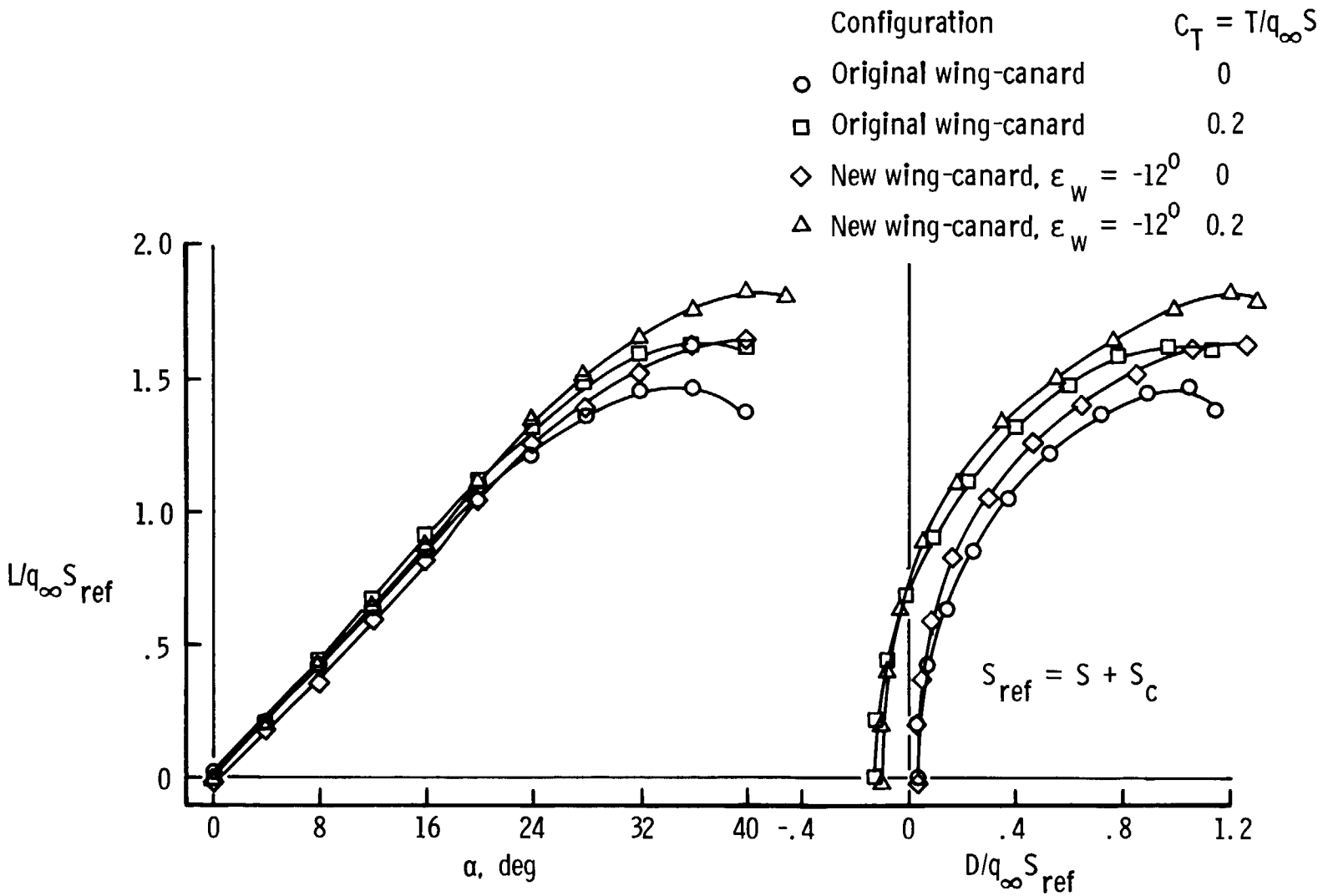

(a) Lift curve and lift-drag polar.

Figure 20.- Comparison of performance data for original and new wing-canard configurations.

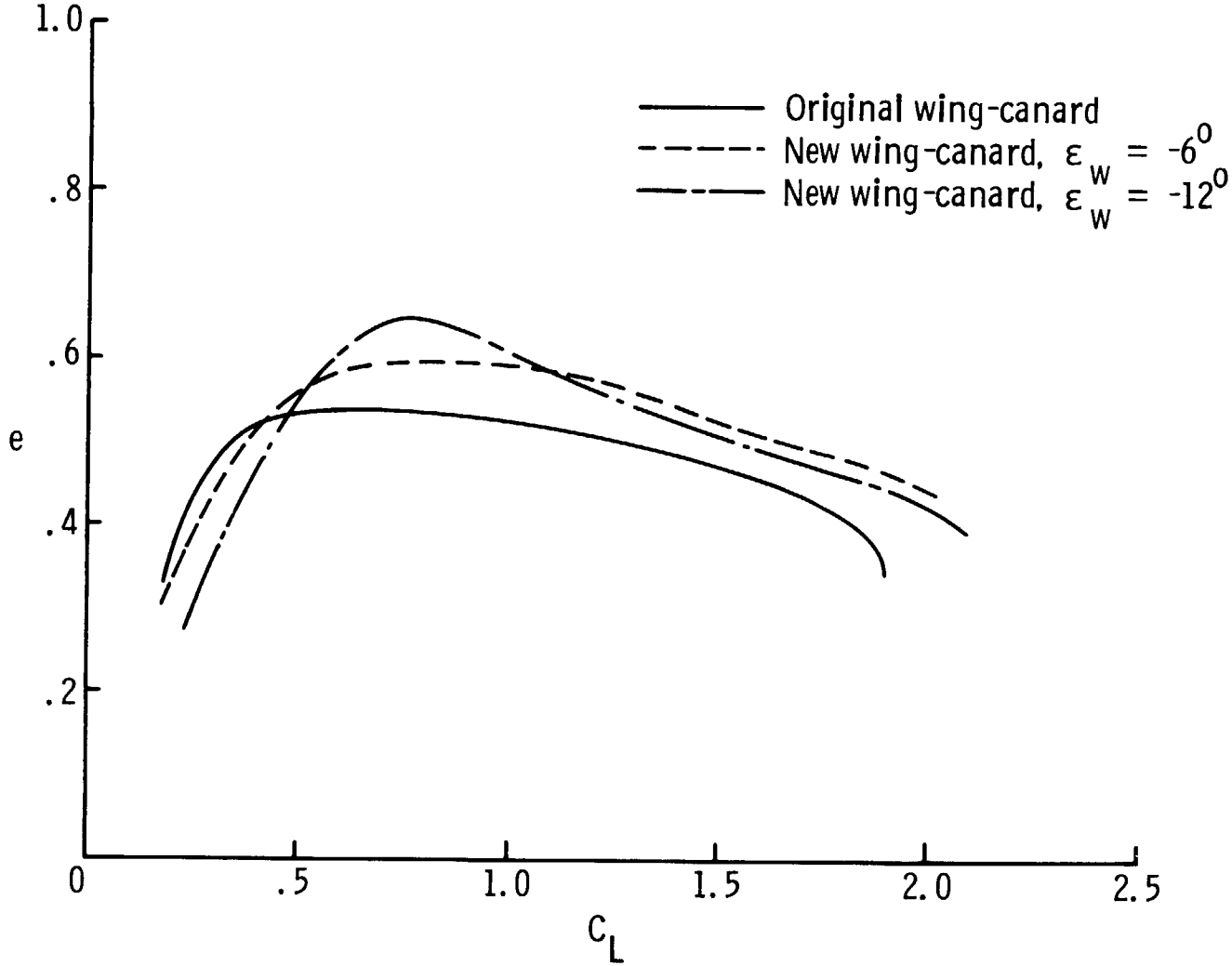

(b) Drag-due-to-lift efficiency factor.

Figure 20.- Concluded.

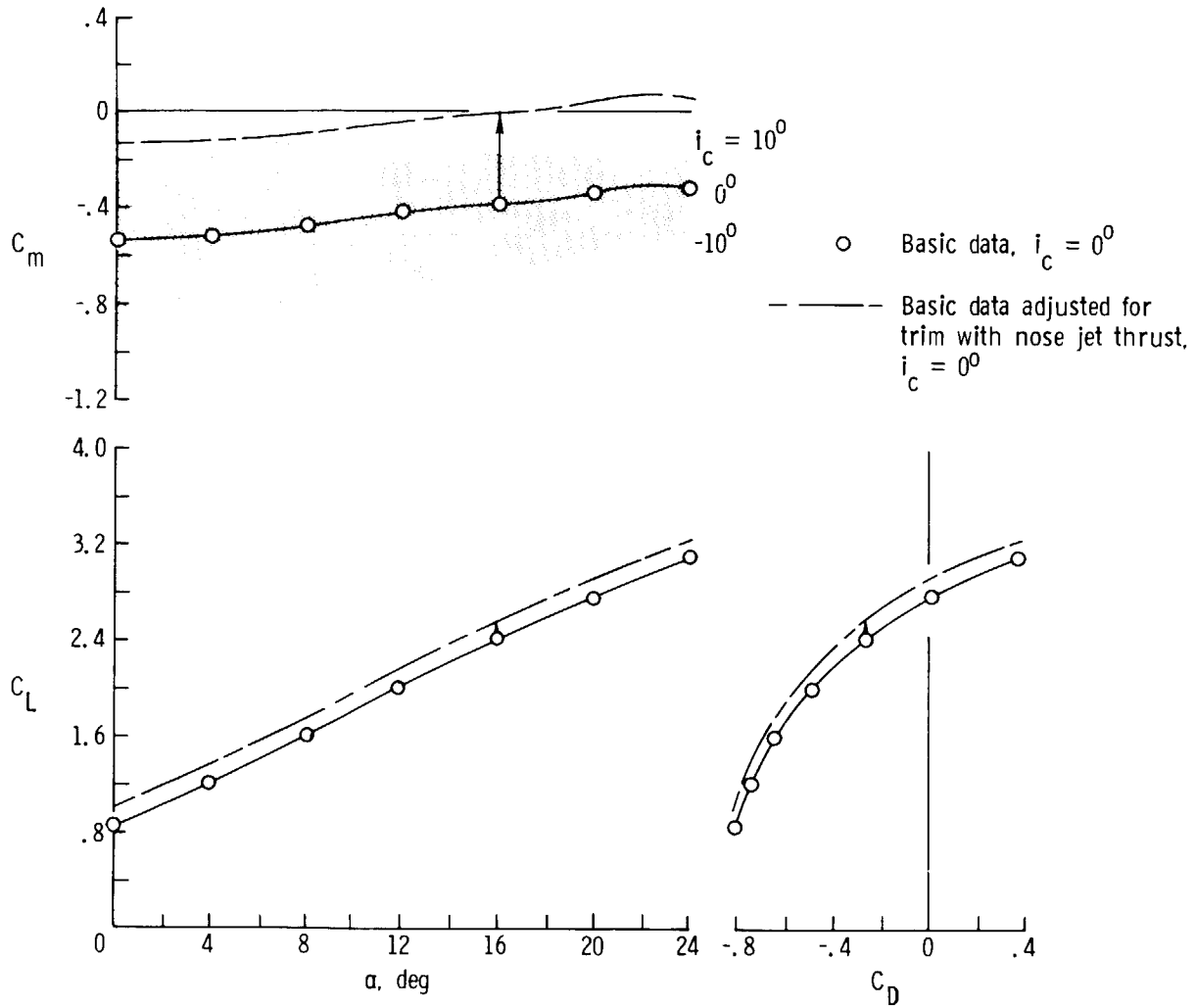

(a) Takeoff $\delta_f = \delta_N = 20^o$; $\delta_{f,c} = 20^o$; $C_T = 1.0$.

Figure 21.- Longitudinal aerodynamics of high flap and nozzle deflections and high thrust coefficients. Trim with nose jet.

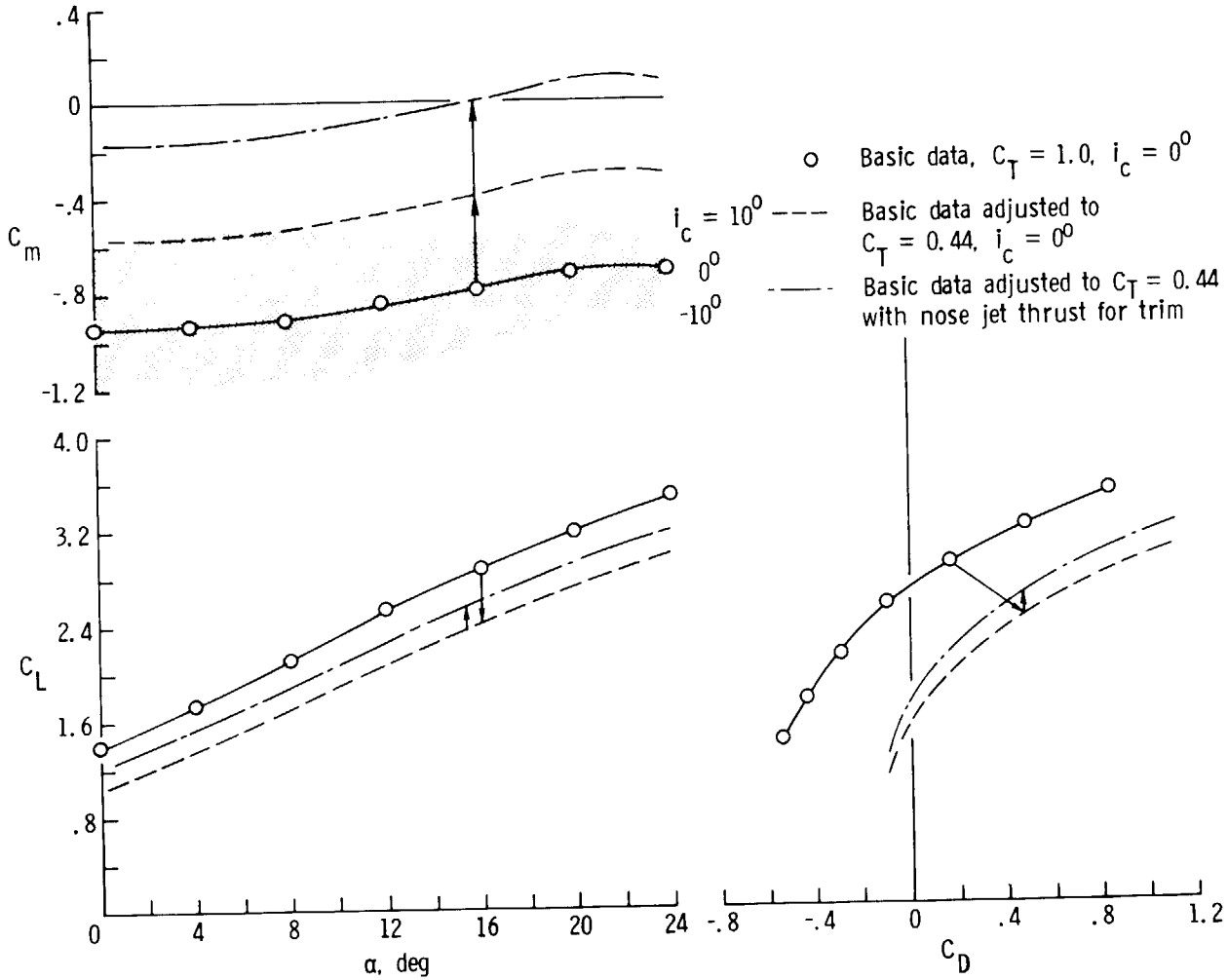

(b) Landing $\delta_f = \delta_N = 40^o$; $\delta_{f,c} = 40^o$.

Figure 21.- Concluded.

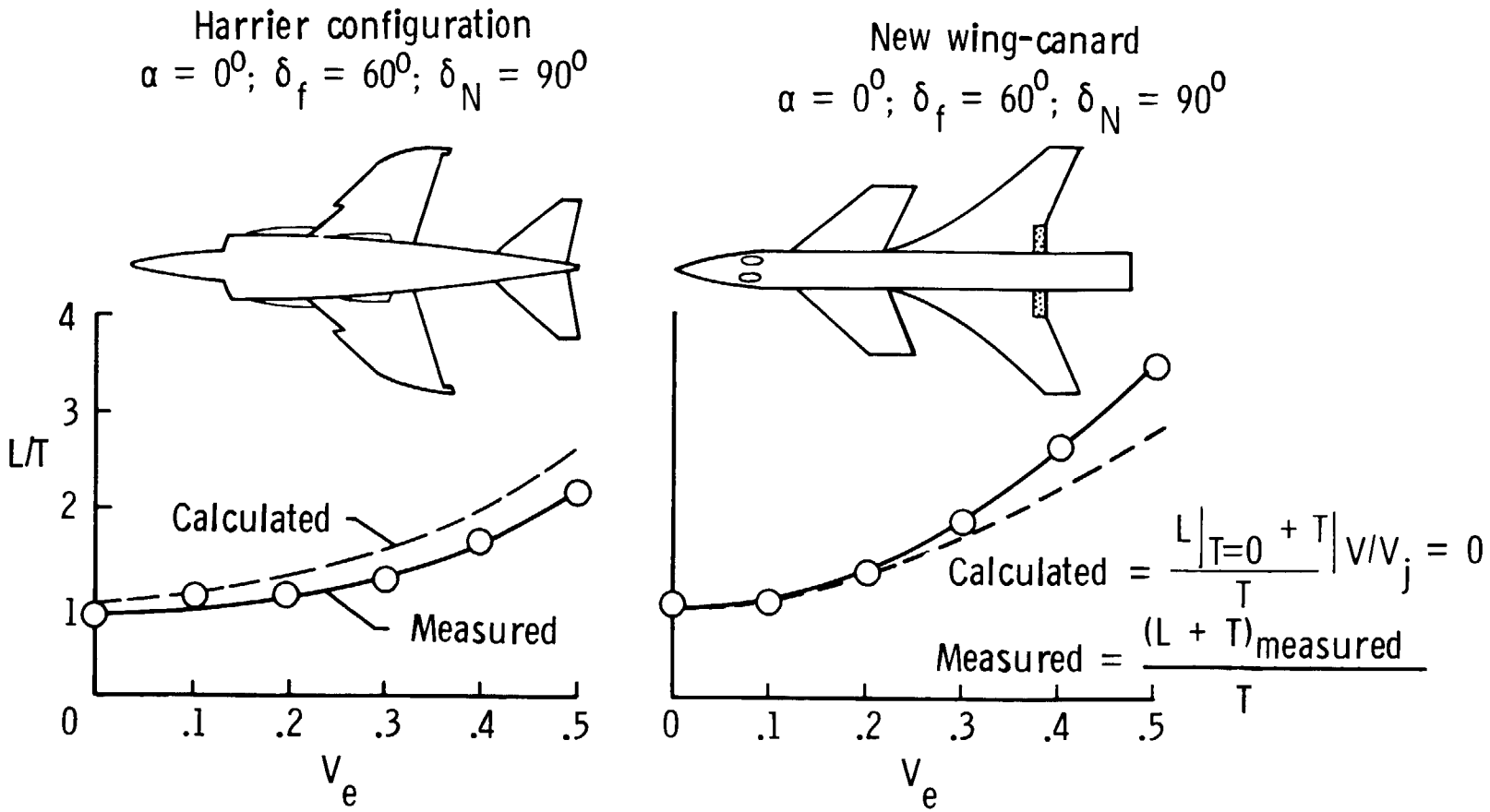

Figure 22.- Interference effects in hover and transition.

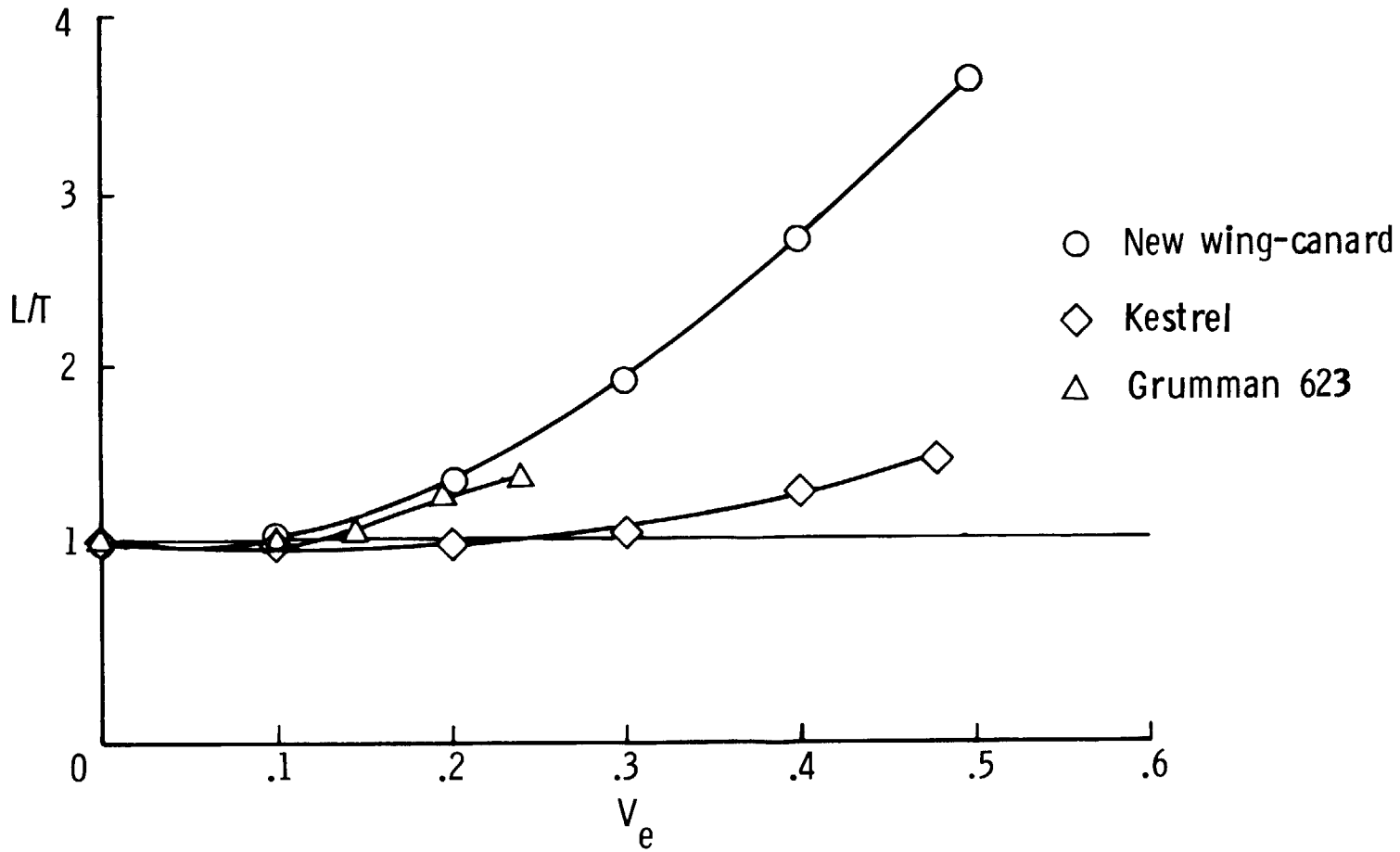

(a) L/T versus V_e.

Figure 23.- Comparison of transition aerodynamic effects for three V/STOL configurations. $\alpha = 0^o$; $\delta_N = 90^o$; $\delta_f = 60^o$.

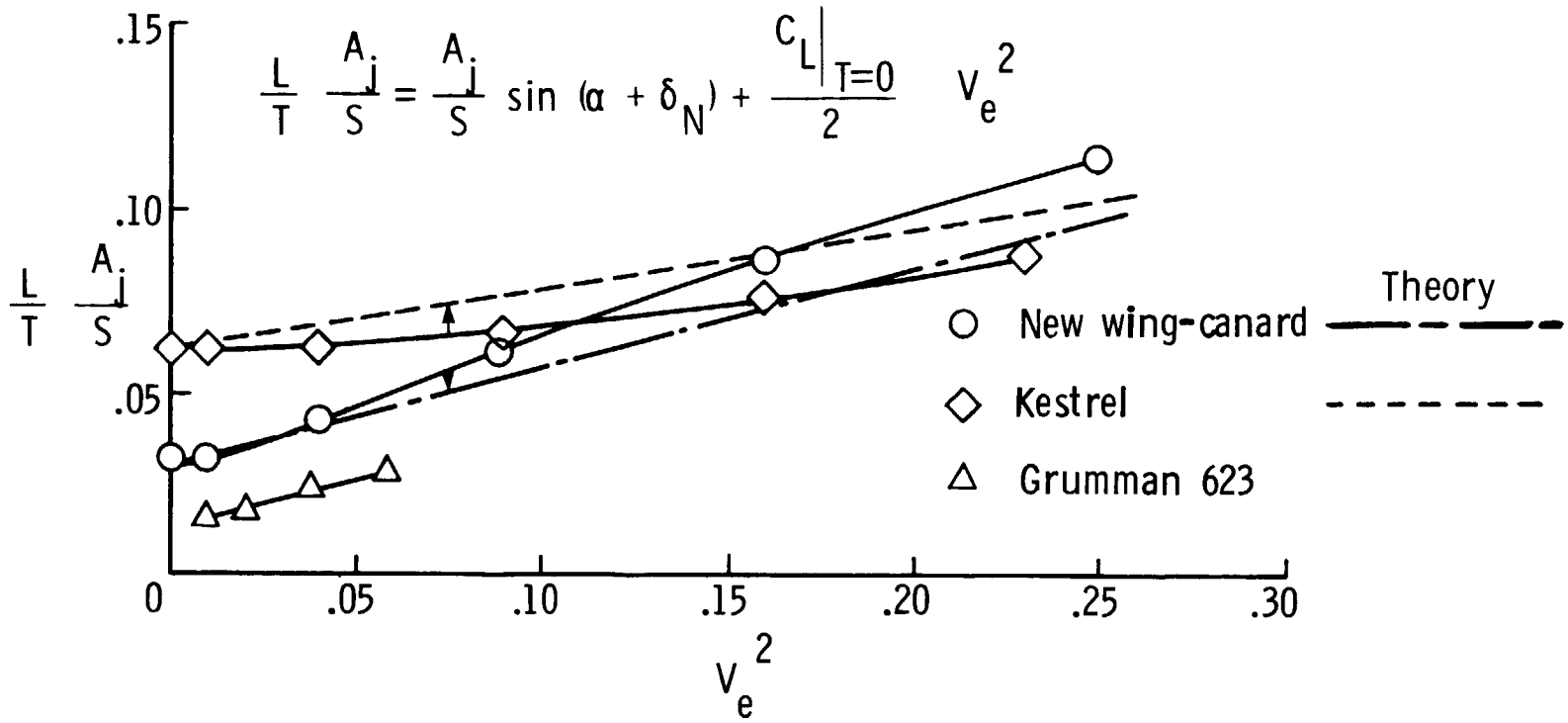

(b) $\frac{L}{T}\frac{A_j}{S}$ versus V_e^2.

Figure 23.- Concluded.

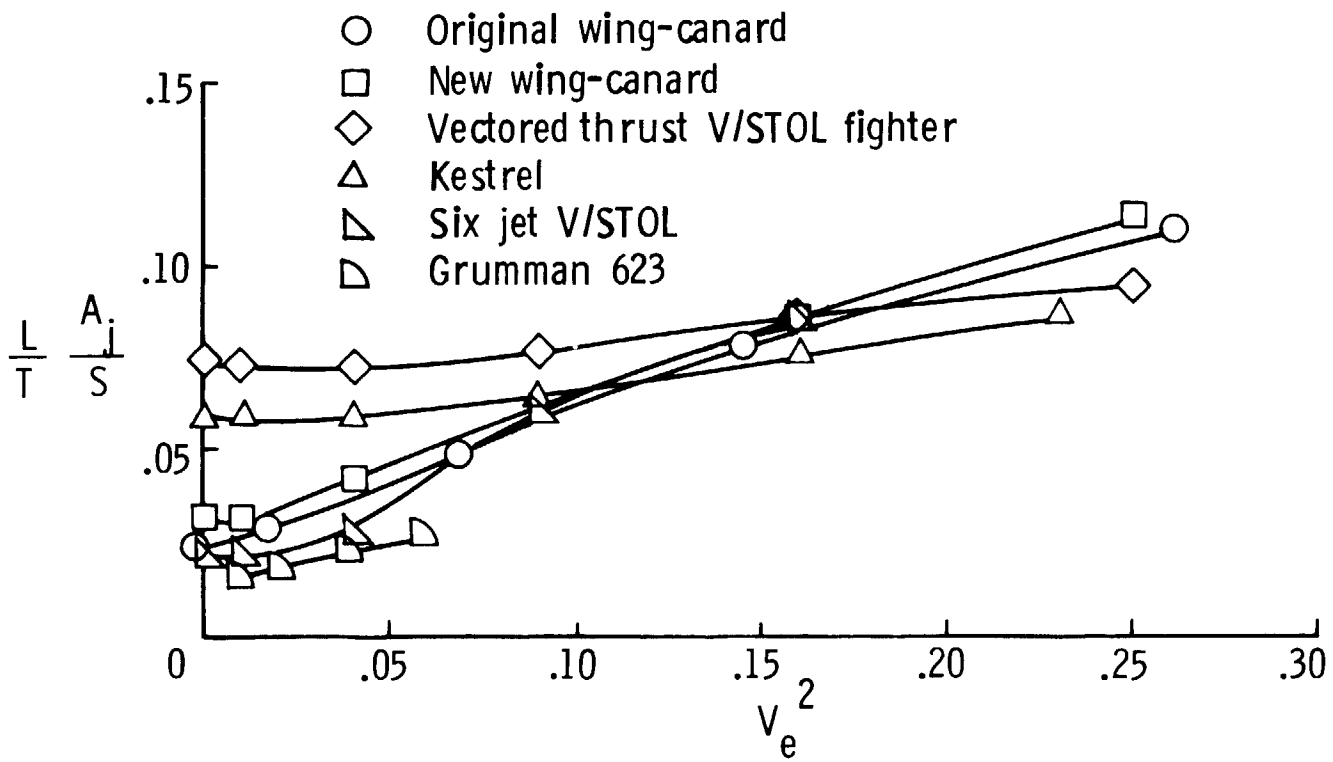

(a) $\alpha = 0^o$; $\delta_N = 90^o$; $\delta_f = 60^o$.

Figure 24.- Comparison of transition aerodynamic effects for several V/STOL configurations.

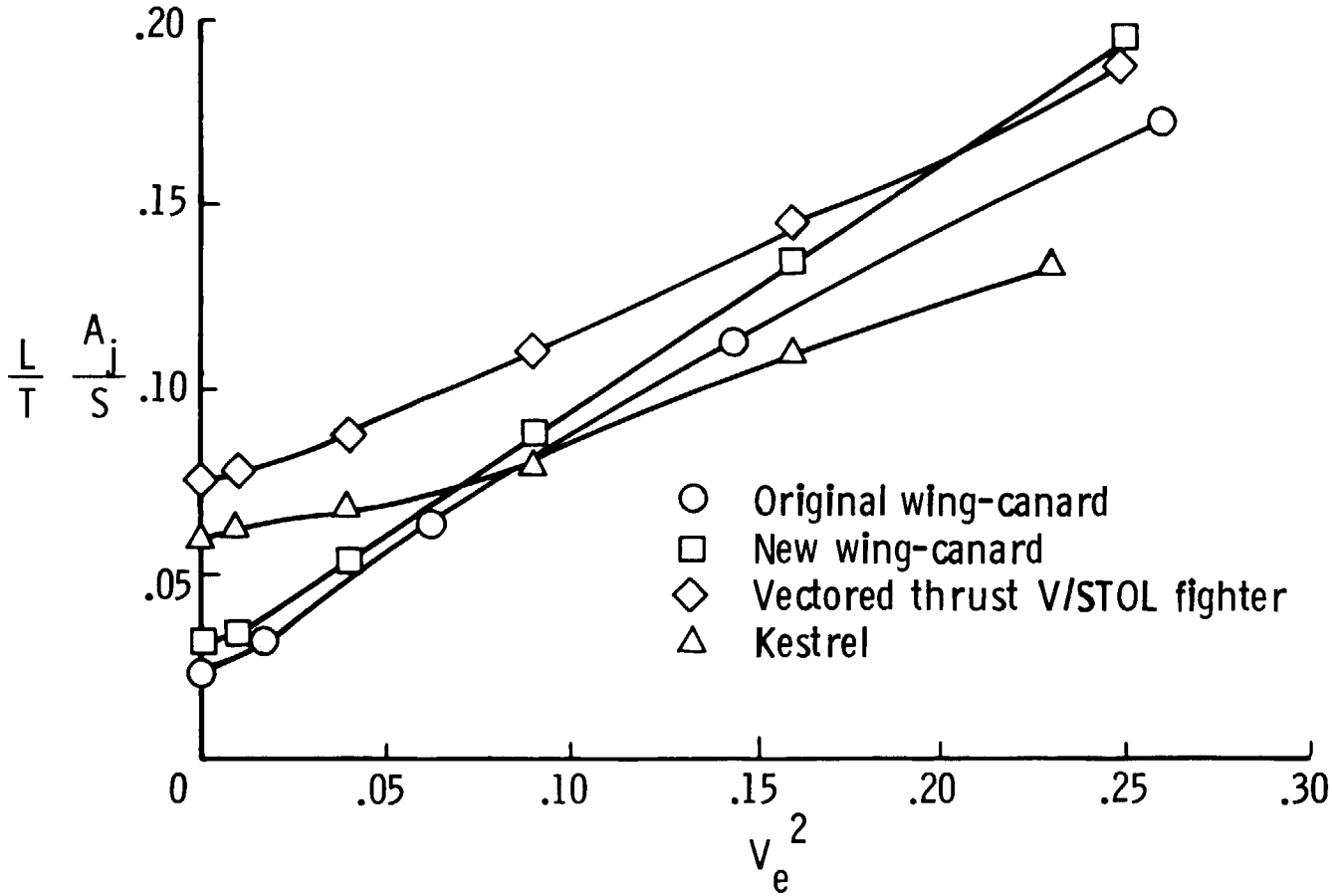

(b) $\alpha = 10^{\circ}$; $\delta_N = 90^{\circ}$; $\delta_f = 60^{\circ}$.

Figure 24.- Continued.

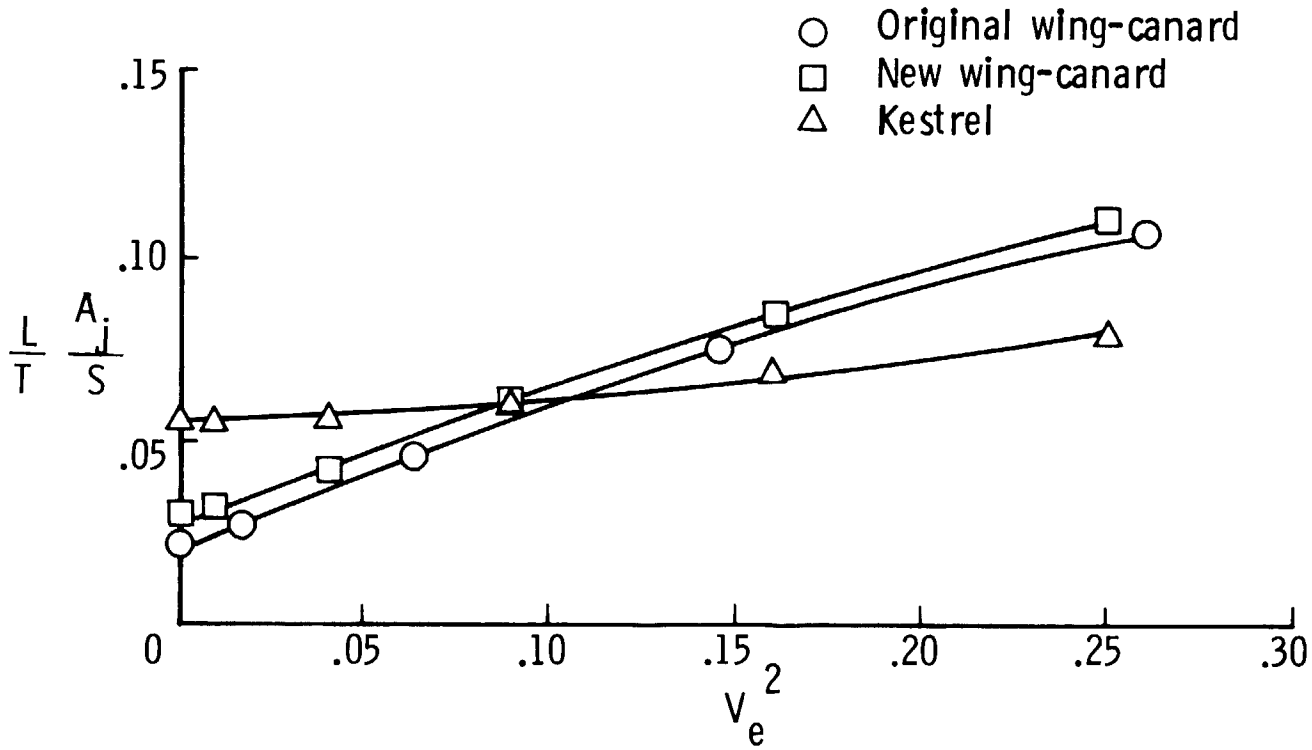

(c) $\alpha = 0^{\circ}$; $\delta_N = 60^{\circ}$; $\delta_f = 60^{\circ}$.

Figure 24.- Continued.

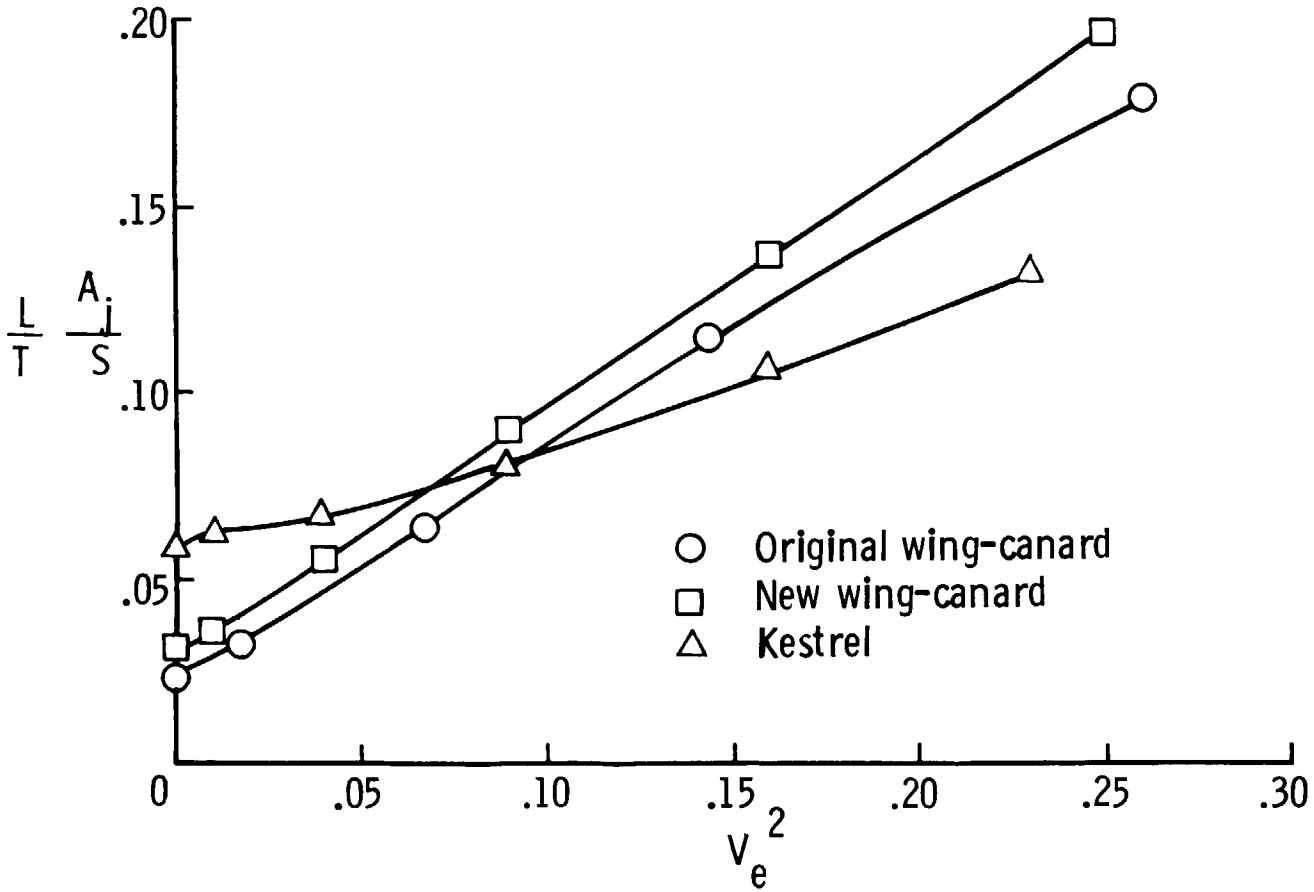

(d) $\alpha = 10^{\circ}$; $\delta_N = 60^{\circ}$; $\delta_f = 60^{\circ}$.

Figure 24.- Concluded.

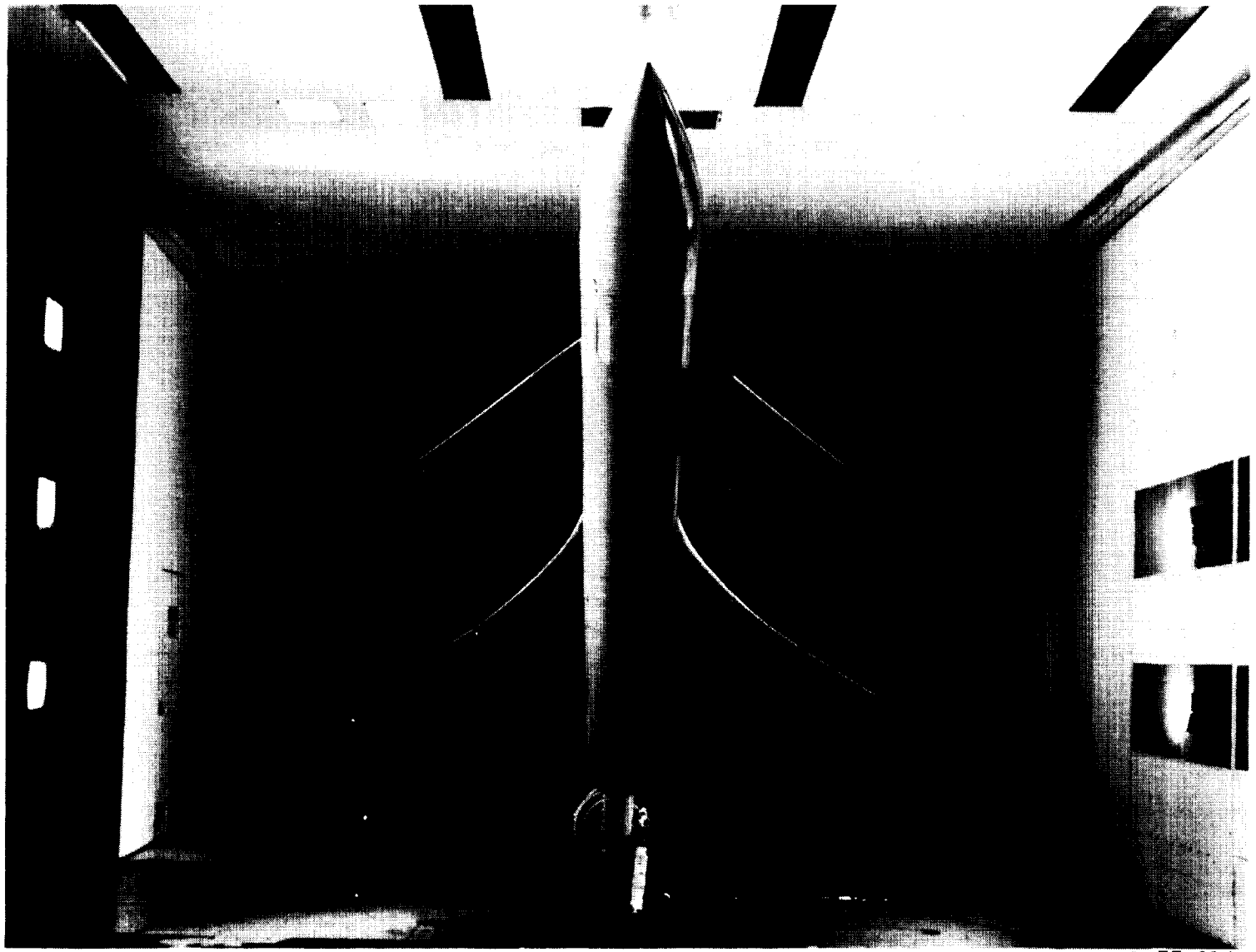

L-77-8145

Figure 25.- Photograph of new wing-canard configuration showing planform shape.

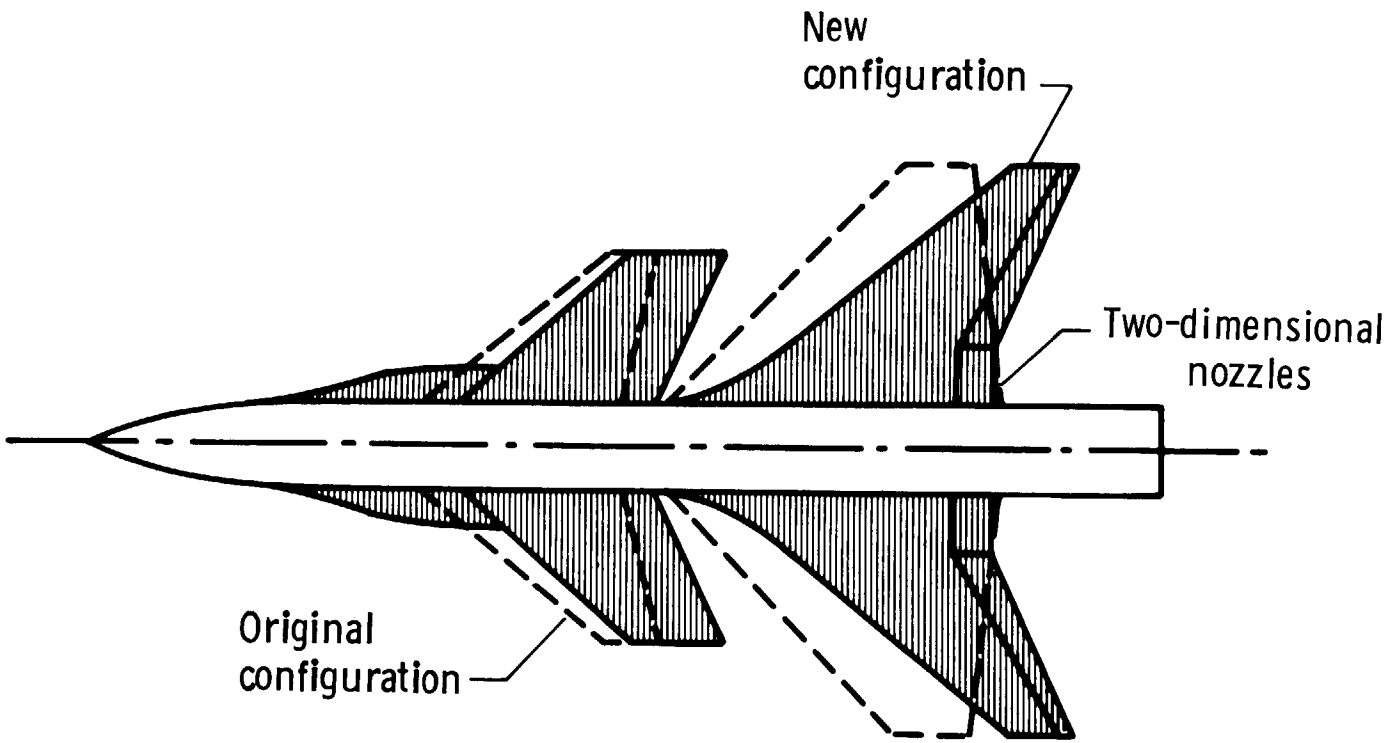

Figure 26.- Comparison of original and new wing-canard configuration planform geometry.

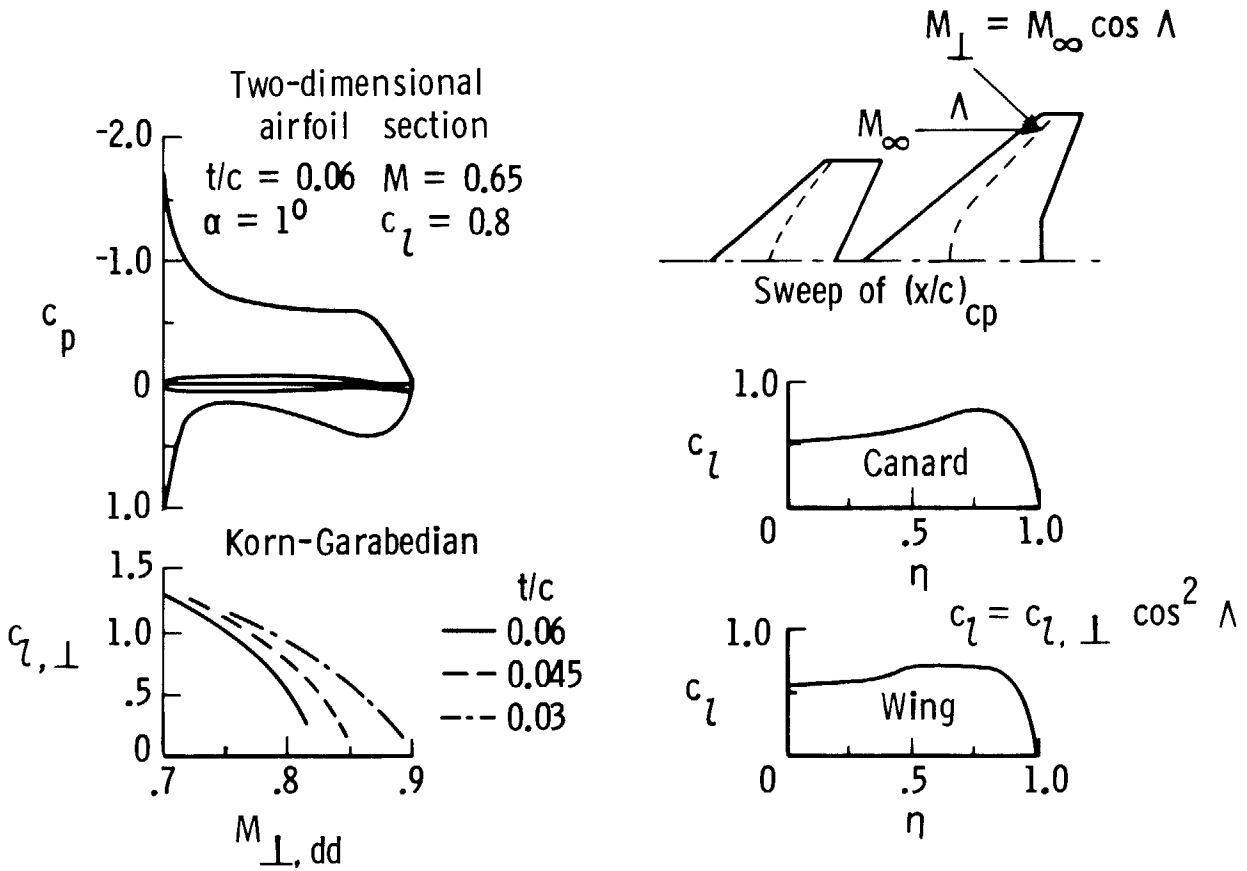

Figure 27.- Maximum section-lift coefficients for new wing-canard planform based on drag divergence.

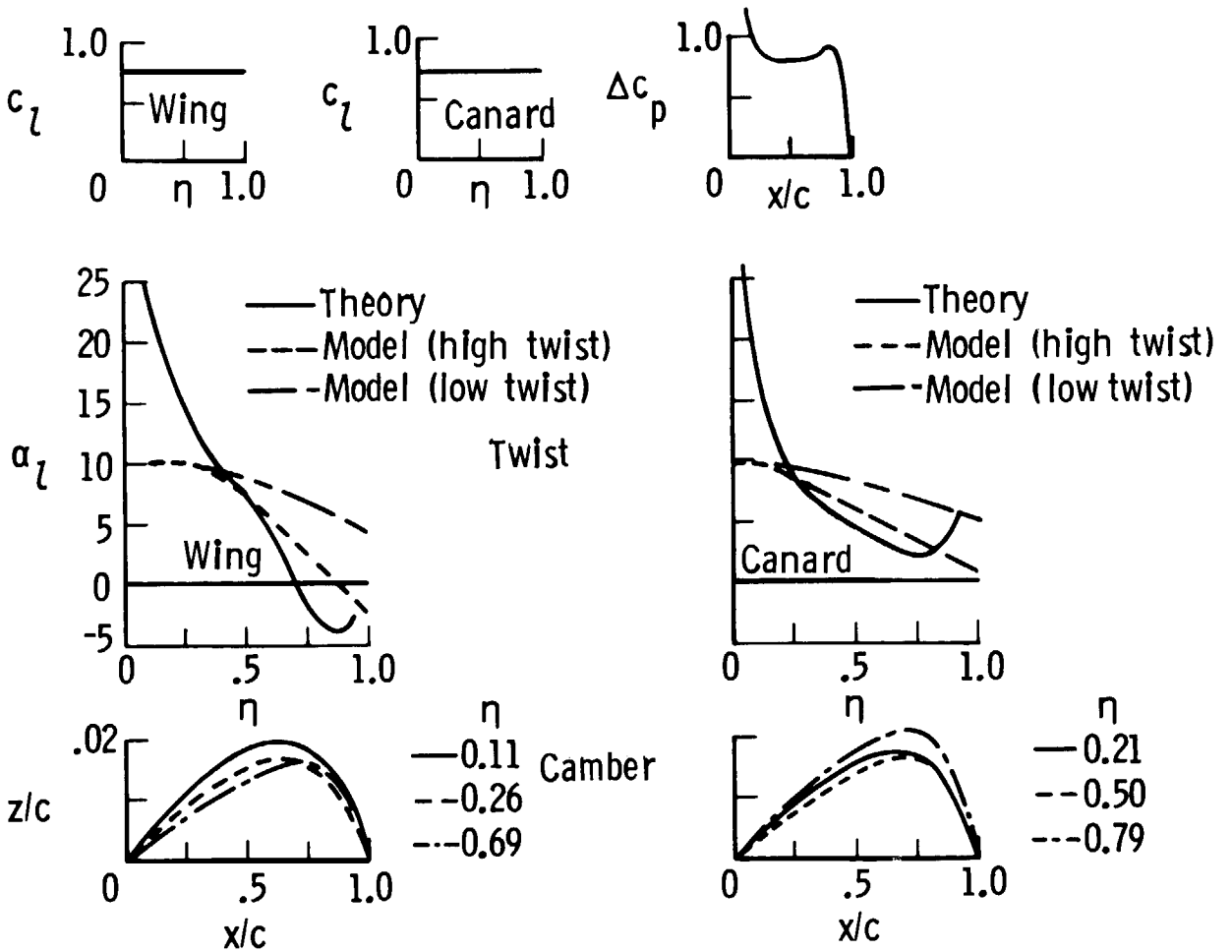

Figure 28.- Twists and cambers for new wing-canard planform based on two-dimensional chord load and constant c_l.

1. Report No.	2. Government Accession No.	3. Recipient's Catalog No.
NASA TP-1535		

4. Title and Subtitle	5. Report Date
SUMMARY OF LOW-SPEED LONGITUDINAL AERODYNAMICS OF TWO POWERED CLOSE-COUPLED WING-CANARD FIGHTER CONFIGURATIONS	December 1979
	6. Performing Organization Code
7. Author(s)	8. Performing Organization Report No.
John W. Paulson, Jr., and James L. Thomas	L-13157
	10. Work Unit No.
9. Performing Organization Name and Address	505-43-23-04
NASA Langley Research Center Hampton, VA 23665	11. Contract or Grant No.
	13. Type of Report and Period Covered
12. Sponsoring Agency Name and Address	Technical Paper
National Aeronautics and Space Administration Washington, DC 20546	14. Sponsoring Agency Code

15. Supplementary Notes

16. Abstract

Investigations of the low-speed longitudinal characteristics of two powered close-coupled wing-canard fighter configurations have been completed in the Langley V/STOL tunnel. Data were obtained at angles of attack from -2° to 42°, Mach numbers from 0.12 to 0.20, nozzle and flap deflections from 0° to 40°, and thrust coefficients from 0 to 2.0 to represent both high-angle-of-attack subsonic maneuvering characteristics and conventional takeoff and landing characteristics. Limited data were obtained at angles of attack of 0° and 10° with the nozzles deflected either 60° or 90° and the flaps deflected 60° to represent vertical or short takeoff and landing characteristics.

17. Key Words (Suggested by Author(s))	18. Distribution Statement
Vectored thrust effects Wing-canard Fighter configuration	Unclassified - Unlimited Subject Category 02

19. Security Classif. (of this report)	20. Security Classif. (of this page)	21. No. of Pages	22. Price*
Unclassified	Unclassified	89	$6.00

* For sale by the National Technical Information Service, Springfield, Virginia 22161

NASA-Langley, 1979